12-2020

Leveraging Biomimicry and Additive Manufacturing to Improve Load Transfer in Brittle Materials

Ana Paula Bernardo
University of Arkansas, Fayetteville

Leveraging Biomimicry and Additive Manufacturing to Improve Load Transfer in Brittle Materials

A thesis submitted in partial fulfillment
of the requirements for the degree of
Master of Science in Civil Engineering

by

Ana Paula Bernardo
Federal University of Espírito Santo
Bachelor of Science in Civil Engineering, 2018

December 2020
University of Arkansas

This thesis is approved for recommendation to the Graduate Council.

Michelle Lee Barry, Ph.D.
Thesis Director

Richard A. Coffman, Ph.D.
Committee Member

Gary Prinz, Ph.D.
Committee Member

ABSTRACT

With the emergence of Additive Manufacturing (i.e., 3D printing) in construction, new strategically designed shapes can be created to improve load transfer through structural members and foundations. Cross-sections can be optimized to carry load using less material, or even using weaker constituent materials, like soils, which are cheap and abundant. The goal of this research is to investigate the benefits of using cellular patterns which leverage biomimicry in civil engineering applications, since nature has perfectly engineered materials and patterns which carry loads with the least amount of material possible. Most of the periodic cellular work to date has focused on metallic materials, which exhibit ductile performance. Therefore, this study is specifically related to brittle materials as there is a need to understand the load transfer mechanisms in this type of material. An initial investigation of biomimicry was carried out, and organisms that presented improved mechanical behavior due to geometry were identified. Analogue prototypes inspired by these biological findings were designed and specimens were 3D printed using a binder-jetting device which offers a resulting part with a brittle behavior, mimicking a cemented soil. Solid samples using the same gross area were also printed to compare performance with the cellular shapes. Uniaxial compression tests were performed in the specimens and in cylinders used to track the properties of the material. The variability of the 3D printer utilized in this study and the material's susceptibility to experimental differences were found to be important factors and some printer settings made it difficult to compare the cellular and solid specimens directly. Overall, the results show that the cellular structures exhibited a significant improvement in the load-to-weight ratio compared to the solid configuration. Applying this improvement in material efficiency to building products can lead to more sustainable and cost-effective construction practices.

ACKNOLEDGMENTS

I would like to manifest my deepest and sincere gratitude to my advisor, Dr. Michelle Lee Barry, for the opportunity of participating in this fascinating project, and for all the encouragement, guidance and support throughout my master's degree program. Her expertise, passion and optimism inspired me, and her care and understanding made my experience not only possible but also comfortable and pleasant. Furthermore, I would like to thank the members of my master's thesis committee, Dr. Richard A. Coffman and Dr. Gary Prinz, for accepting being part in this important moment of my education and for generously offering their time and educational guidance. I would also like to thank many other people for their help during the development of my research. Thanks to the master scientific technician of the Civil Engineering Department at UARK, Mr. Mark Kuss, for the assistance with machines and equipment at the laboratory. Thanks to Dr. Anibal Santos, a fellow graduate student, for his valuable pieces of advice and support with computational codding. Thanks to the undergraduate research assistants, Christina Childress, Anne Claire Hunter and Olivia Overton, for their help with experiments in the laboratory. I am heartly grateful to my parents, family and friends for providing me with unfailing support and continuous encouragement throughout these two years of my program. This accomplishment would have not been possible without them. Finally, I would like to express my profound gratitude to God, Who has loved me so much.

TABLE OF CONTENTS

LIST OF TABLES

LIST OF FIGURES

1 INTRODUCTION

Structural members and foundations are typically made with simple cross-sections (i.e., squares, rectangles, circles) due to limitations of construction equipment and technologies and the efficiencies associated with these shapes in design and construction. However, with the emergence of additive manufacturing (AM) (i.e., 3D printing) and robotics in construction, new strategically designed shapes can be created to improve load transfer through these members. Cross-sections can be optimized to carry load using less material, or even using weaker constituent materials, such as soils, which are cheap, abundant, and environmental-friendly, as a building material. This improvement in building products (e.g., bearing walls, columns, beams, foundations, and soil enhancement) can lead to more sustainable and cost-effective construction practices. In the case of soils, it may also provide a way to improve roadways and foundations, and even build structures in remote areas (e.g., sub-Saharan Africa, Antarctica, war-torn or disaster areas, the Moon and Mars), that would not be possible with traditional techniques.

Biomimicry is the design and production of materials, structures, or systems that are modeled imitating patterns and strategies from nature (The Biomimicry Institute, 2020). Nature has highly efficient and sustainable organisms, and the idea of consciously emulating life's genius was popularized by Benyus (1997). Leveraging biomimicry has proven to be a wise approach in the design of efficient systems, processes, and new innovative products.

Many biological organisms have a complexly organized constitution and structure that gives them mechanical properties well above that of their constituent materials. An understanding of the structuring, mechanisms and functions of these organisms could lead to improved periodic cellular structures for applications in civil engineering infrastructure. Most of the periodic cellular work to date has focused on metallic materials, which have a ductile performance and high tensile

strength, a significantly different behavior from many brittle materials used in construction. Therefore, this research is specifically focused on load transfer and performance of brittle materials (e.g., cemented soil, ceramic, and concrete), as there is a need to better understand the mechanisms of cellular patterns in this type of material.

1.1 Objective

The objective of this research is to leverage biomimicry to identify cellular patterns that can improve the load transfer ability and material efficiency in brittle materials, with the future purpose of supporting the application of soil-based materials in additive manufacturing forms of construction. The specific goals are:

a) Investigate and learn from biological examples that exhibit strength from geometry rather than the material itself.
b) Mimic these mechanisms with analogue prototype using AM processes (i.e. 3D printer) and brittle materials.
c) Gain further understanding of the bio-inspired mechanisms through experimental testing.

1.2 Overview of Thesis

Following this introduction given in Chapter 1, Chapter 2 presents a literature review on biomimicry, biological organisms with enhance mechanical properties, additive manufacturing in construction, mechanics of brittle materials, and cellular solids. Chapter 3 is then related to the methodology applied to conduct this research project, including the design of prototypes inspired by the biological investigation, the materials and equipment used, the experimental tests and analyses implemented. After that, Chapter 4 presents the results and discussion related to the 16 3D printed batches, divided into three segments, which contain the properties, stress-strain curves

and fracture modes for the fabricated prototypes and cylinders. Finally, Chapter 5 provides the conclusions of this research, including perceptions on the functioning of the 3D printer utilized, important aspects for the design of cellular solids with brittle materials, and the impressive improvement in material efficiency that the utilization of periodic cellular cross-sections could deliver.

2 LITERATURE REVIEW

2.1 Biomimicry

For 3.8 billion years, nature has been improving its structures and mechanisms to achieve the best performance under very limited resources (Bhushan, 2009). This evolution is based on the optimization of systems and has led to highly efficient and sustainable organisms (Ivanić et al., 2015). Many organisms have mechanical properties that greatly exceed the properties of the basic materials that they are comprised of. These types of biological organisms are often comprised of composites that are complexly organized in terms of constitution and structure and have a hierarchical organization at multiple length scales (Meyers et al., 2008). Along these lines, observing nature and learning from it can be considered a wise approach for the design of new materials and technologies. Biomimicry is the science that studies systems of nature and the imitation of them. According to Ivanić et al. (2015), it is the transmission of organisms' solutions into the sphere of design and engineering. Since the release of her first book in 1997, Janine Benyus has advanced the practice of biomimicry around the world. She has co-founded the world's first bio-inspired consultancy, Biomimicry 3.8, which has brought nature inspired sustainable designs to more than 250 clients including Boeing, Colgate-Palmolive and Nike. Benyus also co-founded the Biomimicry Institute, which provides the world's most comprehensive biomimicry inspiration database, AskNature.

One of the most successfully commercialized bio-inspired products is VELCRO, which was formally patented in 1955 by George de Mestral. VELCRO mimics microscopic hooks present on seed-bearing burrs, which give them the ability to attach to wool (Meyers and Chen, 2014). More recently, Pax Water developed a bio-inspired product called the lily impeller (UGSI Solutions, 2020), which is an energy efficient design imitating the Nautilus shell shape (Figure

2.1). In terms of processes or systems, Blue Planet recently produced a technology (Blue Planet, 2015) which mimics coral reefs from the oceans, taking carbon dioxide from the atmosphere, and converting it into limestone.

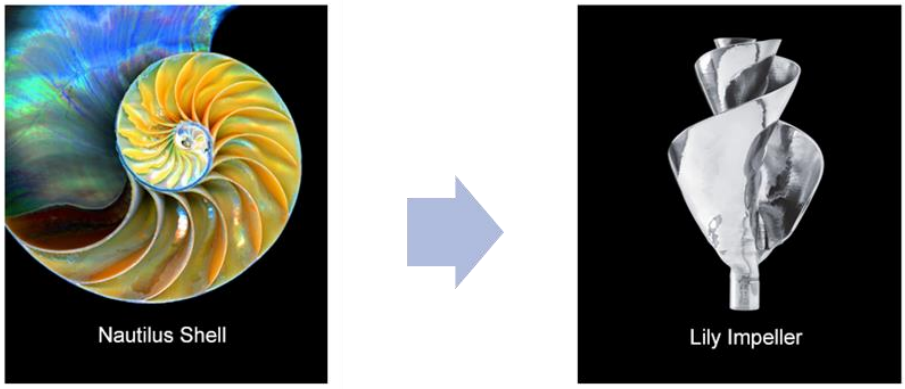

Figure 2.1 Energy efficient design of Lily Impeller, bio-inspired by the Nautilus shell shape. (UGSI Solutions, 2020)

Numerous examples of innovative designs leveraging biomimicry have also been explored in civil engineering applications. The Blue Planet technology previously mentioned creates limestone which can be used as aggregate for concrete in construction. Another innovation team, Natural Process Design, Inc., has created a self-repairing concrete by applying the idea of materials in nature that can self-repair-skin, such as insect exoskeletons, abalone shells, bones and starfish arms, in which repairs initiate from inside the organisms, (Nature Process Design, 2005). Engineers have also explored new forms of structural elements or geometries using inspiration from nature. TECTONICA Architecture, a Puerto Rican innovation team, designed a frame technology for reinforced concrete buildings, called STICK.S, which reduces seismic vulnerability by emulating the human femur's structuring (Figure 2.2) (AskNature, 2016).

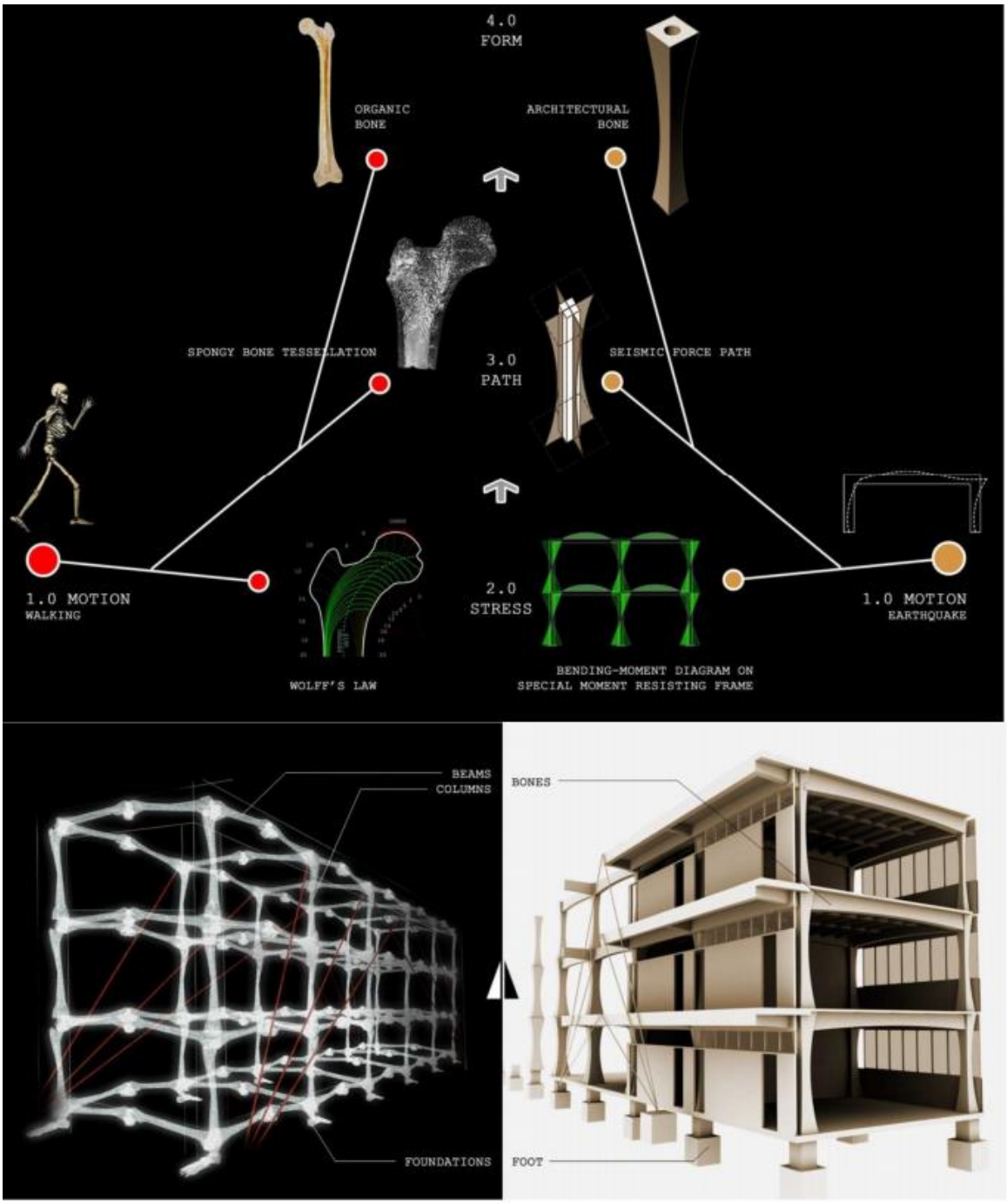

Figure 2.2 STICK.S building frames inspired by the human femur. Illustrated by Wilfredo Mendez. (Kennedy, 2017)

Inspired by architectures found in nature, engineers can also optimize designs to improve or tune the mechanical properties of materials (Gu et al., 2016). This study specifically focuses on

improved load carrying ability of some materials and organisms in nature for applications in geotechnical and structural engineering. In these areas, it is meaningful to recognize the improved mechanical properties of structures in natural organisms and try to mimic them in the design of foundations, earth retaining structures, soil improvement, roadways, bearing walls and columns. Relevant mechanical properties in these aspects are increased compressive strength, tensile strength, toughness, stiffness, strength-to-weight ratio, and friction.

2.1.1 Biological Organisms with Enhanced Mechanical Properties

A number of hierarchical structures or geometric patterns present in nature that exhibit these improved mechanical behaviors was investigated and a summary of them is given here.

2.1.1.1 Mollusc Shells

Molluscs have soft bodies, therefore they need a hard shell to provide protection against impacts and compressions from the ocean and against predators (Meyers & Chen, 2014). These shells are composed of a ceramic phase, for example, calcium-carbonate biomaterial, and a small portion of proteins. The ceramic material itself does not have an efficient structural capability because of its brittleness, but when it is combined with the proteins in a specific structural arrangement, a bio composite is established with exceptional mechanical properties (Mayer & Sarikaya, 2002).

The abalone shell (*Haliotis*) is constituted of two calcium-carbonate (CaCO3) microstructures: a calcite exterior layer and an aragonite internal layer (Nakahara, Kakei & Bevelander, 1982). The aragonite layer is also named nacre and it has a “brick-and-mortar” structure of tiled aragonite platelets glued together by organic layers (Figure 2.3) (Sarikaya, 1994). Figure 2.4 shows the stratified structure of the nacre in a transmission electron microscope (TEM)

micrograph (Menig, Meyers, Meyers, & Vecchio, 2000). 95% of the composite weight is ceramic and 5% is organic. The thickness of the tiles is approximately 0.5μm whereas the protein layer is approximately 20-30 nm thick (Lin & Meyers, 2005).

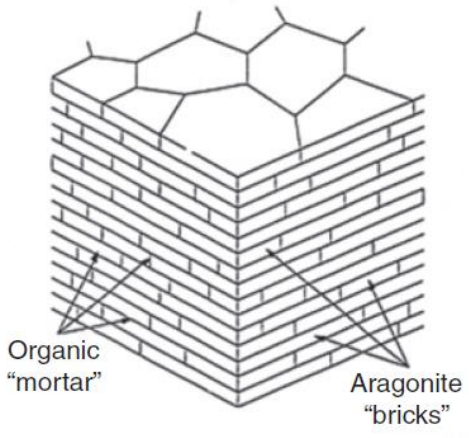

Figure 2.3 Schematic drawing of "brick-and-mortar" structure of nacre in abalone shell. (Sarikaya, 1994)

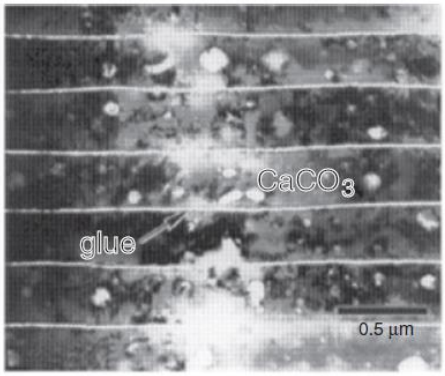

Figure 2.4 TEM micrograph exhibiting the aragonite layers and organic interlayers. (Menig et al., 2000)

Menig et al. (2000) tested the compressive and tensile strength of red abalone shells and measured it using Weibull statistics (Weibull, 1951) with failure probabilities of 50%. The results are presented in Figure 2.5.

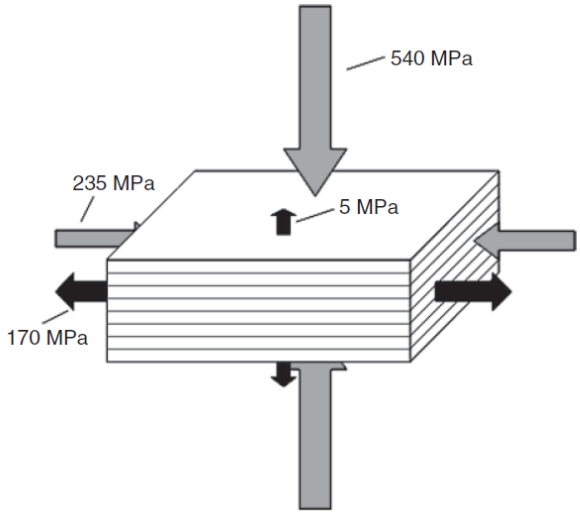

Figure 2.5 Strength of Nacre according to loading directions (Meyers & Chen, 2014)

The abalone shell demonstrates a high compressive strength perpendicular to the tiles and a low tensile strength in the same direction. In the parallel direction both strengths have considerable magnitude that is related to the high toughness of the material.

2.1.1.2 Hoof

When a horse is running, it subjects its hoof to repeated high loads and abrasive forces with the substrate. The hoof has the function of transferring these forces from the ground to the bony skeletal elements (Kasapi & Gosline, 1997). According to Bertram and Gosline (1986), the horse hoof is one of the toughest biomaterials known, and its complex design produces a material with integrated fracture toughness properties.

The hoof wall is a lightweight truncated-cone-shaped structure made of keratin (Kasapi & Gosline, 1997). The keratin is a protein-based fibre-reinforced nanoscale composite that comprises intermediate filaments (IFs) and a matrix phase (globular proteins). Beyond the nanoscale, the hoof wall is organized into tubules and the intertubular material, forming a macroscale composite (Kasapi & Gosline, 1999). Approximately half of the structure consists of the tubules, that are

found on the length of the wall and are parallel to the surface of the hoof (Bertram & Gosline, 1986). Figure 2.6 and Figure 2.7 show schematics of the hoof wall and IFs. The IFs (α-helical protein bundles with 8nm in diameter) are embedded in a keratin matrix. In the inner wall the IFs are placed horizontally in the intertubular material along tubule axis, but the mid wall presents IFs in angles from 0° to 30°. The tubules have elliptical format with approximately 220x140 μm in the major and minor axes and a middle cavity of approximately 50 μm. A circular lamellae 5-15 μm thick of keratin surround the tubules. In their studies, Kasapi and Gosline (1999) concluded that the tubules have the mechanical function of control the crack propagation and enhance fracture toughness, and that hooves are capable of supporting large compressive and impact loads and provide some shock absorption from the impact.

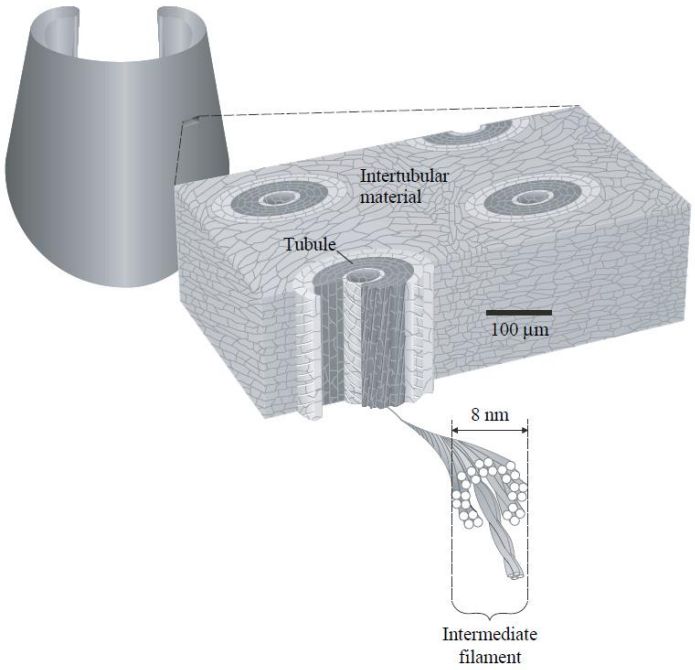

Figure 2.6 Illustration of the front view of an equine hoof wall and a sketch of a hoof wall showing tubules and intertubular material. (Kasapi & Gosline, 1999)

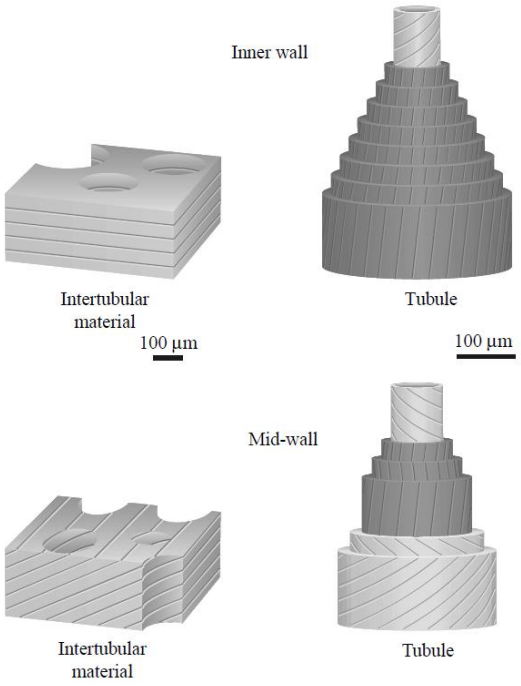

Figure 2.7 Illustrations of the plane of intermediate filaments (IFs) from intertubular material (Kasapi & Gosline, 1999)

2.1.1.3 Honeycomb

Many biological structures require high strength, stiffness, or toughness, while being light weight at the same time. Nature has solved this problem by formatting organisms with a thin solid shell and filling the core with lightweight foam or adding internal reinforcing struts. One example of this is the Honeycomb. Honeycombs are built by bees using the natural wax that they produce, and they have the function of food storage (honey and pollen) and developing bee larvae housing. Therefore, it is necessary for honeycombs to be strong, lightweight and efficiently designed. The soft wax material is rather weak, but when arranged in a repeating hexagonal pattern, it exhibits efficient load support using very minimal amounts of material (Figure 2.8). Hexagons can fit together without any gaps to tile the plane (three hexagons meeting at every vertex), and so are useful for constructing cellular periodic materials (Pronk et al., 2008). Honeycomb structures, inspired from bee honeycombs, have found widespread applications in various fields, including

architecture, transportation, mechanical engineering, chemical engineering, nanofabrication and, recently, biomedicine (Zhang et al. 2015). For instance, this type of geometric pattern has enabled the design of lightweight sandwich panels used in aircraft, ships, automobiles, heat sinks, packing materials, and vibration and shock absorbing materials (Schaedler et al., 2011; Gumruck and Mines, 2013, Jeong et al., 2013), as well as the design of periodic cellular metals (PCMs) which have been studied for their high strength-to-weight ratios and thermal flow properties (Lu, 1999; Deshpande and Heck, 2001; Wadley, 2006; Wahl et al., 2012; Choi and Lee, 2014). More discussion of these studies on periodic cellular materials is given in section 2.5 - Two Dimensional Cellular Solids.

Figure 2.8 Honeybees on Honeycomb. (Woolley-Barker, 2014)

2.1.1.4 Toucan Beak

Bird beaks need to be strong for probing food, fighting, and killing prey, but at the same time they need to be lightweight to allow them to fly. The beaks are usually short and thick or long and thin; however, the toucan has a long and thick beak. This is achieved by a well-designed structure of a keratin-based hard shell and an internal cellular core, enabling a low density and a

high stiffness (Figure 2.9). The keratin shell is comprised of layers of hexagonal tiles that have 30-60 μm in diameter and are 2-10 μm thick. The tiles are connected together by an organic glue and the total thickness of the shell is approximately 0.5mm (Seki et al., 2005). Figure 2.10 shows a scanning electron micrograph (SEM) of the exterior of the Toucan beak. Inside the beak there is a foam closed-cell structure built with bony struts. Figure 2.11 shows SEM images of the internal foam of the beak, and Figure 2.12 shows a scheme for the entire beak.

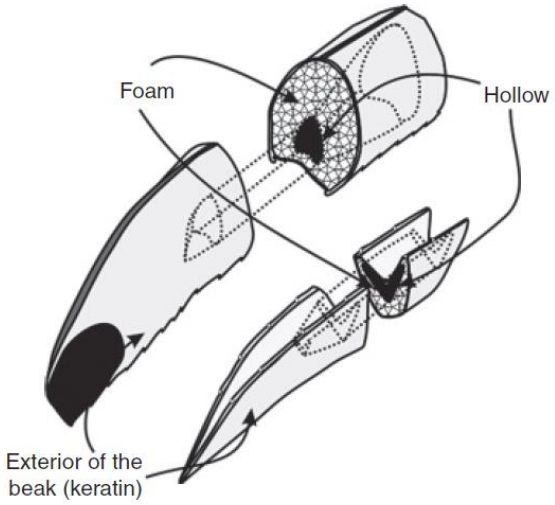

Figure 2.9 Schematic representation of Toucan Beak. (Seki et al., 2005)

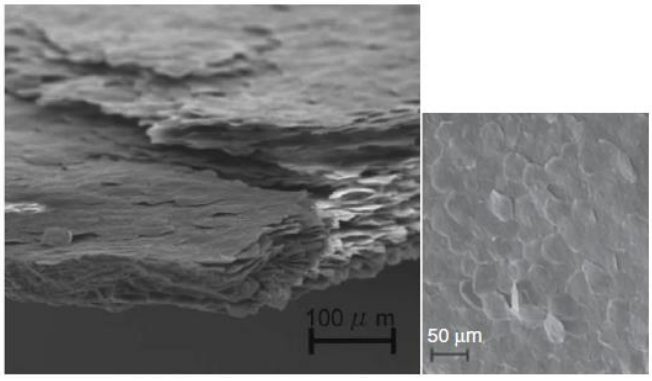

Figure 2.10 SEM images of the keratin tiles on the surface of the Toucan beak. (Seki et al., 2005)

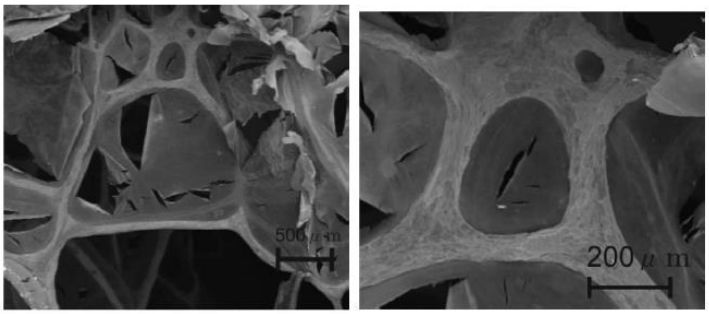

Figure 2.11 SEM images of the interior foam of the Toucan beak. (Seki et al., 2005)

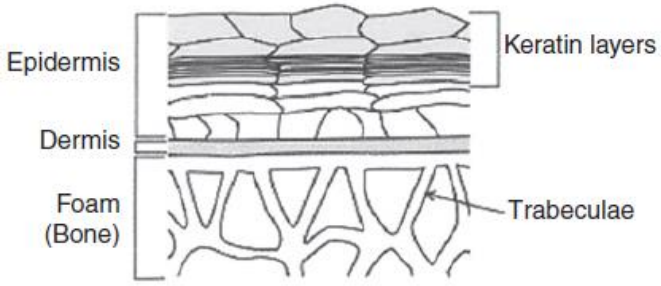

Figure 2.12 Scheme of cross-section of the Toucan beak. (Meyers & Chen, 2014)

Seki et al. (2005) in their studies showed that the Toucan beak has a significantly higher bending strength than a material that comprises the shell and the hollow zone. They found that the internal foam enhances the buckling resistance, and that there is a synergism between the two parts that contribute to the stability of the beak.

2.1.1.5 Horn

Horns found in animals such as cattle, sheep and goats are tough, resilient and impact resistant. They must be strong and durable because of the exposition to high loading impacts. Horns are non-living tissue that projects from the back of the skull and are formed of a cancellous bone core covered with a skin. They do not have a mineralized component, rather, they are mainly composed of alpha keratin. Alpha-keratin is a structural, fibrous protein found in wool, hair, nails, equine and bovine hooves, and horns. It is composed of microfibrils (IFs) that are embedded in a viscoelastic protein matrix. In horns, the filaments and matrix are organized into circular lamellae

that surround a hollow tubule (medullary cavity), which is also similar to the configuration of hooves and osteons in compact bone (Tombolato et al., 2010).

Tombolato et al. (2010) studied the Bighorn sheep horn and reported that it is a composite material consisting of stacked lamellae in the radial direction with a thickness of 2–5 μm, with tubules, 40 x 100 μm in diameter, interspersed between the lamellae, resulting in an overall cross-sectional porosity of 7%. Across the thickness of the horn wall, the porosity decreases from the external surface (8–12%) to the interior surface (0%). Figure 2.13 shows the optical micrographs of transverse and longitudinal sections of the horn and Figure 2.14 presents a schematic of its hierarchical structure.

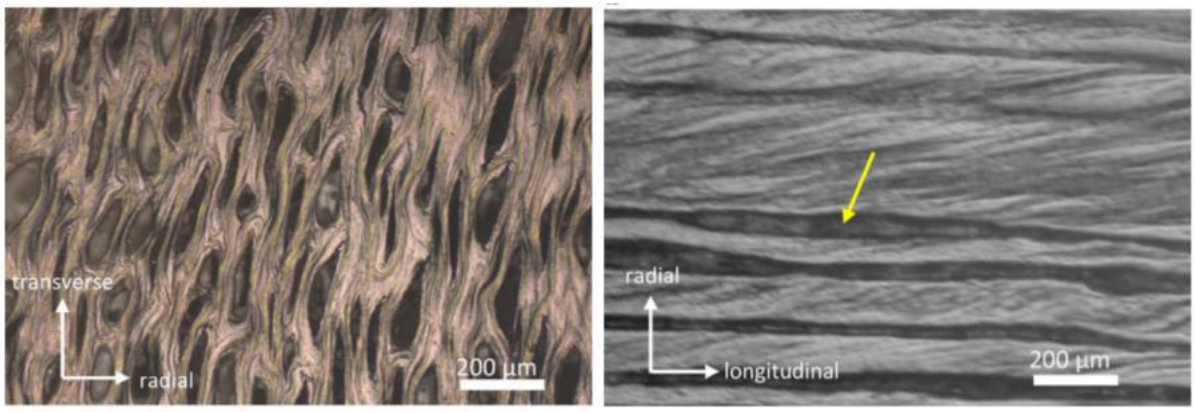

Figure 2.13 Optical micrographs of transverse and longitudinal sections of the Bighorn sheep horn. (Tombolato et al., 2010)

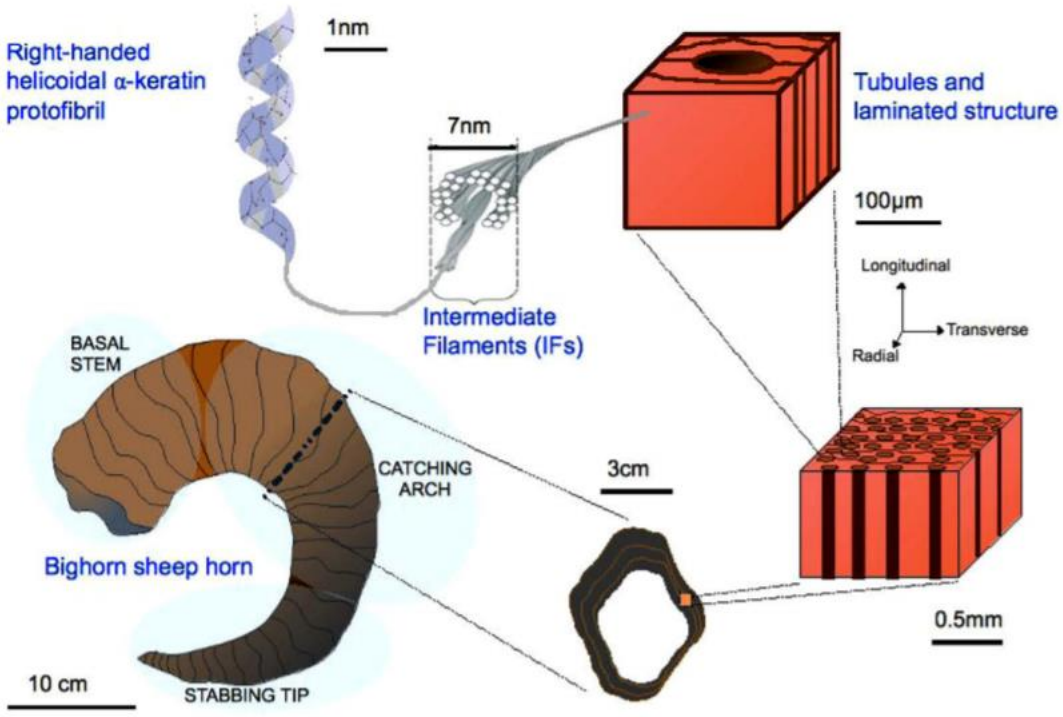

Figure 2.14 Hierarchical structure of Bighorn sheep horn. (Tombolato et al., 2010)

2.1.1.6 Plant-Bird of Paradise Stalk

Another example of strong, lightweight and efficiently designed organisms is plant stalk. They are composed of cellulose and lignin in cells aligned parallel to the growth axis. Figure 2.15 shows the plant stalk from the Giant-Bird of Paradise (*Strelitzia*). The cells have a rectangular shape on the longitudinal section and elliptical shape on the cross-section, forming cylindrical holes. The struts are also composed of a pattern of holes, that helps to decrease the weight of the structure. This design enhances the flexural resistance of the stem (Meyers et al., 2013).

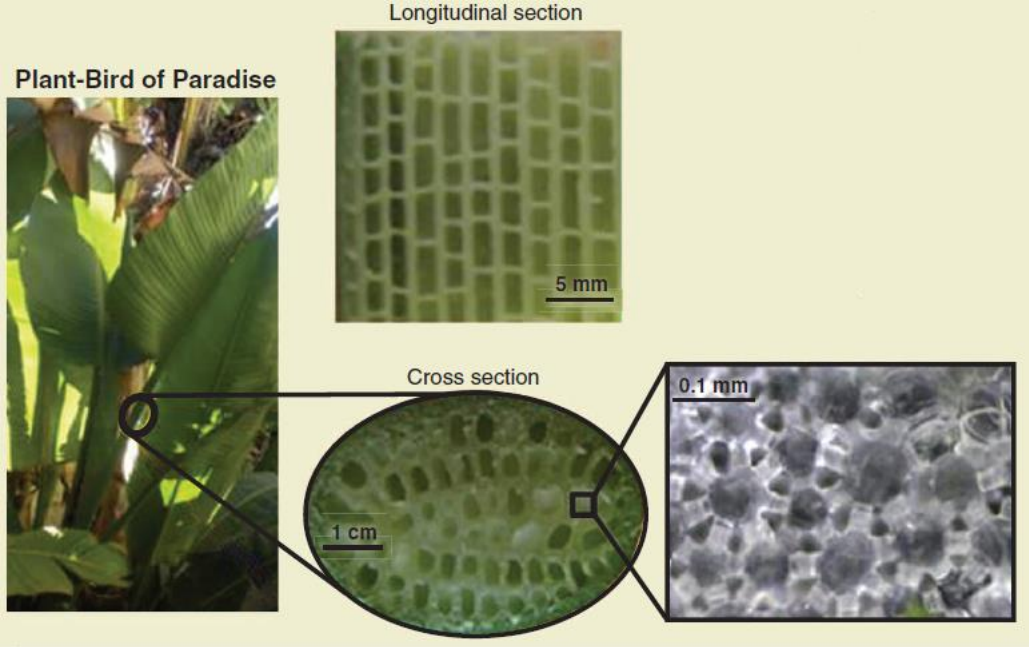

Figure 2.15 Schematic representation of Plant stalk for the Bird of Paradise. (Meyers et al., 2013)

2.1.1.7 Cortical Bone

Bone is the structural component of our body and is composed of a ceramic (calcium phosphate, or hydroxyapatite) and polymer (collagen). It has multiple functions, such as supporting the human body, protecting organs, storing mineral ions, and producing blood cells, but the most important is its ability to resist fracture. Bones are classified into two types: cortical (or compact) bone and cancellous bone (Figure 2.16). This study focuses on the cortical bone which is found in long weight-carrying bones such as the Femur, Tibia and Fibula. This type of bone has a density of approximately 2 g/cm^3 and a porosity typically between 5-10%. It is generally characterized by microscopic structures called osteons, which are comprised of concentric lamellae surrounding a vascular channel. Figure 2.17 presents a typical osteon with two types of vascular channels: Harvesian canals and Volkmann's canals (Meyers & Chen, 2014).

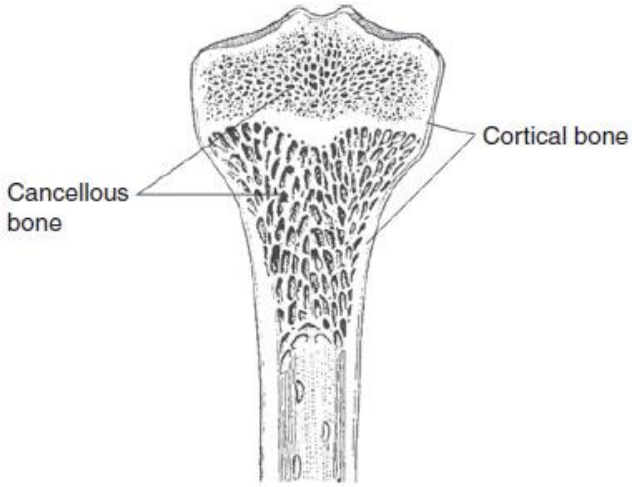

Figure 2.16 Classification of Bones: Cortical and Cancellous. (Mann, 2001)

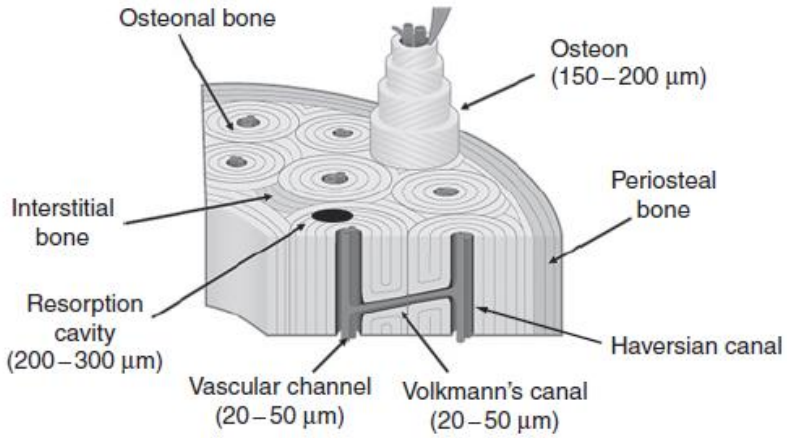

Figure 2.17 Schematic representation of microstructural feature of cortical bone, osteon. (Novitskaya et al., 2011)

Bones are assembled into a complex hierarchical structural. Meyer and Chen (2014) divided its structure into seven levels. Level I to Level III are related to molecular and fibril arrangements. Level IV to VII are represented in Figure 2.18. Level IV has 5-7 µm thick lamellae formed by the fibril arrays. Level V presents the basic unit of the cortical bone, the osteon, assembled by the lamellae in concentric cylinders. In Level VI, there is the light-microscope level

presenting osteons with a central vascular channel for the cortical bone. Level VII is full and integrated bone.

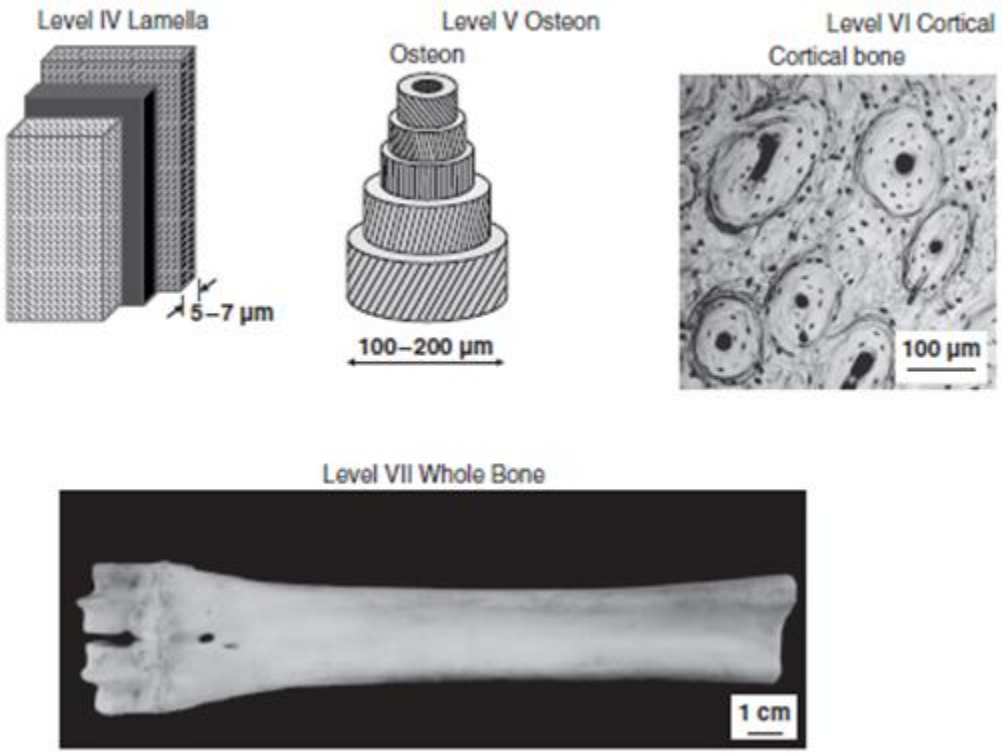

Figure 2.18 Hierarchical Structure of Bones (Adapted from Meyers & Chen, 2014)

2.2 Additive Manufacturing (AM)

Additive Manufacturing (AM), often called 3D printing, is a collection of technologies where a three-dimensional Computer-Aided Design (CAD) model is used to build a 3D object without a process plan (Gibson et al., 2015; Ngo et al., 2018; Elliott & Waters, 2019). AM uses a layer-based approach, where parts are fabricated by adding material in layers; an individual layer represents a thin cross-section of the part extracted from the initial CAD data (Gibson et al., 2015; Bikas et al., 2016; Ngo et al., 2018). The benefits of using AM include the conveying of parts with complex geometries, and the applicability to a variety of materials, such as plastic, metal, ceramic, concrete and soils, which enable designers and engineers to produce unique products (Bikas et al.,

2016; Ngo et al., 2018). AM also offers reduced time for building processes and seamless products, which require just one process step. Another benefit is the reduced resources required, including labor and materials. Although the cost of the initial equipment and material can be rather expensive, the quantity of labor needed is compressed because of the use of computers and robots and the quantity of materials decreases because of a near-zero material waste, since AM can be much clearer, more streamlined, and more versatile than traditional methods (Gibson et al., 2015; Bikas et al., 2016). The advantages of AM technologies have led scientists to deepen studies on its development and application in many fields (e.g., medical, aerospace, automotive and construction).

2.2.1 Binder Jetting (BJ) Process

The AM technique used in this study was a power-based binder jetting (PBBJ) process. In this process, the fabrication of objects is achieved by selectively depositing a liquid binder with an inkjet print head into a powder bed (Gibson et al., 2015; Elliott & Waters, 2019). Once a layer is printed with binder, the powder bed is lowered, and a new layer of powder is spread on top of it. This process is repeated until the full height of the part is complete (Gibson et al., 2015; Chen & Zhao, 2016). The binder is responsible for bonding powder particles together and most of the object is composed of powder, with only a small portion of binder present. Figure 2.19 shows a schematic view of the PBBJ printing process. At the end of the process, there is a build box filled with powder and parts spread in the middle of it. Once the build is cured, the parts can be removed from the powder chamber.

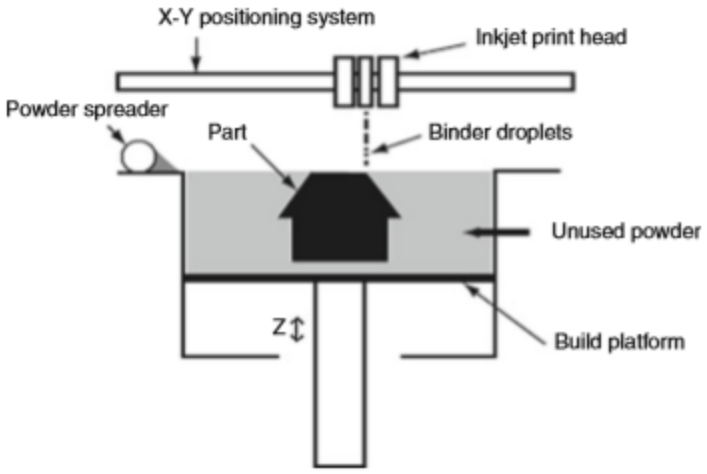

Figure 2.19 Binder jetting process schematic. (Gibson et al., 2015)

2.2.2 AM in Construction

Aerospace, automotive, and healthcare industries have explored the use of AM, focusing on rapid prototyping to fabricate complex geometries with no part-specific tooling, much less waste material, and reduced production time. The construction industry is now also starting to investigate AM technologies as a way to overcome challenges such as work in severe environments (e.g., freezing or high temperatures, or exposition to chemical and nuclear contamination), safety, large production of waste material, use of non-sustainable materials, and the transportation of materials. AM would also allow designers to produce one-of-a-kind complex geometries, that would be difficult and costly to produce using traditional processes. Conventional construction uses simple and rectilinear designs to facilitate ease and schedule constraints; however, large-scale AM is allowing architects and engineers to rethink their design and forms, giving them more freedom to consider functionality rather than constructability (Camacho et al., 2018). The potential of new unique designs needs to be investigated to maximize the AM potential in construction and research is needed to ensure these new geometries and materials are able to

achieve the expected levels of reliability and safety. While much more study is needed to fully realize AM as a cost-effective and reliable option in the construction industry, the potential benefits it can provide are worthy of further work and development (Camacho et al., 2018).

Some of the AM processes investigated in civil construction so far include material extrusion and binder jetting. Material extrusion comprises the process of extruding material through a nozzle layer-by-layer and has been the most explored in the construction sector for large-scale components with cementitious material. A material extrusion process called Contour Crafting (CC) was one of the first AM techniques proposed for the construction industry (Khoshnevis and Dutton, 1998; Khoshnevis, 1999; Khoshnevis, 2004). This process has been used to extrude paste-like materials (e.g., concrete, or ceramic paste) through a 3D printing-head mounted on a gantry system. Similar techniques for commercial and academic applications have been developed by several different companies or research groups around the world such as Apis Cor, which built the biggest 3D printed building in Dubai in 2019 (Figure 2.20).

Figure 2.20 The biggest 3D printed building in Dubai (Apis Cor, 2019)

Most of the cementitious materials for this application use Portland cement, which is well known for its satisfactory mechanical properties and low cost, but its production is not sustainable because of large amounts of carbon dioxide (CO_2) released to the atmosphere (Camacho et al.,

2018). A more sustainable application of AM in construction would be with the utilization of soil (e.g., sand and clay) as building material. The powder-bed binder jetting (BJ) process represents an interesting approach for this application, because the soil could act as the powder material used in this technology. In recent years, researchers have explored the application of the PBBJ process in the civil engineering industry. The first study on the use of PBBJ technology in construction was made by Pegna (1997) and consisted of the deposition of a layer of Portland cement over a layer of sand. A similar sand PBBJ technology, D-shape from Italy, applies the PBBJ process with sand and a binder to create stone-like structures (D-Shape, 2020). Emerging Objects from the USA recently developed a rapid concrete masonry unit that uses inkjet sprays to bind small-sized aggregates with a fiber-reinforced cement mixture (Emerging Objects, 2020). Shakor et al. (2017) fabricated specimens made of selectively dropping water onto calcium aluminate cement and Portland cement. Architectural 3D printed elements are being produced with inorganic polymer material and inkjet technology by CONCR3DE from The Netherlands (CONCR3DE, 2020). Similarly, Xia and Sanjayan (2016) used PBBJ technology to print geopolymer specimens for construction applications.

2.2.3 AM using Soil Based Materials

Some AM technologies that use soil already exist, such as D-Shape that uses sand and binders of magnesium oxide and magnesium chloride (Oberti & Pantamura, 2015), as mentioned before. Perrot et al. (2018) successfully 3D printed, with a 6-axis robot, an earth-based material (fine clay soil mixture of kaolinite, illite and smectite) with improved green strength due to the addition of alginate, which benefit the feasibility of soil-based materials in 3D printing for the construction field. Moreover, the World's Advanced Saving Project (WASP) has been developing large size delta printers to extrude construction materials, which use natural mixtures that contain

soil and straw. Gaia, constructed in Italy in 2018, was the first 3D printed house using natural materials from the surrounding area and a new Crane WASP technology (Figure 2.21).

Figure 2.21 The first 3D printed house with earth in Italy (WASP, 2018)

In 2010, the first one-shot-printed house ever was 3D printed using PBBJ process by D-Shape in Italy. UnaCasaTuttaDiUnPezzo has a very simple design, with four walls and a roof, with dimensions of 2.4 m x 4 m, and was printed in 3 weeks (Figure 2.22). The D-shape system operates by pouring binder on a sand layer, using an aluminum gantry structure to hold the printer head. The deposition of binder works as a "structural ink' on the sand, causing a solidification process just in selective areas and the surplus sand acts as support until the solidification is complete. This system uses two inorganic reactants for the binding chemistry: metallic oxide in powder form (Magnesium Oxide, Silicon Oxide, Iron Oxide, Calcium Oxide and Aluminium Oxide) or Magnesium Chloride ($MgCl_2$) and its various hydrates $MgCl_2(H_2O)_x$, which can be extracted from brine or sea water. The benefits of this system include the light weight of the aluminum structure, which facilitates the transport and assembly, the possibility to use local sand, as a zero-mile base material, the inorganic binder is ecofriendly with relation to air emissions, and the minimal human intervention which reduces the risk of accidents and promotes safety (Cesaretti et al, 2014).

Figure 2.22 UnaCasaTuttaDiUnPezzo in Italy (D-Shape, 2010)

Reduction of material transportation costs and more sustainable design solutions can be achieved with the use of locally available resources. The use of on-site materials also allows construction in locations that are difficult to access. Furthermore, since sending raw construction materials into space is very difficult and expensive, CC and D-Shape technologies have been investigating the possibility of building structures using in-situ resources such as regolith rock on the Moon (Mueller et al., 2016; Cesaretti et al., 2014). Additionally, the combination of AM processes and local materials could allow constructions in disaster affected regions that may have limited workforce and construction material resources. Labonnote et al. (2016) suggest the use of AM for construction of first response shelters that can be rapidly produced.

2.3 Biomimicry with Additive Manufacturing

Nature's complex architectures exceed the capability of traditional manufacturing and construction methods. The advent of additive manufacturing has now made it possible to emulate the intrinsically multiscale, multimaterial and multifunctional biological structures (Huang et al., 2013; Gao et al., 2015; Yang et al., 2018). Studies have shown that the superior performance of biomaterials strongly depends on their hierarchical structures (Bechtle et al., 2010; Meyers & Chen, 2014). The fabrication of these hierarchical features found in nature has shown to be possible

with the combination of AM techniques and advanced chemical and biological synthesis methods to produce novel synthetic materials that mimic natural constituents (Gu et al., 2016). Bioinspired structures fabricated with recent 3D-printing technology developments can be classified into three categories: single material, multimaterials, and composites (Yang et al., 2018).

Polymer, metal, graphene, etc. have been used as a single material for 3D-printed bioinspired structures. The geometries and forms of these structures have shown that they perform an important role in the enhancement of their properties, rather than the constituent material itself. Using a photo resin and an optical two-beam super-resolution lithography, Gan et al. (2016) demonstrated the replication of gyroid photonic nanostructures found in the butterfly Callophrys rubi (Figure 2.23). Gyroid structures are chiral periodic structures with unique geometrical properties. They are object of interest in photonics for the application in photonic crystals and optical metamaterials with topological complexity.

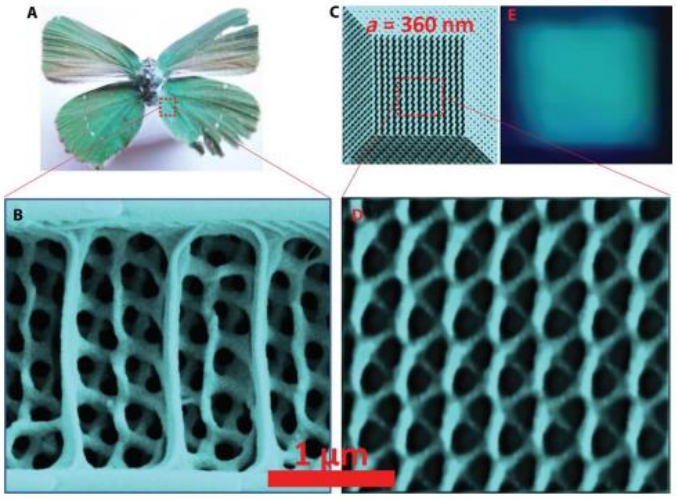

Figure 2.23 Image of the butterfly C. rubi., the nanostructures found within the butterfly wings, and the artificial gyroid nanostructure fabricated. (Gan et al., 2016)

Tiwary et al. (2016) studied the evolution of two complex shapes in seashells. They presented a mechanics-based model and fabricated similar shapes using PLA-based polymer and FDM 3D printer (Figure 2.24). The complex shapes were shown to play a pivotal role in stress transfer to enhance the safety from extreme conditions of the living species residing inside. The results show that the structuring can sustain loads that are nearly twice as high as those based on their respective counterpart simple shapes. Their study introduces pathways for the design of new architecture for structural applications.

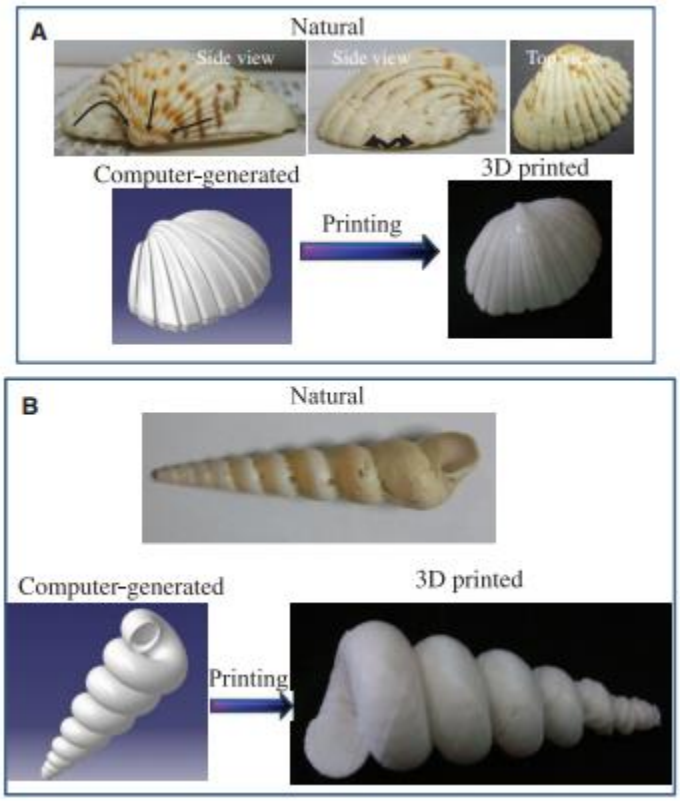

Figure 2.24 Images of the natural, computer-generated and 3D printed shells. (Tiwary et al., 2016)

Quin et al. (2017) combined bottom-up computational modeling with experiments based on 3D-printed models with photopolymer material to investigate the mechanics of porous 3D graphene materials (Figure 2.25). Their study reveals that the 3D graphene assembly has an

exceptionally high strength at relatively low density, since it has a density of just 4.6% of that of mild steel and it is 10 times stronger than mild steel. The porous graphene has an ultralight nature, outstanding mechanical properties, high surface area, stable chemical and thermal properties, which makes it a promising possibility for many engineering applications, enabling the fabrication of lighter and stronger products.

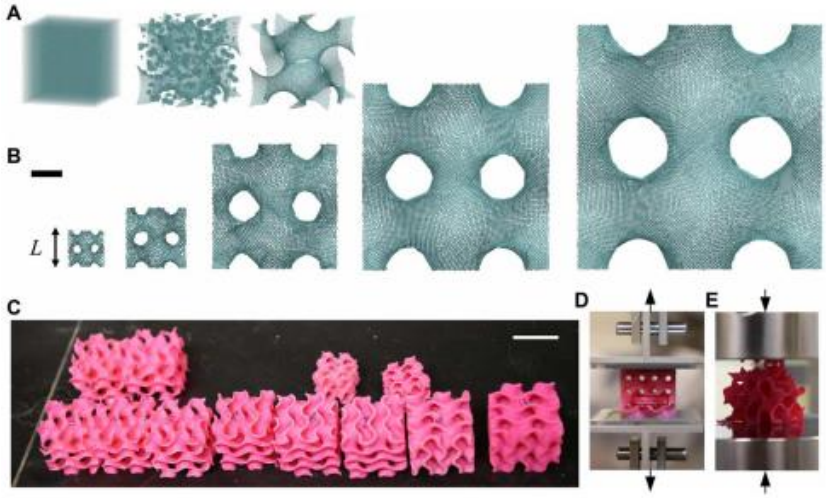

Figure 2.25 Modeling of the atomic 3D graphene structure with gyroid geometry, 3D-printed samples and tensile and compressive tests. (Quin et al., 2017)

New findings with single material bioinspired structures have shown important aspects of unusual geometrical configurations in tuning engineering properties, regardless of the composition of the material itself. Nonetheless, biological materials are composed of two main structural categories: nonmineralized, known as “soft” structures, and “hard” structures, which are composites of minerals and fibrous organic biopolymers (Yang et al., 2018). In order to fully imitate some biological materials and structures, multimaterials and composites have been investigated. Typical biological composite topologies such as bone, hexactinellid sponges and nacreous abalone shell, with brick-and-mortar architecture, have been emulated using multi-material 3D printing and computer simulations. The studies revealed toughness emerging from the

synergetic effects of a load-bearing stiff anisotropic phase (bricks) and a soft and ductile polymer matrix (mortar), confirming that the mechanical behavior of structures can be enhanced by using specific topological arrangements of soft and stiff phases as a design mechanism (Figure 2.26 and Figure 2.27). (Dimas et al., 2013; Mirzaeifar et al., 2015; Libonati et al., 2016; Gu et al., 2017; Tran et al., 2017; Frolic et al., 2017).

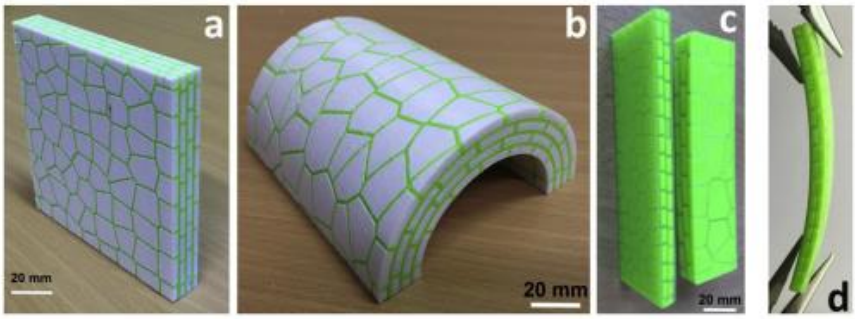

Figure 2.26 3D Printed nacre-like composite prototypes of different shapes and material combinations. (Tran et al., 2017)

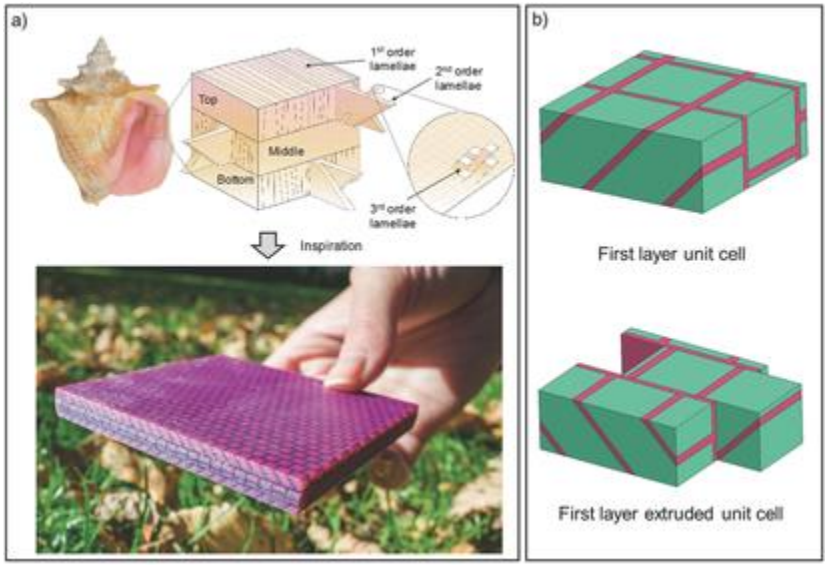

Figure 2.27 Conch shell-inspired structure fabricated via additive manufacturing, with cell is composed of a stiff (green) and soft (pink) material. (Gu et al., 2017)

Fu et al. (2011) emulated nature's design by direct-ink-write assembling of glass scaffolds with a periodic pattern, and controlled sintering of the filaments into anisotropic structures (Figure 2.28). Their porous glass scaffold presented high compressive strength with high porosity.

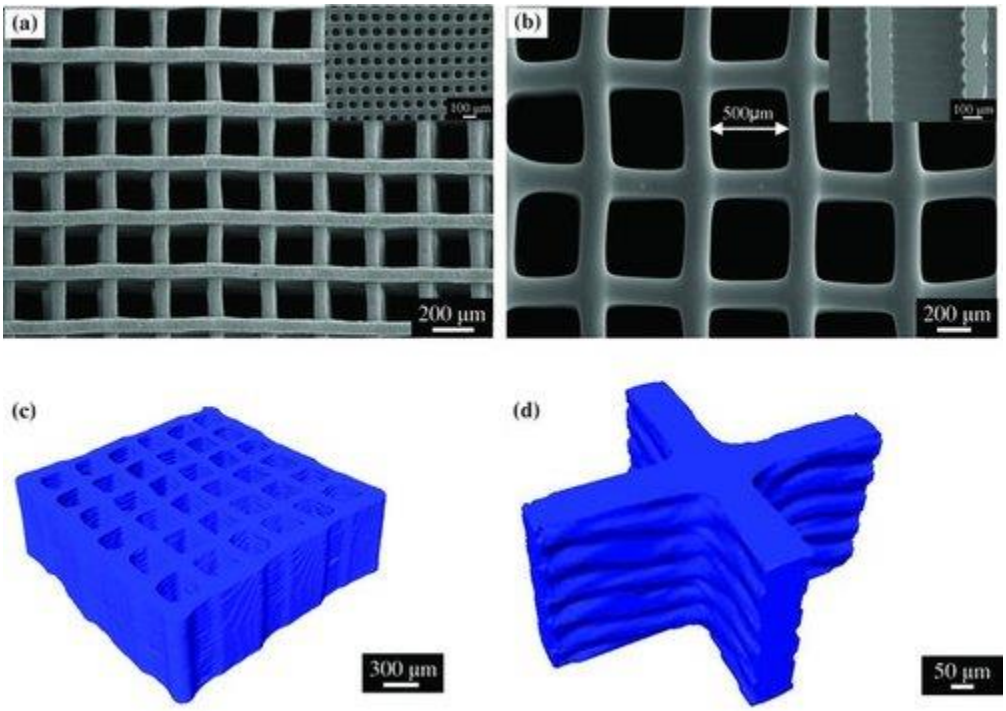

Figure 2.28 3D printed 6P53B glass scaffolds with a periodic pattern. (Fu et al., 2011)

To create hierarchical structures inspired by balsa wood, Compton and Lewis (2014) reported a new epoxy-based ink, which enables 3D printing of lightweight cellular composites with controlled alignment of multiscale and high aspect ratio fiber reinforcement (Figure 2.29).

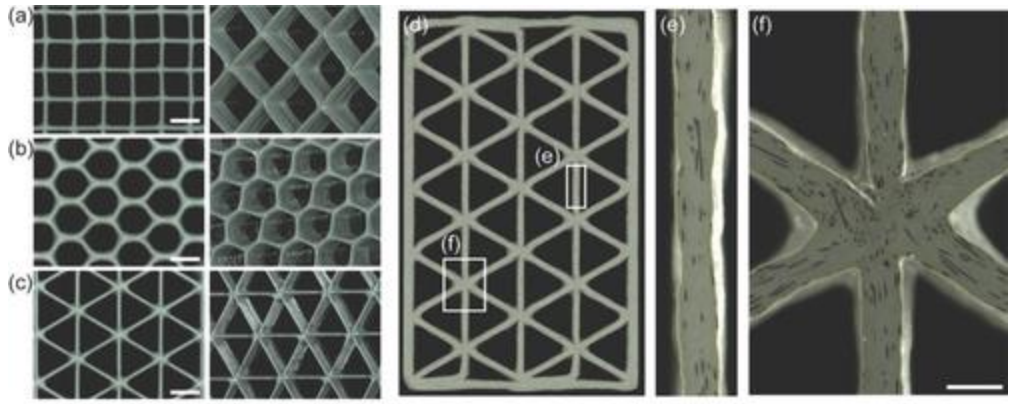

Figure 2.29 Cellular structures 3D printed with SiC-filled epoxy. (Compton and Lewis, 2014)

Sajadi et al. (2018) conveyed the schwarzite atomic structure, which is a 3D porous solid with periodic minimal surfaces and negative Gaussian curvature, to the macroscopic scale using 3D printing (Figure 2.30). A combination of experiment and molecular dynamics simulation shows that these structures are high load bearing and impact-resistant materials due to a singular layered deformation mechanism that develops during loading.

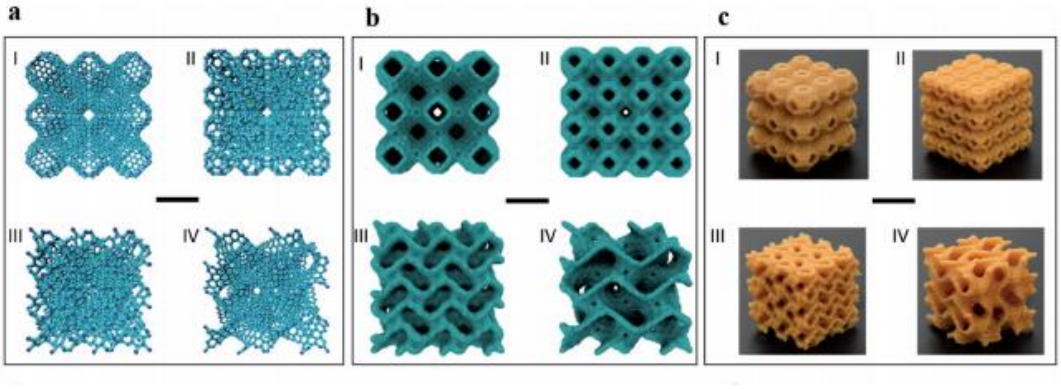

Figure 2.30 3D printed Schwarzite structures mimicking the molecular structures. (Sajadi et. al, 2018)

Nguyen-Van et al. (2020) produced lightweight cellular specimens made of cement mortar with 3D printed sacrificial thermoplastic Polylactic Acid (PLA) molds and demonstrated the mechanical responses of cellular blocks with experimental results and numerical simulation

(Figure 2.31). The cellular structures investigated are promising for a wide range of applications such as coastal protection blocks, lightweight bricks, noise barrier wall panels for highways and railways.

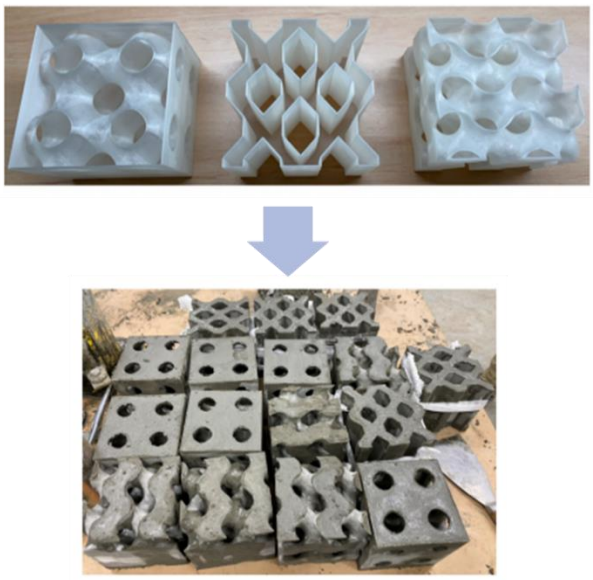

Figure 2.31 3D printed molds with sacrificial thermoplastic PLA material and resulted cellular blocks from filling fresh cement mortar into molds. (Adapted from Nguyen-Van et al., 2020)

2.4 Mechanics of Brittle Materials

The materials which align well with the AM processes most likely to be used in construction are either bonded particulates or hardened pastes, both of which tend to behave like brittle materials. The mechanical behavior of a material describes its response to external applied forces. This response includes deformation and fracture, which are sensitive to defects, temperature, and rate of loading. Deformation is the change in the contour of an object. An elastic deformation occurs under small stresses and when the stress is released the material returns to its original shape. On the other hand, plastic deformation is caused by larger stresses and the material's original form is never reached again. Normally, structures are sufficiently stiff and have

a high resistance to deformation, so that they remain in their design shape while in service. Fracture occurs when the material breaks into more than one piece. A material is considered brittle if fractures arise with little plastic deformation, and ductile if extensive plastic deformation precedes fracture (Hosford, 2010).

The principal mechanical properties of a material are stress (σ), strain (ε), Young's Modulus (E) and Poisson's ratio (υ). Stress represents the intensity of a force at a point and is defined as the force (F) applied divided by the area (A) subjected ($\sigma = F/A$). A normal stress (σ) is caused by a force acting perpendicular to the area, and it can be compressive or tensile. Forces acting parallel to the area cause a shear stress (τ). Strain means the amount of deformation that the material is subjected to. Normal strain is defined as the length variation of a material in extension (tensile) or compression (compressive) o$\varepsilon = \Delta L/L_0$). In brittle materials (e.g., crystalline materials), the elastic strain is small, usually less than 0.5%. For isotropic materials, which have$\varepsilon_z = \sigma_z/E$, where E is Young's$\varepsilon_x = \varepsilon_y = -\upsilon\varepsilon_z$, where υ is Poisson's ratio. For most materials, Poisson's ratio ranges between 0.2 and 0.4 (Hosford, 2010).

Common mechanical testing to achieve these properties are axial tensile and compression tests. With Plasticity Theory, tensile and compressive data can be used to predict a material's behavior under other forms of loading. Usually, the elementary concern is the strength of the material. The maximum compressive stress a material can carry is called the ultimate compressive strength, and the same applies to the maximum tensile strength, which is called the material's ultimate tensile strength. For brittle materials, compression tests can achieve notably higher strains and stresses compared to tensile tests. However, there are two undesirable factors during compression tests: friction and buckling. Friction between the ends of the specimen and the plates of the machine restrains the lateral spreading of the material near the extremities. Buckling is

expected to occur if the sample is excessively long or slender, commonly with height-to-diameter ratio greater than about 3. Brittle materials fail in compression by shear fractures on planes normally around 45 degrees to the compression axis (Hosford, 2010).

Besides strength, it is also important to know a material's ductility, which represents how much it can deform before fracturing, and it is related to the toughness of the material. Toughness is the energy the material can absorb without fracturing, or the material's resistance to fracture when stressed. A material can have a ductile or brittle fracture, depending on the amount of deformation present. Failures can also be classified as intergranular, when a crack propagates along grain boundaries, or transgranular, when a crack travels through the grain of the material. A brittle fracture can be intergranular or occur by cleavage. Intergranular fracture occurs when crystal structures have brittle grain boundaries, which are easy fracture paths. Cleavage fractures occur when crystal structures have crystallographic planes (cleavage planes). As shown in Figure 2.32, cleavage occurs when the normal stress across a cleavage plane (σ_n) reaches a critical value (σ_c). The toughness of brittle materials depends on grain size. The smaller the grain size, the greater the toughness. This can be explained by the fact that cleavage fractures need to reinitiate at each grain boundary, thus there are more grain boundaries with smaller grain sizes.

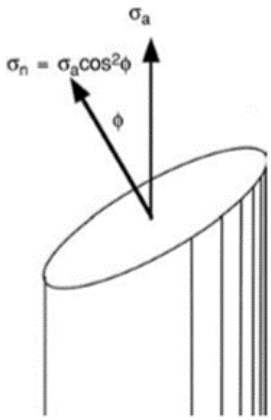

Figure 2.32 Cleavage fracture: cleavage plane and applied stress. (Hosford, 2010)

Brittle materials lack stress relief mechanisms to prevent the formation and propagation of cracks. This results in cracks growing to failure at stresses notably less than in ductile materials (e.g., metals). Also, defects (or flaws) in brittle materials can lead to faster crack formation and growth. Brittle failure typically begins from small cracks at the surface of an object that are produced during machining, finishing, or handling processes. The fact is that all brittle materials contain such flaws, even the strongest ceramic (i.e., pristine glass fibers) include small flaws on its surface. The size of flaws in real components can range between 10–200 μm. The strength of a component is then subjected to the size and shape of such flaws (i.e., flaw severity), and their location with respect to internal tensile stresses. Brittle fracture is calculated by a statistical process, where failure begins from the most severe flaw located in the region of highest tensile stress (Freiman & Mecholsky, 2012).

The higher uniaxial strength in the compression of brittle materials is explained by the presence of these flaws because of the stress-concentrating effect of defects under tensile loads. The failure of brittle materials in compression generally starts with stable microfractures and crack growth. The agglomeration and succeeding linking together of these small cracks result in a

catastrophic macroscopic failure (Brezny and Green, 1993). Sammis and Ashby (1986) studied the damage mechanics of dense and porous brittle solids in compression and concluded that the porosity of the material can express flaws, and thus impact the mechanical behavior of brittle solids.

2.5 Two-dimensional Cellular Solids

Periodic cellular solids are those composed of an interconnected network of struts or plates, which form the edges and faces of cells, filling a space (Gibson and Ashby, 1997). Their use extends the range of properties available to engineering. For example, they can provide low densities for the design of light and stiff members such as sandwich panels used for modern aircraft, large portable structures, and flotation components. Low thermal conductivity can also be obtained, allowing cheap and reliable thermal insulation. They are also appealing for energy-absorbing applications, such as packaging, because of large compressive strains that can be provided.

Periodic cellular structures formed of a two-dimensional array of polygons packing to fill a plane are called "honeycomb" structures in the literature, even if the unit cells do not have hexagonal geometry. In addition to the different shapes of a unit cell (i.e., squares, triangles, hexagons, etc.), there is also more than one approach to combine them, giving structures which differ in edge connectivity and properties. It is constructive, from a geometric perspective, to analyze a cellular structure in terms of v*ertices*, joined by *edges*, which envelope *faces,* enclosing *cells.* The quantity of edges in a polygon is designated here as *n*, and the quantity of edges meeting at a vertex is the edge-connectivity, Z_e. Figure 2.33 shows different assemblages for the same unit cell filling a space in a cellular solid. Figure 2.33(a) shows a packing

of equilateral triangles with Z_e = 6 and n=3, and (b) with Z_e = 4 and n=4. Figure 2.33(c) illustrates a packing of squares with Z_e = 4 and n = 4, and (d) with Z_e = 3 and n = 5. Figure 2.33(e and f) present packings of hexagons, regular and irregular, respectively, with Z_e=3 and n=6. For this study, three-dimensional cells were obtained extruding two-dimensional cells in a third direction. Figure 2.34 shows three-dimensional shapes for cells that can be packed together to fill space: a triangular prism (a), a square prism (b), and a hexagonal prism (c), respectively.

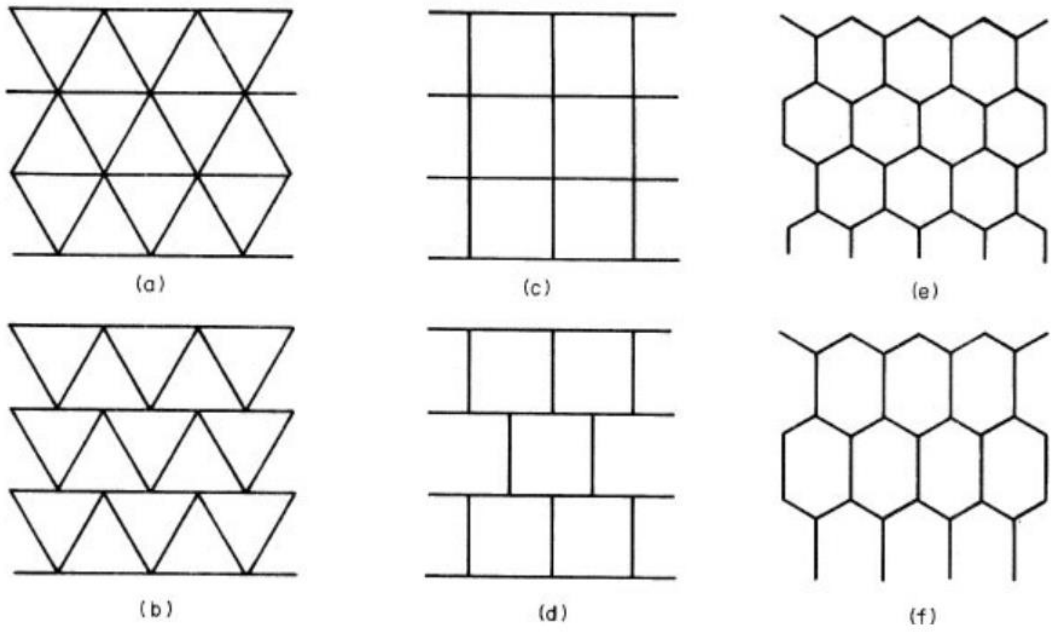

Figure 2.33 Unit cells filling a space in a cellular solid. (Gibson & Ashby, 1997)

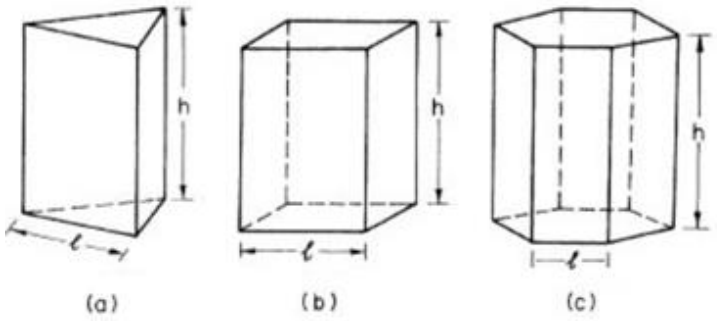

Figure 2.34 Three-dimensional unit cells to fill a space in a cellular solid. (Gibson and Ashby, 1997)

The properties of any cellular solid rely on the way the solid is distributed about the cell faces and edges. The significant structural characteristics of a cellular solid are: relative density (E^*/E_s), which is the density of the cellular object (E^*) divided by the one that the solid is made with (E_s); cell size; cell shape; topology, if it is constitute of two-dimensional or three-dimensional cells (foams); and the connectivity of cell edges and faces.

Besides the geometric properties, periodic cellular solid characterization depends on the properties which are inherent to the material the cell walls are made of. The cell wall material properties relevant in this study are the density, ρ_s, the Young's modulus, E_s, the plastic yield strength, σ_{ys}, the fracture strength, σ_{fs} and Poisson's ratio υ_s. Herein, the subscript refers to the solid cell wall material and the superscripted '*' indicates the cellular solid itself.

It is important to understand the mechanics of cellular solids if they are going to be used in load–bearing structures. A two dimensional cellular solid can be loaded *in-plane*, that is when the stress acts in the plane of cell edges (X_1-X_2 plane in Figure 2.35), or *out-of-plane*, when the stress acts perpendicular to the plane of cell edges (X_3 direction in Figure 2.35). In the last case, stiffnesses and strengths are much larger because they require the axial extension or compression

of the cell walls. On the other hand, the *in-plane* mechanical properties are lower because stresses in this plane make the cell walls bend, like shown in Figure 2.36.

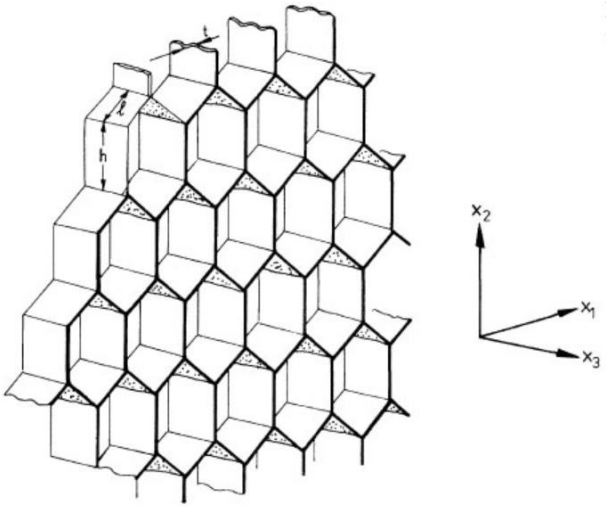

Figure 2.35 Periodic cellular solid with hexagonal cells and reference coordinate. (Gibson & Ashby, 1997)

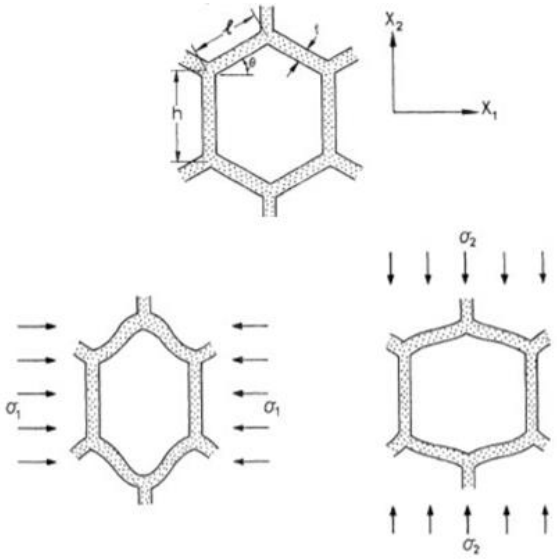

Figure 2.36 Example of hexagonal unit cell being compressed in-plane. (Gibson & Ashby, 1997)

Therefore, compression applied out-of-plane was considered in this study to achieve the best performance of the cellular solid. The function of the cellular solids in this research is to carry

normal loads in the longitudinal axis direction of the cylinders and prisms. In this course of action, expressive axial deformations of the cell walls develop in the initial linear-elastic regime, followed by the collapse, which could be by buckling (elastic, plastic or rigid) or brittle crushing. Gibson and Ashby (1997) proposed the following stress–strain curves for this scenario with a range of relative densities as shown in Figure 2.37.

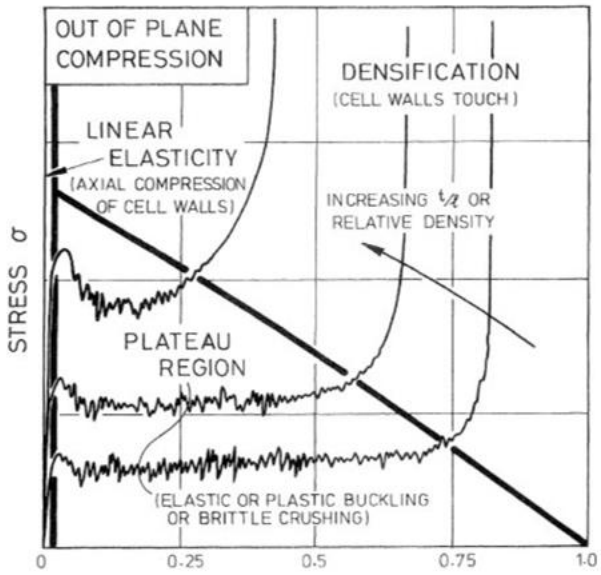

Figure 2.37 Stress-strain curve showing regimes of linear elasticity, collapse and densification for different relative densities of cellular solids. (Gibson & Ashby, 1997)

2.5.1 Cellular cores for sandwich panels

The behavior of honeycomb panels under compressive loads has been investigated by many researchers analytically and experimentally. These studies have been carried out on the out-of-plane axis (i.e., flatwise) and on the in-plane axis (i.e., edgewise), for bare honeycomb core or complete sandwich panels, and under quasi-static or impact loads. As mentioned, thin-walled structures are much stiffer under axial loading than in bending, which is the reason why honeycomb structures are stronger in the out-of-plane direction rather than in the in-plane direction. Wierzbicki (1983) investigated the crushing behavior of metal honeycomb cores, such

as aluminum and mild steel in this direction, and identified the folding and rolling of the walls as the principal types of deformation for these materials (Figure 2.38).

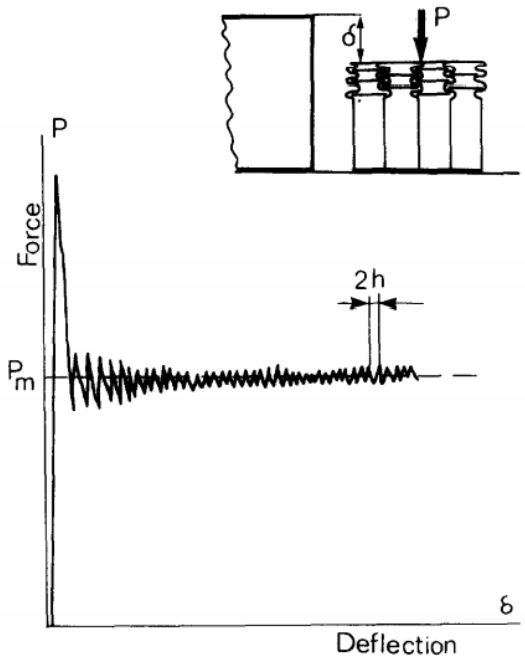

Figure 2.38 Typical force-displacement characteristics of compressed metal honeycomb. (Wierzbicki, 1983)

Zhang and Ashby (1992) studied the out-of-plane deformation and failure mechanisms of honeycomb cores made out of Nomex, which is a flame-resistant meta-aramid material, related to nylon, yet more rigid (Mera and Takata, 2000). They identified two kinds of collapse during uniaxial compression: elastic buckling, with folds forming across the wall; and fracture, with stress reaching a maximum and then suddenly dropping to less than a third of the maximum stress. The later process was reported with audible cracking. They also stated that for rigid-plastic honeycombs, such as aluminum, plastic yielding dominates the failure mechanisms. Zhang and Ashby (1992) affirmed that for these two types of materials, aluminum and Nomex, the out-of-plane strengths are independent of height and cell geometry, however highly sensitive to the density of the honeycomb. Khan (2006) tested honeycomb core of aluminum with different

thickness in the flatwise position and also concluded that the compressive strength is not function of core thickness.

Wu and Jiang (1997) also studied the axial crushing of aluminum honeycomb. When loading was applied quasi-statically, the specimens exhibited the same sharp peak load, followed by series of oscillatory crushing loads as showed by Wierzbicki (1983). The progressive plastic-buckling waves and subsequent plastic folding of these cellular structures are shown in Figure 2.39. They also asserted that the number of cells under axial loading does not affect the crush strength of the honeycomb cellular solid.

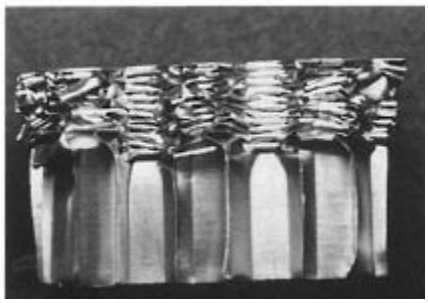

Figure 2.39 Progressive plastic-buckling waves and subsequent plastic folding of aluminum honeycomb cellular solids. (Wu and Jiang, 1997)

Studies have suggested that square-honeycomb cores with higher relative density would be preferred for impact loads, because of their combination of axial crushing resistance and in-plane stretching strength (Fleck and Deshpande, 2004; Xue and Hutchinson, 2004). Enhancement in the performance of cellular structures is expected when using materials with high strain hardening, such as stainless steel (Wierzbicki, 1983). Côté et al. (2004) examined the out-of-plane crushing characteristics of 304 stainless steel square-honeycomb. Their specimens tested under compression without facing sheets revealed a periodic axial-torsional buckling of the cells, as shown in Figure 2.40. During compression, the vertical node axis remains straight and cell wall

segments rotate about this axis. They found that the peak stress was insensitive to the ratio of height of core to cell size, yet it was affected by the relative density.

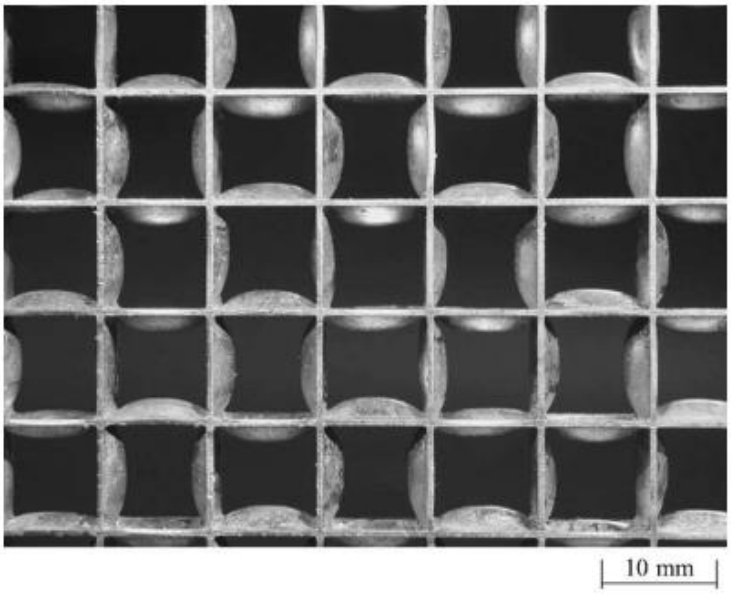

Figure 2.40 304 stainless steel square-honeycomb specimen showing axial torsional buckling mode. (Côté et al., 2004)

Côté et al. (2004) compared the mechanical behavior under compression of the steel square-honeycomb with a commercial aluminum alloy hexagonal-honeycomb (Figure 2.41). The aluminum hexagonal-honeycombs presented lower peak stress and faster softening after peak. It exhibited the expected oscillation in the plateau region corresponding to the formation of folds in the cell walls, which did not appear on the steel square-honeycomb. The difference in post-buckling response was associated with the different strain-hardening capacity of the materials. In such manner, the high strain hardening of the stainless steel restrains the formation of successive folds.

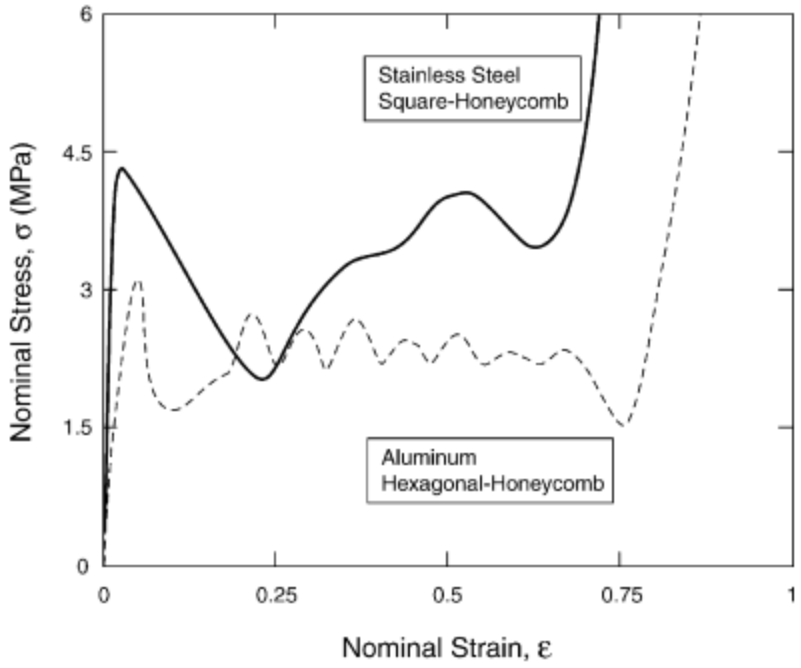

Figure 2.41 Comparison between compressive stress vs. strain response of typical stainless steel square-honeycomb and Al HexWeb hexagonal-honeycomb specimens. (Côté et al., 2004)

Aminanda et al. (2005) investigated the crushing phenomenon for honeycomb structures made of Nomex, aluminum alloy and drawing paper. The folding mechanism was observed for all three materials. The final deformation of the specimens is presented in Figure 2.42. The stress-strain curves followed the same pattern as previous studies on plastic-behaving materials.

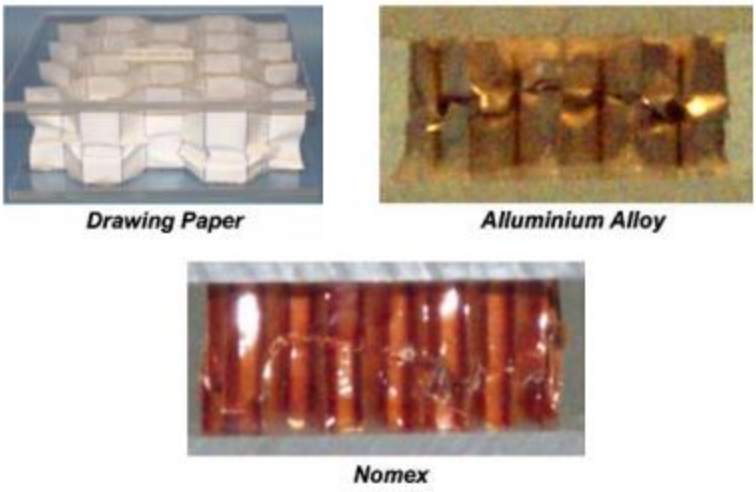

Figure 2.42 Folding deformation of honeycomb cores during out-of-plane uniaxial compression of three different materials: drawing paper, aluminum alloy and Nomex. (Aminanda et el., 2005)

A large number of studies have focused on the design optimization for load bearing metal cellular cores for sandwich panels, using beyond prismatic shapes, such as truss configurations and nano/micro lattices (Figure 2.43 and Figure 2.44) (Evans et al., 2001; Deshpande et al., 2001; Wicks et al., 2001; Chirras et al., 2002; Wadley et al. 2003, 2006; Jeong et al., 2013; Gumruk et al., 2013). However, little has been published on the properties and mechanisms of cellular solids made of brittle materials. Shahverdi et al (2017) studied the mechanical response of a fiberglass/phenolic honeycomb core, which is a more brittle material. However, compression tests were conducted in the in-plane direction (Figure 2.45). Failure modes were reported to occur by ribbon fracture or node bond failure (i.e., debonding of adhesive attachment).

Figure 2.43 Diamond shape 304 stainless steel textile sandwich panel. (Wadley et. al., 2003)

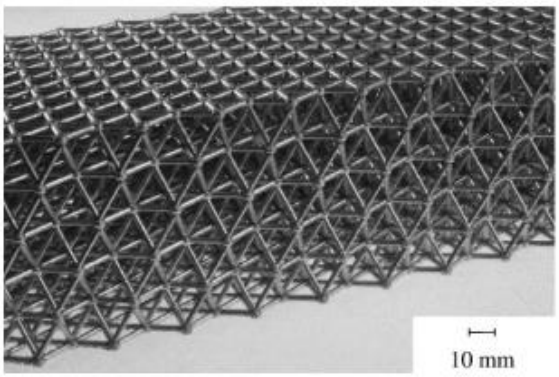

Figure 2.44 Octet-truss lattice core from casting aluminum alloy. (Deshpande et al., 2001)

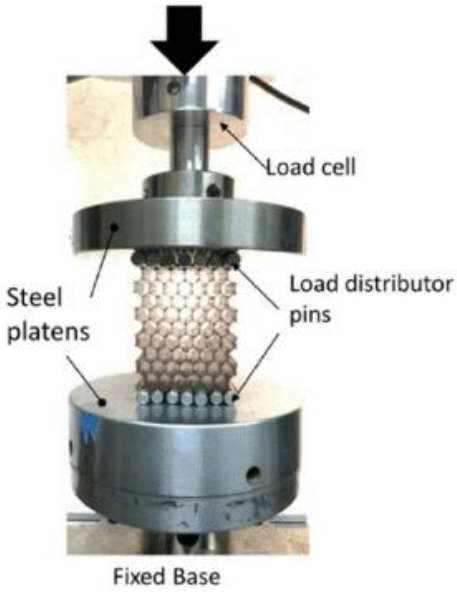

Figure 2.45 Compression test of fiberglass/phenolic honeycomb core on the in-plane direction. (Shahverdi et al., 2017)

The materials currently used to manufacture honeycomb structures are metal, Nomex, paper and Fiberglass. The manufacturing process of these structures requires the use of adhesives to bond sheets together. Liu et al. (2015) studied the bonding conditions between aramid paper sheets on a Nomex honeycomb core and found out that the debonding imperfections have significant effects on the mechanical behavior of the honeycomb structure. The issue of debonding between the adhesive cell walls could be overcome by the application of AM technologies. Additionally, AM technologies would allow for the comparison of different shapes of cellular structures composed of the exact same material. Using the same constituent material will eliminate one of the additional variables in many of the studies found in the literature, giving more confidence in the conclusions drawn.

2.5.2 Geocells

Periodic cellular materials are also currently being applied in geotechnical engineering with the utilization of geosynthetic geocells. 3D geocells are composed of an interconnected honeycomb-like network, which confines and stabilizes soils that would otherwise be unstable during loading (Figure 2.46). They are used in unpaved roadways, retaining walls, erosion control of slopes, and stormwater control in channels (Presto GeoSystems, 2020).

Geocell products are generally made of high-density polyethylene (HDPE), polyester or other polymer material, forming a flexible three-dimensional cellular structure. After being installed, specified infill materials are placed into it and compacted. This system can hold materials in place and prevent mass movements by providing confinement through tensile reinforcement and providing a free-draining system. Soils and aggregate infill materials have improved structural and functional behavior with the utilization of these cellular confinement systems (IFAI, 1970).

Figure 2.46 Aggregate confinement with geocell and on-site infill. (Presto GeoSystems, 2020)

A number of researchers have studied the performance of geocells for base and subgrade of unpaved roads and railways (Leshchinsky, 2012; Yang et al., 2012; Yang et al., 2013; Akpinar et al., 2018; Pokharel et al., 2018; Satyal et al., 2018), slope stabilization (Martin et al., 1998; Mehdipour et al., 2013; Mehdipour et al., 2017; Arvin et al., 2018) and seismic vibration isolation (Leshchinsky et al., 2009; Xinye et al., 2016; Ujjawal et al., 2019).

3 METHODOLOGY

3.1 Prototypes Design

Of the natural structures examined, four were chosen to be further investigated because of their likelihood of being effectively implemented in brittle materials. The biological structures chosen were Honeycomb, Toucan Beak, Plant Stalk and Horn. Table 3.1 provides a summary of these biological structures and the associated performance aspects targeted.

Table 3.1 Summary of biological structures and performance mechanisms examined in this study.

Biological Material/Organism	**Description of Hierarchical Microstructure or Cellular Pattern**	**Performance Mechanism**
Honeycomb	Arranged in a repeating hexagonal pattern	Efficient load support using very minimal amounts of material
Toucan Beak	Foam closed-cell structure built with bony struts in triangular cells	Low density and high stiffness
Plant Stalk	Composed of cells aligned parallel to the growth axis, which have a rectangular shape on the longitudinal axis	Decrease the weight of the structure and enhance flexure resistance
Horn	Filaments and matrix organized into circular lamellae that surround hollow tubules	Tough, resilient and impact resistant

Many of these biological examples have complex hierarchical structuring which spans several length scales. While this comprehensive function gives the composite material its improved performance, these complex assemblies are difficult to create within current additive manufacturing (AM) processes and it is unlikely that they would be implementable at field scale with this form of detail. Therefore, the focus of this particular study is on singling out the function that the periodic cellular pattern contributes to the overall behavior, as this is also a major macroscale feature leading to improved performance.

Prototypes inspired by their microscopic structuring were drafted using AutoCAD software, and virtual 3D representations describing the geometry were obtained as shown in Figure 3.1. The prototypes were designed to be 50 mm tall and approximately 47 mm wide, producing a height-to-width ratio of approximately 1 to avoid buckling during the uniaxial compression test. For the Toucan Beak, three additional configurations were designed varying the wall thickness, total cross-sectional area, and solid (material) cross-sectional area, as demonstrated in Figure 3.2. This separate parametric study was carried out to better understand how these features affect load transfer in these cellular structure designs. For each organism, a full solid part was also fabricated respecting the same contour, as presented in Figure 3.3, to obtain strength-to-weight comparisons. Cylinders with 12x24 mm and 20x40 mm (diameter x height), were also generated to track material properties.

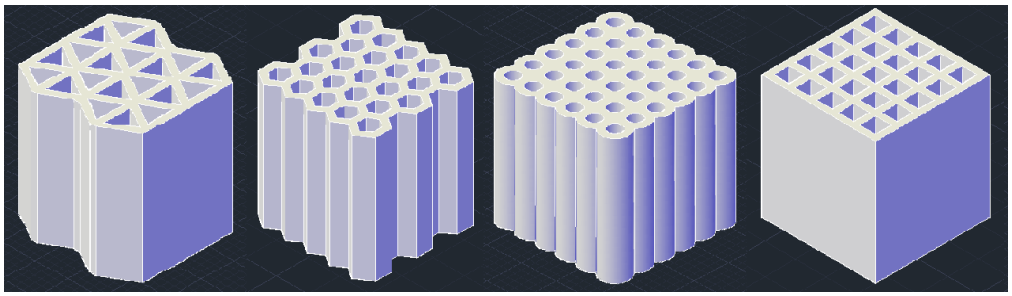

Figure 3.1 CAD 3D representation of the Toucan Beak, Honeycomb, Horn and Plant Stalk, respectively.

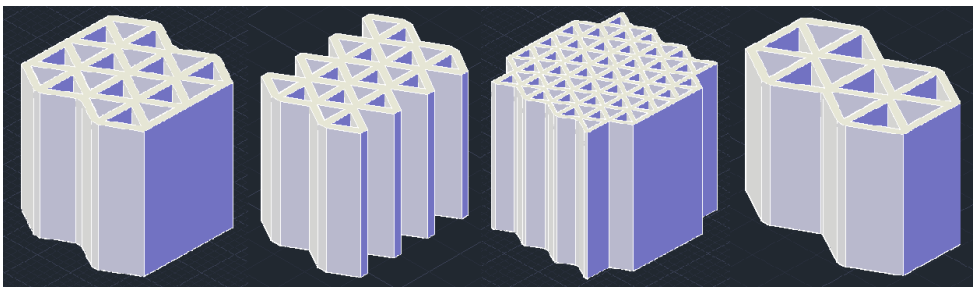

Figure 3.2 CAD 3D representation of the Toucan Beak variations: I, II, III and IV, respectively.

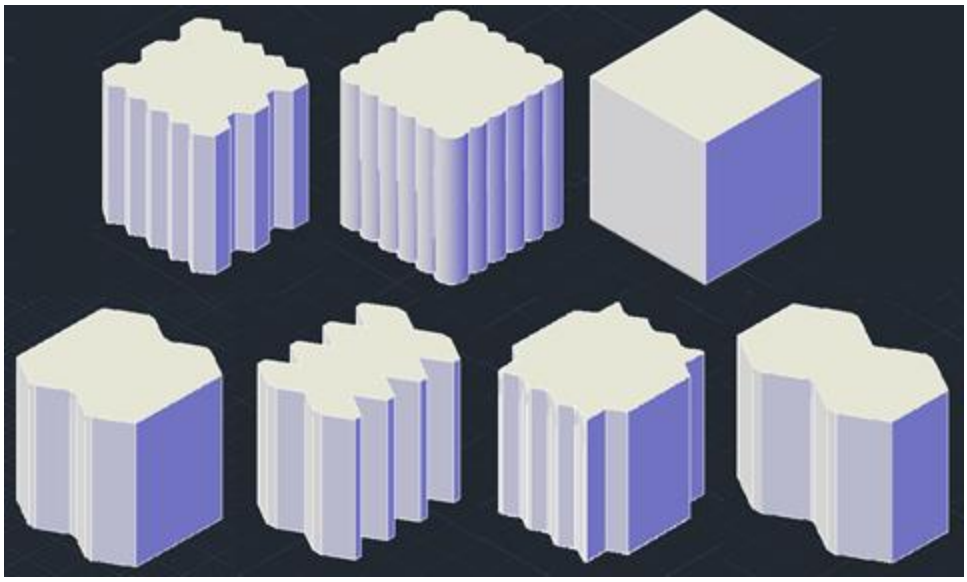

Figure 3.3 CAD 3D representation of full solid prototypes, Honeycomb, Horn, Plant Stalk, Toucan Beak I, II, III, IV, respectively.

3.2 Prototype Geometry

The Toucan Beak prototypes are formed of cells (pores) with triangular geometry imitating the foam closed-cell structure built with bony struts inside the Toucan Beak. The Honeycomb prototype is constituted of hexagonal cells. The Horn prototype is composed of pores with circular geometry mimicking the hollow tubules found in the microstructure of the Bighorn Sheep horn. The Plant Stalk prototype is organized in squared cells motivated by the longitudinal section of the Plant-Bird of Paradise.

Figure 3.4 to Figure 3.10 exhibit the cross-sections of all prototypes, including dimensions of sides or diameter, thickness of the walls, sides or diameter of the geometric cells (pores), and their respective connection configuration at a vertex. The Toucan Beak prototypes have 6 edges meeting at a representative vertex, therefore, an edge connectivity of Z_e=6. The Honeycomb has Z_e=3 and the Plant Stalk has Z_e=4. The Horn does not present straight edges meeting at a vertex, although there is still a curvilinear connection between cells. Dimensions and areas for the different

prototypes are summarized in Table 3.2 and Table 3.3, respectively. Figure 3.11 presents a schematic to aid understanding of the nomenclature for the different areas used to calculate stress in this study. The area used in the corresponding calculation type is shown by the shaded zones for each. These two areas were used because depending on the application, it may be relevant to consider just the area filled with solid material, for example when considering efficiency of material use, or it may be relevant to consider the whole area occupied by the structure.

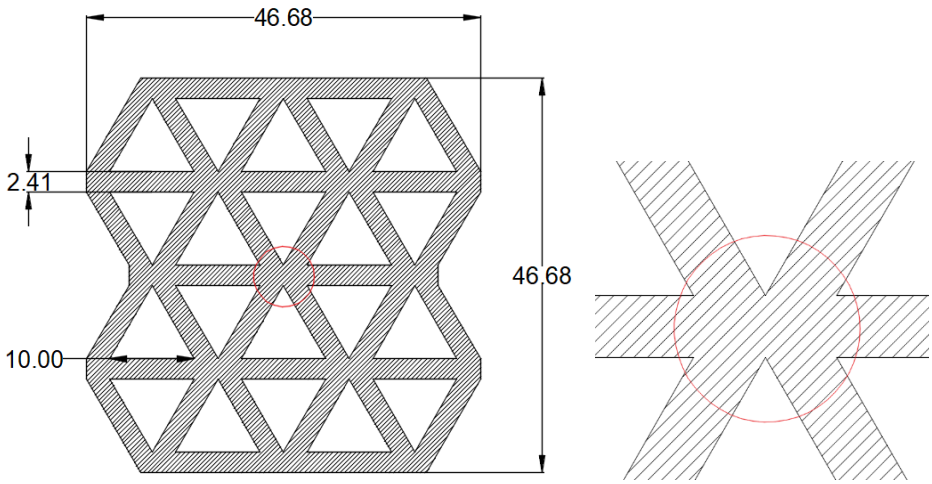

Figure 3.4 Toucan Beak I cross-section with dimensions in mm and representative edge connectivity (Z_e=6).

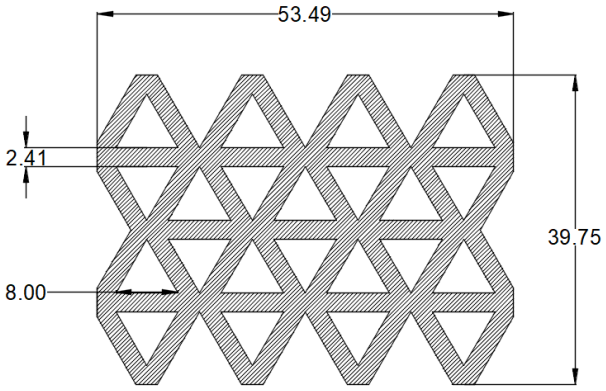

Figure 3.5 Toucan Beak II cross-section with dimensions in mm.

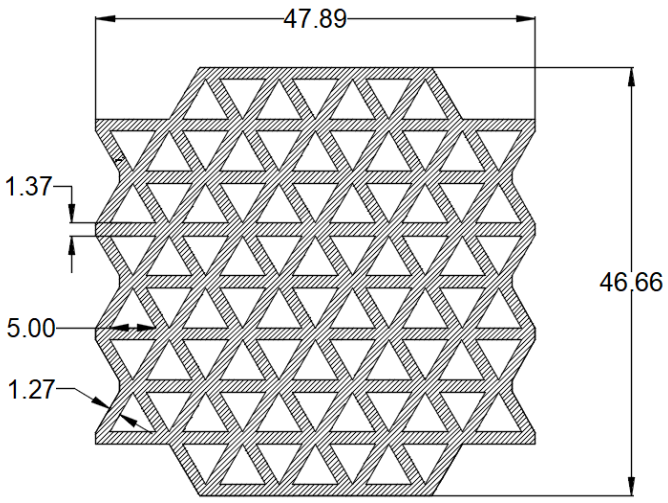

Figure 3.6 Toucan Beak III cross-section with dimensions in mm.

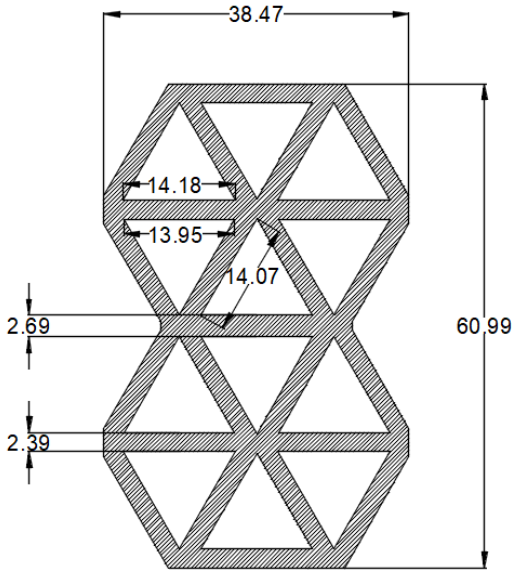

Figure 3.7 Toucan Beak IV cross-section with dimensions in mm.

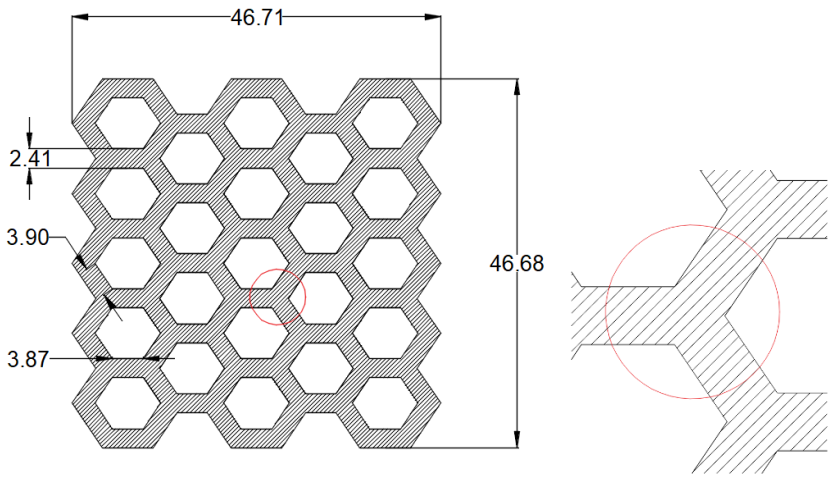

Figure 3.8 Honeycomb cross-section with dimensions in mm and representative edge connectivity (Z_e=3).

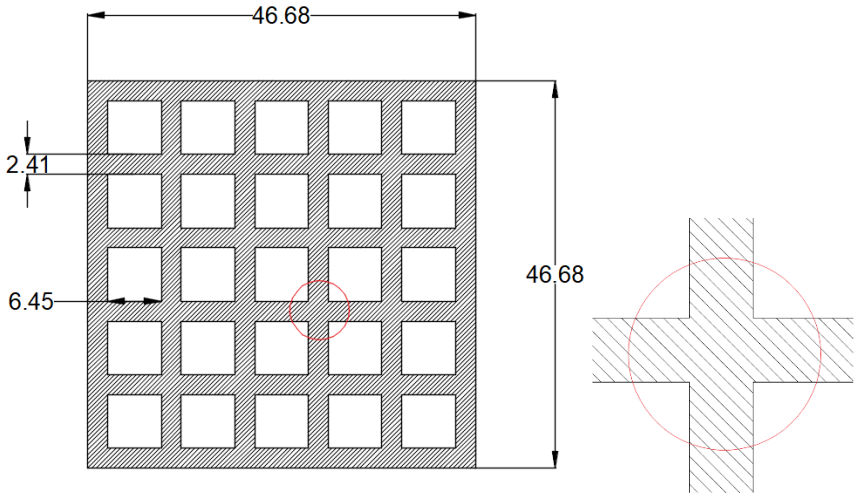

Figure 3.9 Plant Stalk cross-section with dimensions in mm and representative edge connectivity (Z_e=4).

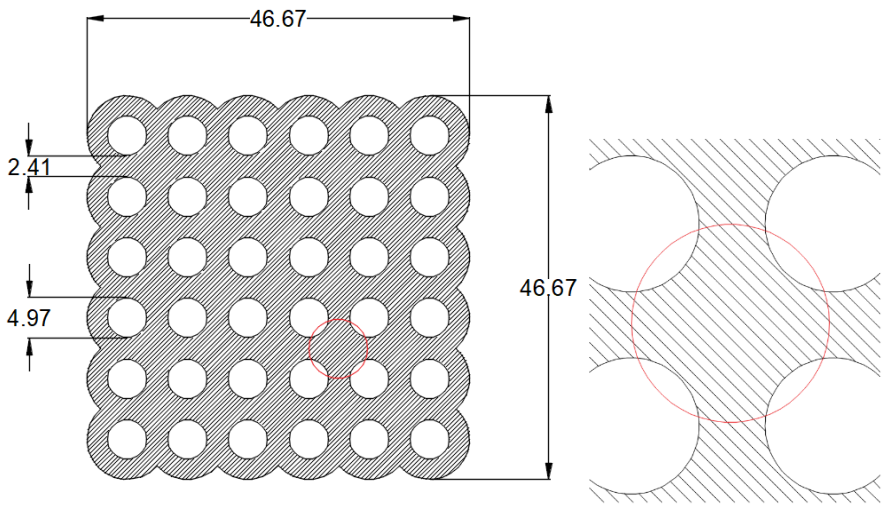

Figure 3.10 Horn cross-section with dimensions in mm and connectivity.

Table 3.2 Dimensions of prototypes.

	Side 1/ diameter (mm)	Side 2 (mm)	Cell side/ diameter (mm)	Wall thickness (mm)
Toucan Beak I	46.68	46.68	10	2.41
Toucan Beak II	53.49	39.75	8	2.41
Toucan Beak III	47.89	46.66	5	1.27-1.37
Toucan Beak IV	38.47	60.99	≈14.05	2.39; 2.69
Honeycomb	46.71	46.68	≈3.89	2.41
Horn	46.67	46.67	4.97	2.41
Plant Stalk	46.68	46.68	6.45	2.41

Table 3.3 Areas of prototypes.

	Gross Area (cm^2)	Material Area (cm^2)	Cell Area (cm^2)
Toucan Beak I	19.27	10.61	8.66
Toucan Beak II	16.72	10.63	6.10
Toucan Beak III	19.29	10.63	8.66
Toucan Beak IV	19.26	9.00	10.26
Honeycomb	19.09	10.09	8.99
Horn	20.82	13.83	6.98
Plant Stalk	21.79	11.40	10.39

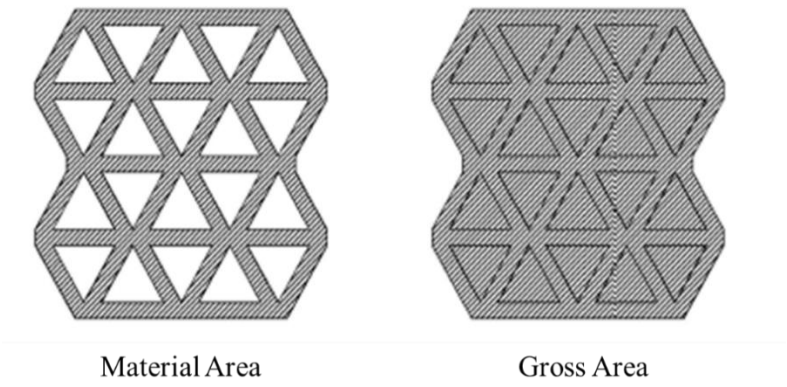

Figure 3.11 Representative schematic for the nomenclature of Areas.

For the Toucan Beak parametric study, Toucan Beak I was taken as the reference and each of the other designs differ from it in only one characteristic. Toucan Beak II has the same wall thickness and material area as Toucan Beak I but has a smaller gross area. Toucan Beak III has the same gross and material areas, but thinner walls. Lastly in Toucan Beak IV, most of the walls have the same thickness as Toucan Beak I and the same gross area; however, it has less material area.

Table 3.4 presents details about the geometry, including the shape of the cells, the number of edges in the specific cell, the representative edge connectivity of the cell's geometry, and the total quantity of cells in the prototype design. Table 3.5 shows a more detailed description of edge connections in the prototypes, including the total number of vertices (i.e., the number of points where edges meet), and the quantity of edges with each specific edge connectivity.

Table 3.4 Detailed geometry of prototypes.

	Cell geometry	Cell quantity	Edge quantity per cell	Cell edge connectivity (Z_e)
Toucan Beak I	Triangles	20	3	6
Toucan Beak II	Triangles	22	3	6
Toucan Beak III	Triangles	80	3	6
Toucan Beak IV	Triangles	12	3	6
Honeycomb	Hexagons	23	6	3
Plant Stalk	Squares	25	4	4
Horn	Circles	36	inf	-

Table 3.5 Detailed connectivity of prototypes.

	Quantity of Vertices (V)	Quantity of vertex with Z_e=6	Z_e=5	Z_e=4	Z_e=3	Z_e=2
Toucan Beak I	17	5	2	2	8	0
Toucan Beak II	22	8	2	0	4	8
Toucan Beak III	54	28	10	4	8	4
Toucan Beak IV	12	2	2	0	8	0
Honeycomb	66	0	0	0	44	22
Plant Stalk	36	0	0	16	16	4
Horn	-	-	-	-	-	-

3.3 3D Printer and Materials

The parts were 3D printed with the binder jetting printer ProJet 260C manufactured by 3D Systems Incorporated. The ProJet 260C specifications are: 20 mm/h deposition rate, build size (*l* x *w* x *h*) of 236 x 185 x 127 mm, resolution of 300 x 450 dpi, layer thickness of 0.1 mm, 604 nozzles in the inkjet printer head to disperse the binder, and the material is a polymer composite (Gibson et al., 2015). The 3D printer was maintained in a controlled environment at a temperature between 23°C and 25°C, and a relative humidity between 20 and 28 per cent.

The powder and binder used are also commercialized by 3D Systems. The powder is plaster based, more specifically calcium sulfate hemihydrate (CaS04 · 0.5 H20), and the binder is water based (2-pyrrolidone). Typically, these parts are infiltrated with epoxy strength infiltrates to improve their mechanical properties. Watters and Bernhardt (2017) studied the mechanical properties of parts with epoxy infiltration for the same printer and material. A new post-processing curing protocol was implemented to increase the maximum depth of infiltration and the strength of the parts improved significantly. However, this step was not included in this study because complete infiltration of the material was not possible for the solid specimens. Watters and Bernhardt (2017) showed that the epoxy infiltration was limited to approximately 12 mm depth. Because the solid specimens were approximately 50 mm in each dimension, the epoxy would have created a shell rather than a homogeneous material matching the periodic cellular specimens. Therefore, the specimens were tested in an uncured or "green" state.

The 3D printer allows the setting of shell saturation from 20 to 170 per cent and the core saturation from 0 to 340 per cent. Although previous studies (Vaezi & Chua, 2011; Fereshtenejad & Song, 2016) investigated the effect of binder saturation levels on the uncured part strength, the default binder saturation settings (100% shell and 100% core saturation level) were used in the study herein.

3.4 AM Process

The 3D models were exported from the CAD solid modeling software as a Standard Triangular Language (STL) file, which is the format that the 3D printer recognizes. The STL files were then opened in the 3D Systems software and could be manipulated to correct position and orientation in the build volume space of the 3D printer. Also, configurations such as binder saturation level were set. The objects were place vertically along the Z axis. Figure 3.12

demonstrates an example of parts organized in the build space of the ProJet 260C. The build volume space layout and configurations were then sent to the machine to be printed. Figure 3.13 shows the prototypes and cylinders during printing.

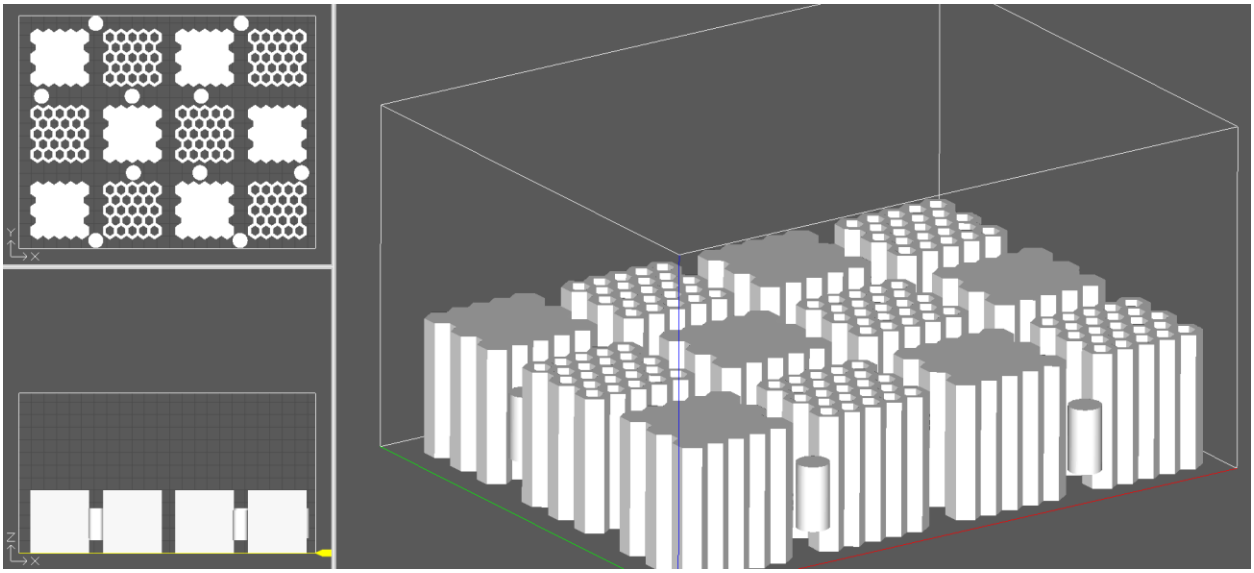

Figure 3.12 Organization of STL Files in the build volume space of ProJet 260C 3D printer.

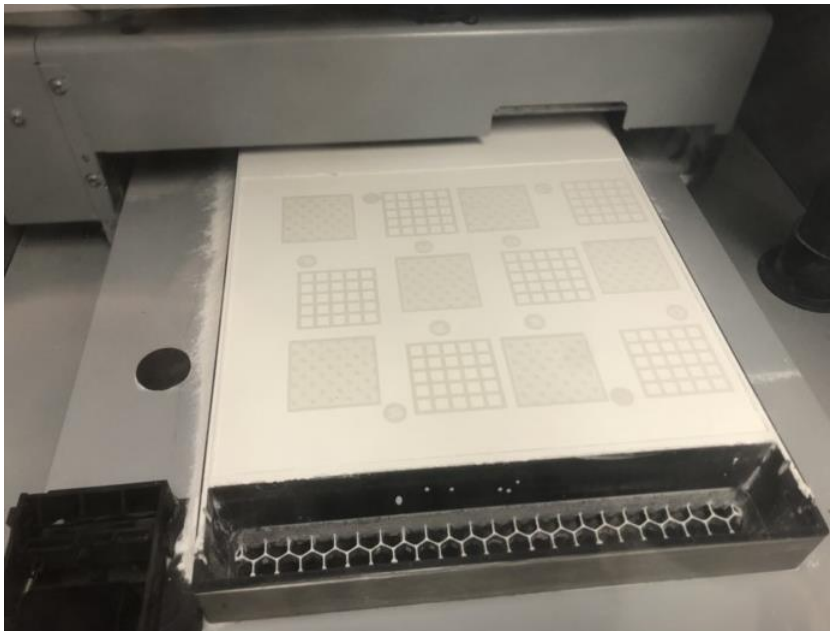

Figure 3.13 Prototypes and cylinders being printed in the build volume space of ProJet 260C 3D printer.

From Figure 3.14 it is possible to notice that the printing process uses different patterns (formed by different levels of binder saturation) for spreading binder across the cross-sectional area of the cellular and solid prototypes. The cellular objects appear to have the more saturated material throughout, while the solid objects consist of a more saturated shell, and a less saturated core, with dots of concentrated binder throughout. This was a limitation in this study which prohibited the direct comparison of the cellular and solids structures since they were, in fact, made of two different constituent materials. Therefore, the results presented in this thesis focus mostly on the strength-to-weight performance for each and the stress-strain responses are only briefly considered. Future efforts will be made to overcome this issue in the printer and obtain a more comparable set of objects.

Figure 3.14 Different printing patterns for cellular and solid structures.

Once the printing was complete, the parts were removed from the printer. In this study, the only post-processing procedure executed was the removal of loose powder from the objects. A Core Recycling Unit from *3D Systems, Inc*, equipped with an pressurized air nozzle and powder recycle system was used for cleaning the parts. Some specimens were left with the voids filled with powder, to simulate an in-situ process were the cleaning of the loose powder would be impractical. In some cases, where keratin or other infill material was present in the biological example, they could be simulated by a powder filled prototype. While this is not perfectly

analogous to the biological constituents, it was anticipated that the infill would change the load transfer mechanisms, which should also be better understood. For example, if the construction process matches the small-scale printing process, a layer of soil would be spread (and possibly compacted) followed by spray application of the binder in the chosen cellular pattern. Then another layer of soil would be spread, and the binder would be applied again. This process would continue until the subgrade reached the desired height. In this type of procedure, the cellular pattern would be filled with the excess soil (resulting in a soil matrix with a macro-fabric inclusion of solid material) and any behavior changes due to this infill must also be understood.

Dimensions of finished parts were measured using a digital caliper with 0.01 mm accuracy. Each dimension was measured three times, and the value reported was the average of the three. The parts were also weighed using a digital scale with 0.01 g accuracy. Figure 3.15 to Figure 3.21 show the finished 3D printed prototypes. Note that some of the specimens shown have already been tested at the time the picture was taken and any cracking or anomolies seen are after testing and are not present for the freshly printed specimens.

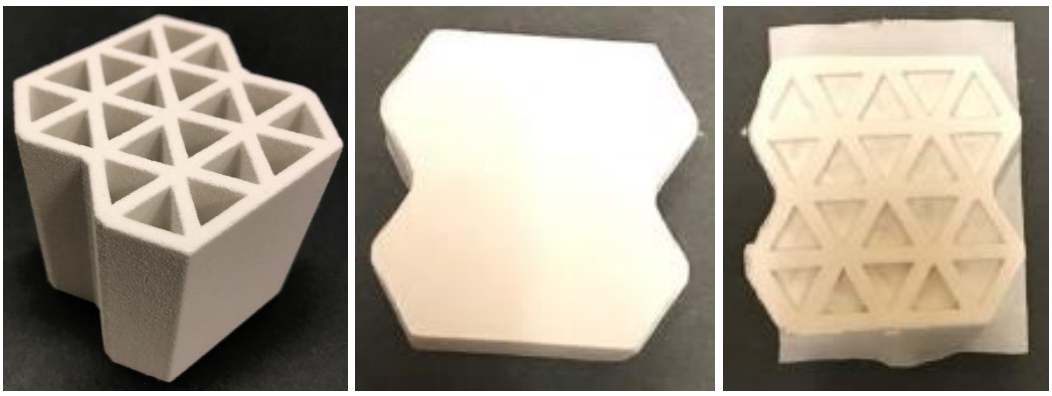

Figure 3.15 Toucan Beak I 3D printed prototype with cellular, solid and infilled cellular structures, respectively.

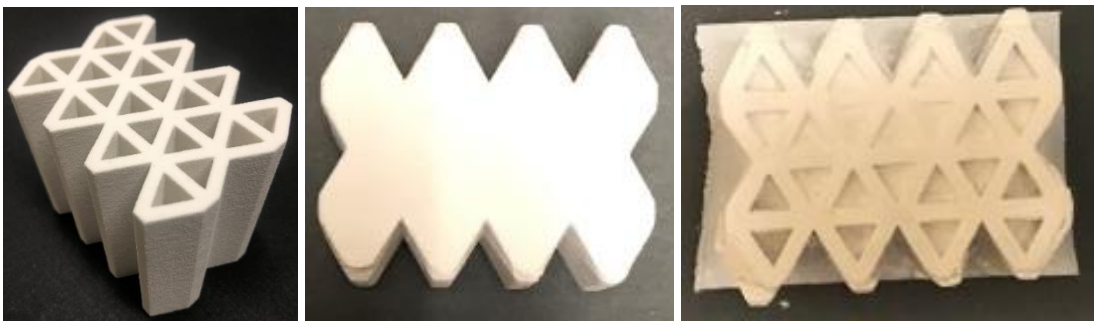

Figure 3.16 Toucan Beak II 3D printed prototype with cellular, solid and infilled cellular structures, respectively.

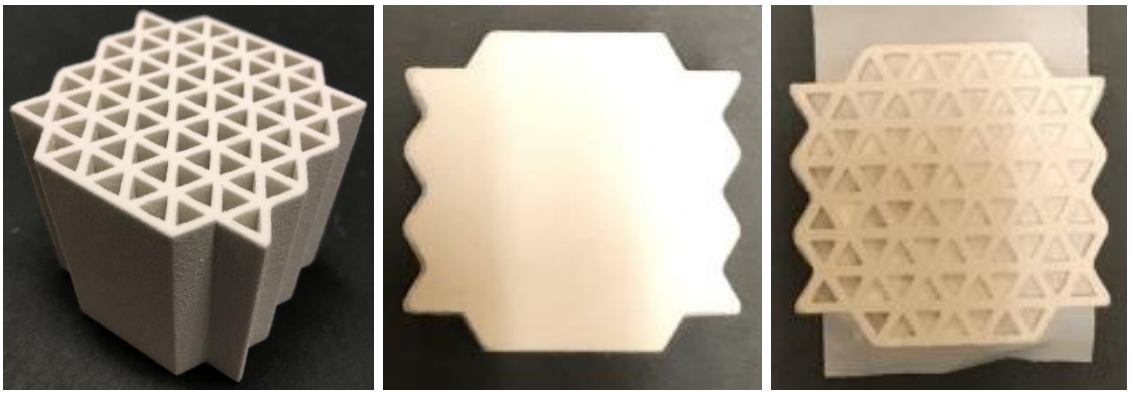

Figure 3.17 Toucan Beak III 3D printed prototype with cellular, solid and infilled cellular structures, respectively.

Figure 3.18 Toucan Beak IV 3D printed prototype with cellular, solid and infilled cellular structures, respectively.

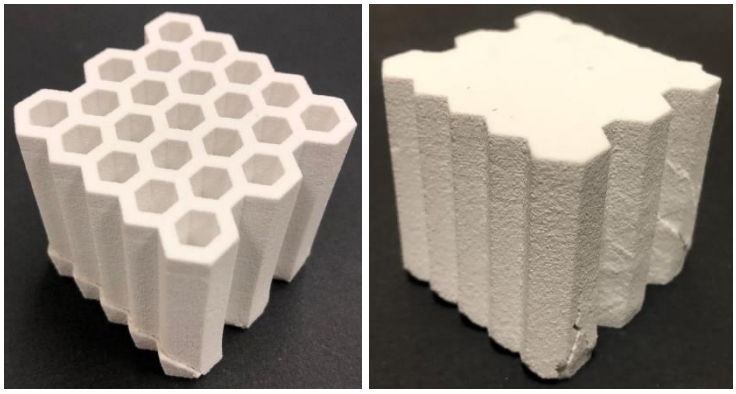

Figure 3.19 Honeycomb 3D printed prototype with cellular and solid structures.

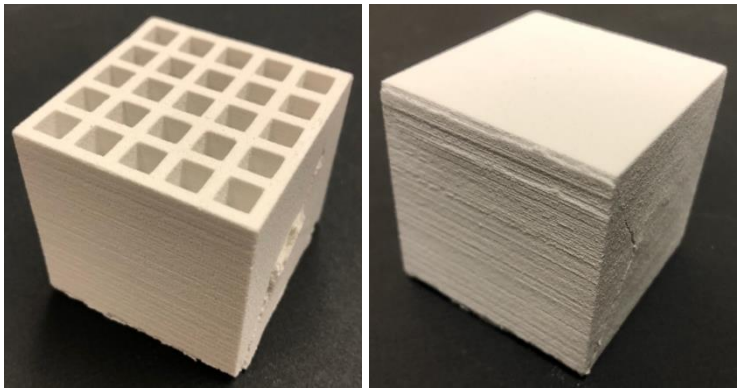

Figure 3.20 Plant Stalk 3D printed prototype with cellular and solid structures.

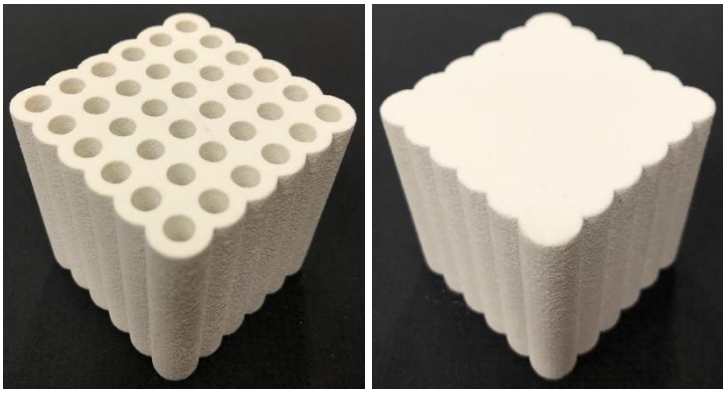

Figure 3.21 Horn 3D printed prototype with cellular and solid structures.

3.5 Uniaxial Compressive Test

Unconfined uniaxial compression tests were performed following the procedures defined in ASTM C39/C39M-20 for cylindrical concrete specimens (ASTM, 2020). A hydraulic controlled loading frame manufactured by MTS Systems Corporation was used to test the cylinders using a load transducer with a capacity of 4.45 kN. The Sigma-1 Automated Load Test System from GEOTAC was used with a 44.5 kN capacity load cell to test the bio-inspired specimens. A constant displacement rate of 0.0063 mm/s was used to test all specimens. In addition, a 12.5 mm gauge length extensometer also from MTS was used while testing the cylinders to minimize the boundary effects and obtain a more precise measurement of Young's modulus. Figure 3.22 12x24 mm cylinder being tested under uniaxial compression with MTS loading device and extensometer. and Figure 3.23 Prototype being tested under uniaxial compression with GEOTAC loading device. show the set up for the cylinders and prototypes being tested.

Figure 3.22 12x24 mm cylinder being tested under uniaxial compression with MTS loading device and extensometer.

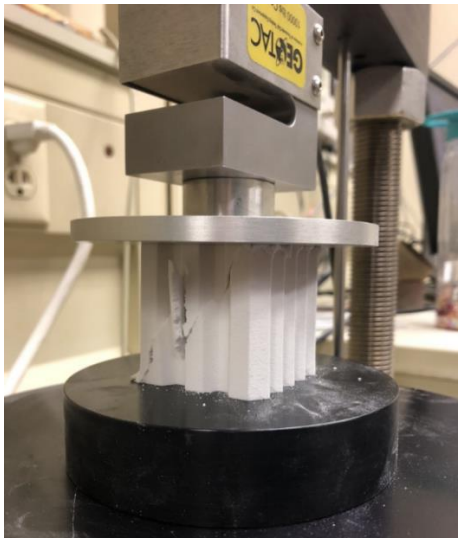

Figure 3.23 Prototype being tested under uniaxial compression with GEOTAC loading device.

3.6 Calculations and Plots

A MATLAB code was written to read the output files from the loading machine programs, calculate properties such as densities, maximum stresses, Young's modulus, strain at the peak stress of the samples, and plot stress versus axial strain curves and contour plots for material proprieties across the build volume of the 3D printer.

4 RESULTS AND DISCUSSION

4.1 Material Properties and Variability

Upon initial testing of the cylinders and the biological structures, it was determined that the printing process, ambient laboratory conditions, and the testing scheduling (e.g., relative humidity, and days between printing and testing) were influencing the results. It was important to ensure that the differences observed in the periodic cellular structure results were due to the biological feature and not the printing or experimental procedures. Because only a few replicates could be printed together in the same batch, it was important for the properties to be tracked from batch to batch. Therefore, 10 cylinders (12mm diameter x 24 mm height) were printed in each batch with the bio-inspired prototype structures. The batches were observed to vary quite significantly, but it was later determined that the variation was due to two main factors, (1) the location of the specimen in the printer, and (2) the time between printing and testing.

To better understand the first factor, a batch of 39 cylinders was printed and the location within the printer bed was tracked. All 39 cylinders were tested the same day and they were oven dried prior to testing. Figure 4.1 illustrates the build volume within the 3D Printer and the coordinate origin and axes adopted to analyze the results, and Figure 4.2 presents the organization of the cylinders within the build chamber. The properties determined for cylinders in this batch, including mass, height, density, ultimate compressive strength (UCS), strain at peak stress (SPS), and Young's Modulus (E) are summarized in Table 4.1 Cylinder properties at different layers of build volume of 3D Printer.. Statistical values including the mean, standard deviation (SD), and coefficient of variance (COV) are reported for each layer, as well as for the entire group. Note that an Analysis of variance (ANOVA) will be conducted in the future to evaluate the significance

of groups within this study. Figure 4.3 shows the stress-strain curves for cylinders at different layers of the build volume of the 3D printer.

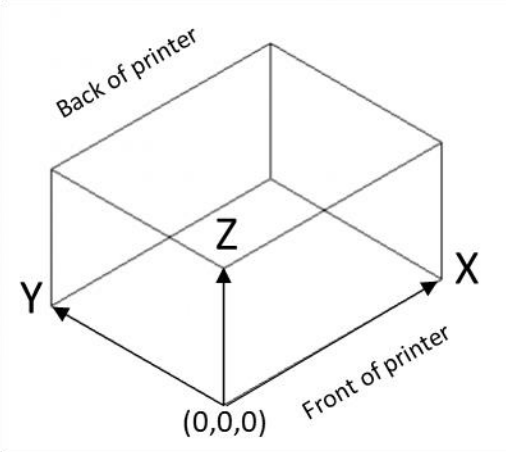

Figure 4.1 Representation of build volume of 3D printer with coordinates.

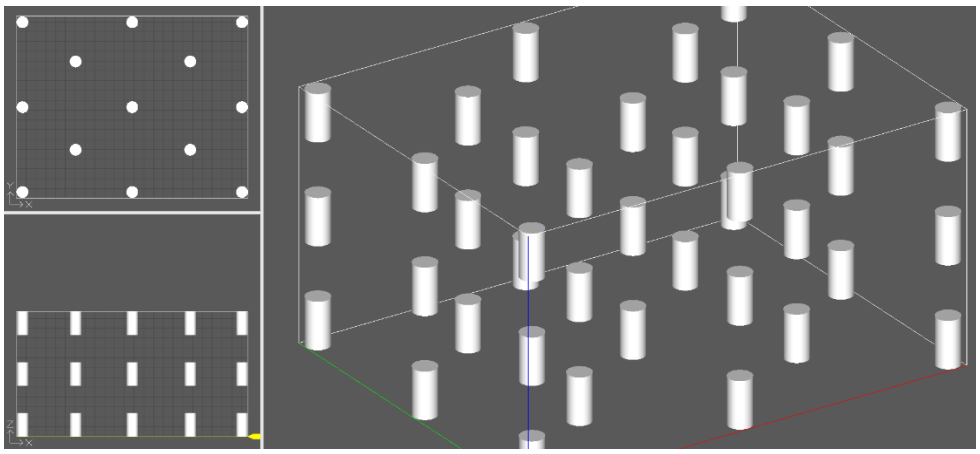

Figure 4.2 Organization of cylinders in the build volume of the Project 260C 3D printer.

Table 4.1 Cylinder properties at different layers of build volume of 3D Printer.

		Mass (g)	Height (mm)	Density (g/cm3)	UCS (kPa)	Strain at Peak Stress (%)	Young's Modulus (GPa)
Bottom Layer	**Mean**	3.59	24.33	1.25	4876	2.98	1.27
	SD	0.09	0.13	0.03	835	0.72	0.45
	COV (%)	2.57	0.51	2.56	17.13	24.04	35.33
Middle Layer	**Mean**	3.71	25.21	1.25	4986	3.27	1.10
	SD	0.07	0.42	0.03	827	0.95	0.63
	COV (%)	1.78	1.67	2.04	16.58	28.95	57.28
Top Layer	**Mean**	3.85	26.93	1.22	3713	7.12	0.11
	SD	0.09	0.40	0.03	794	1.82	0.07
	COV (%)	2.39	1.49	2.39	21.37	25.55	64.43
Mean		3.72	25.50	1.24	4512	4.49	0.82
SD		0.14	1.15	0.03	1002	2.28	0.68
COV (%)		3.69	4.50	2.65	22.22	50.86	83.33

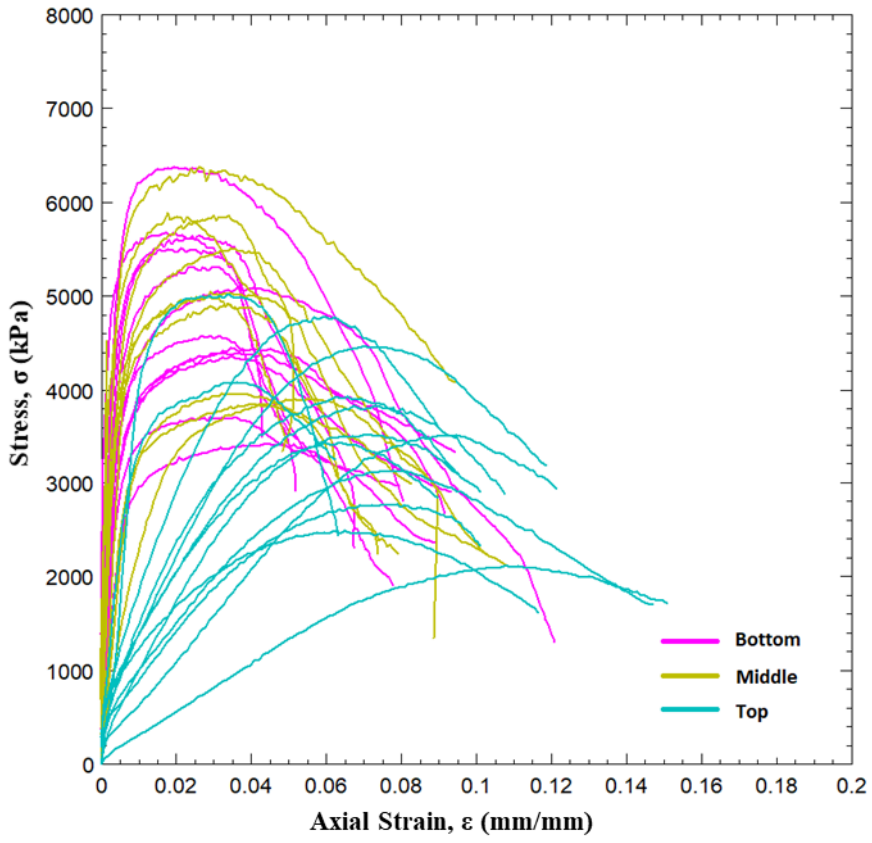

Figure 4.3 Stress-strain curves of cylinders at different layers of the build volume of the 3D printer.

From Table 4.1 Cylinder properties at different layers of build volume of 3D Printer. it is possible to notice that the mass and height of the cylinders increase from the bottom to the top layer. The density is constant for the bottom and middle layers, but smaller at the top layer. The same happens with the UCSs, which are almost the same for the bottom and middle layers, but lower at the top layer. The SPS tends to increase from the bottom to the top layer, while the E decreases from the bottom to top of the build volume. Figure 4.3 demonstrates the significant difference between SPS and E from the bottom and middle layers to the top layer. From the statistical values on Table 4.1 Cylinder properties at different layers of build volume of 3D Printer., mass, height and density did not show large COVs, but UCS, SPS and E did present substantial variation within the same layer and even more when the whole group is analyzed. Figure 4.4 show the variation of the cylinders' properties across the vertical plane (x-z) of the build volume. An analysis of the horizontal plane (x-y) is shown by the contour plots in Figure 4.5. The cylinders closer to the left and back edges were heavier, denser, had higher UCS, higher E, lower SPS and smaller height. The cylinders closer to the right and front edges were lighter, taller, less dense, weaker, less stiff and presented higher SPS. These results may indicate that the printer is compacting the powder more efficiently on regions closer to the right and back edges, and on the bottom and middle layer of its build volume.

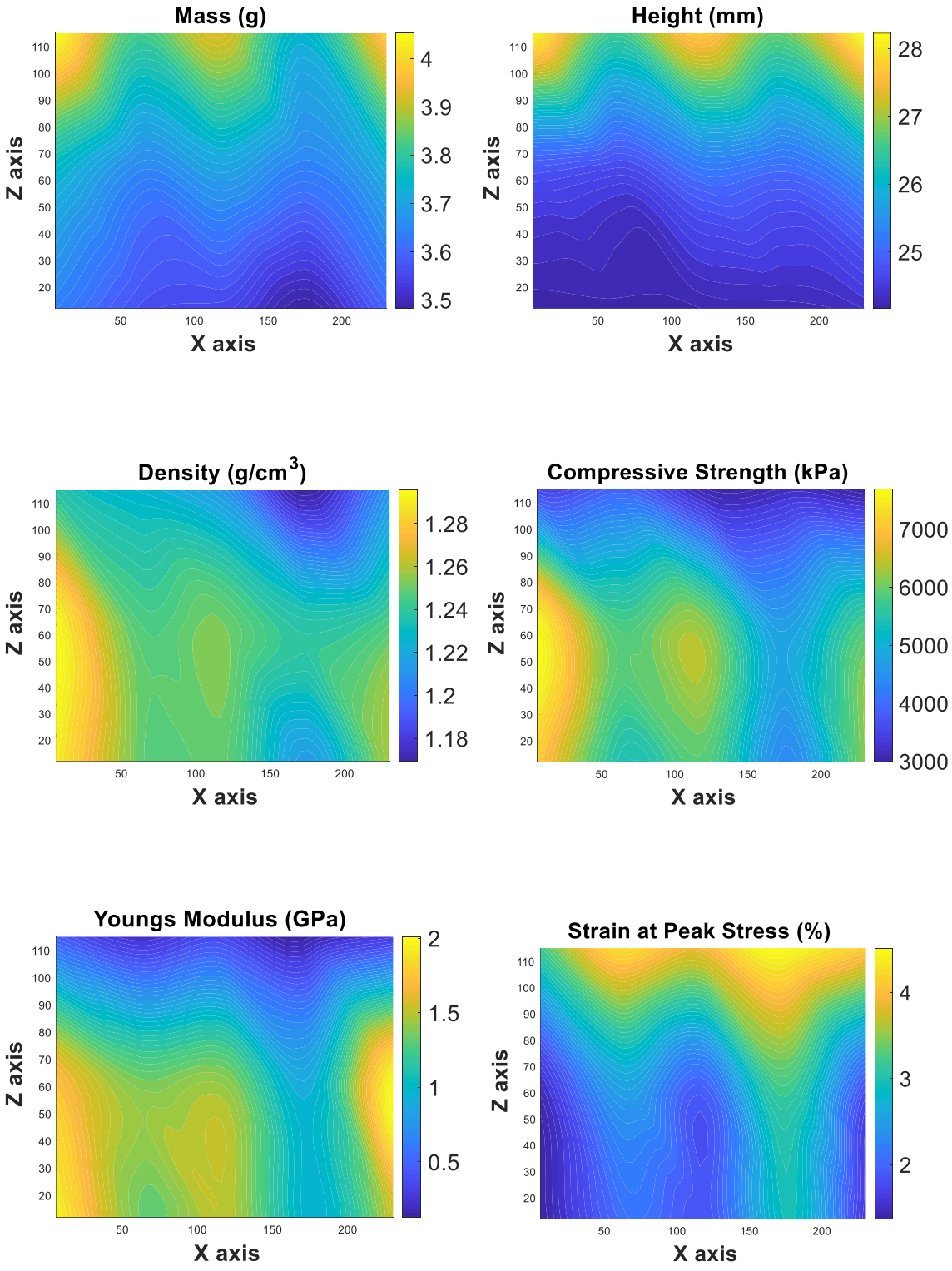

Figure 4.4 Properties variation across x-z plane.

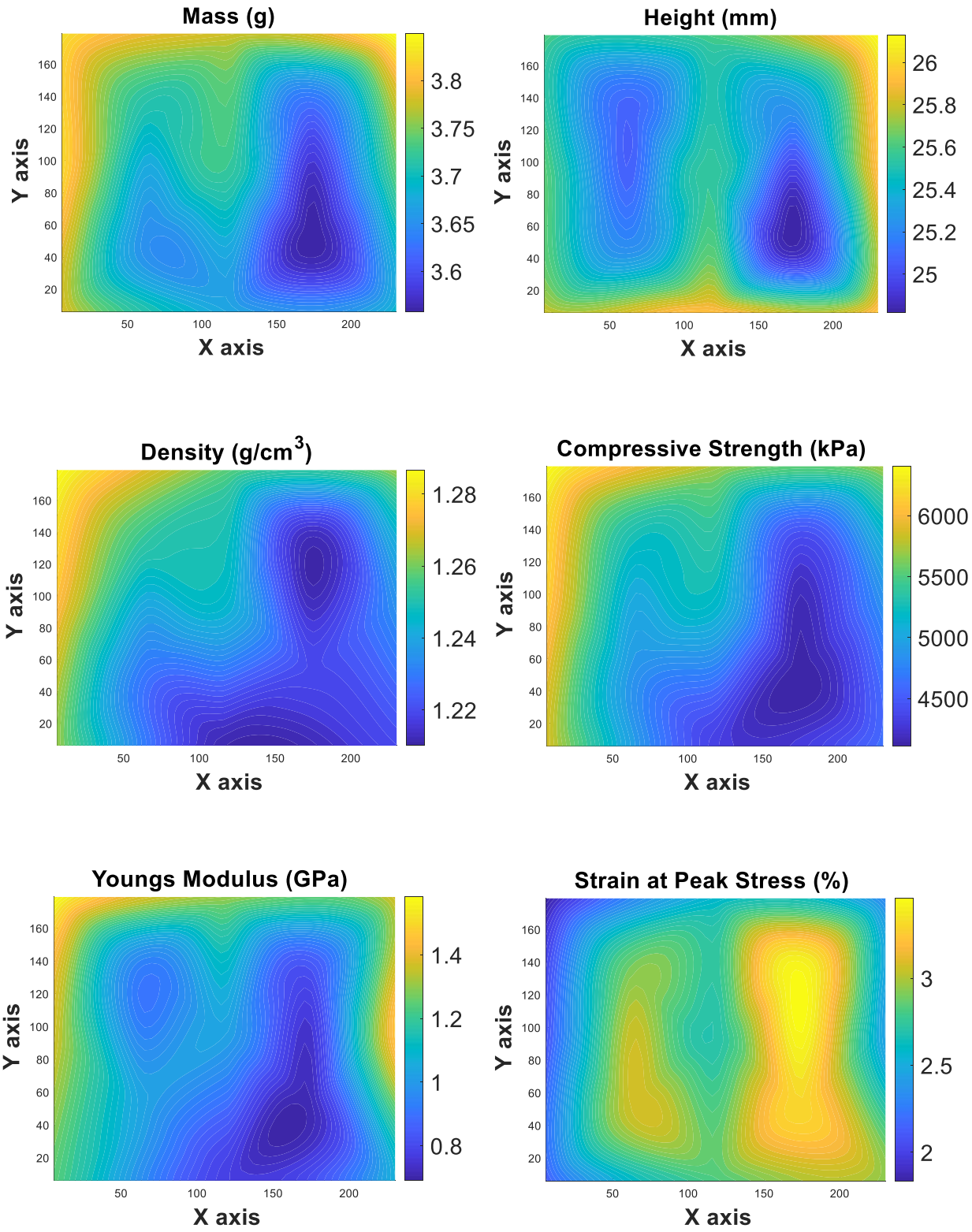

Figure 4.5 Properties variation across x-y plane.

A number of the prototype structures had already been printed and tested by the time this issue was uncovered, and therefore, it was not possible to track their location within the build volume, but all structures printed after this point were tracked and comparisons were made across similar locations from batch to batch.

The moisture conditions of the specimens also influenced the results. In many cases, the specimens were printed and then tested at a later date due to equipment scheduling conflicts. As the number of days between printing and testing increased, the average strength of the cylinders decreased (Figure 4.6). The R-squared value of the linear regression in the graph does not show a strong relationship between time and compressive strength, however, this is likely due to the fact that other factors leading to variability were acting simultaneously. It was determined that an increase in the moisture content of these specimens due to the ambient conditions in the laboratory was weakening the gypsum material. It was also determined that oven drying prior to testing would improve this issue, therefore, all subsequent testing was carried out on oven dried specimens. While it would have been better to keep the days between printing and testing also consistent, this was not easily accomplished because of scheduling. As such, rather than being able to compare the printed structures across batches, it was determined that a more appropriate approach was to consider only results within a single batch.

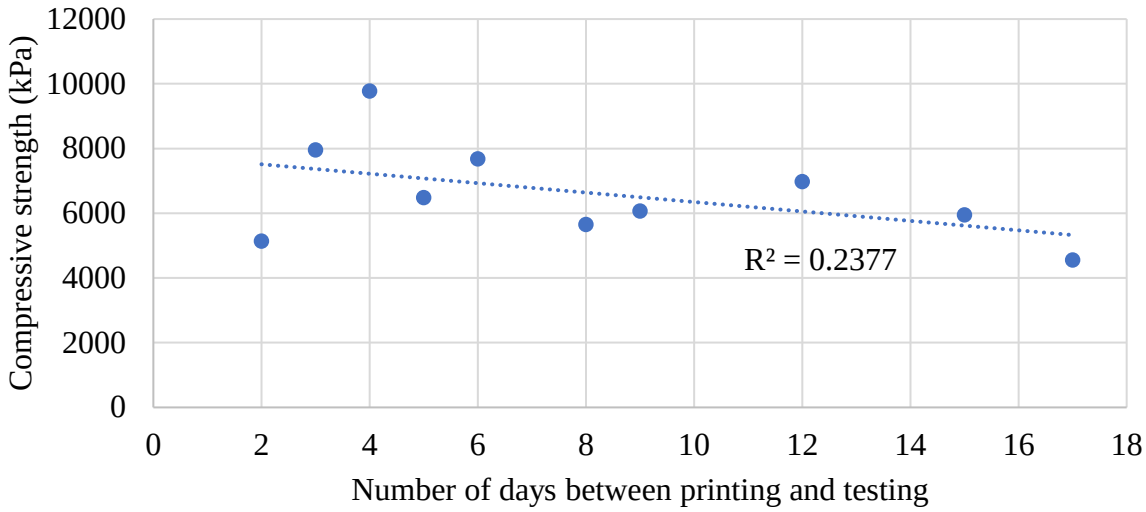

Figure 4.6 Compressive strength variation as a function of the number of days between printing and testing.

4.2 Fracture Modes

The prototypes exhibited different types of shear, bearing, and buckling failure modes when subjected to uniaxial compression. Figure 4.7 shows a schematic to demonstrate the nomenclature used in this study for the different types of failures. Figure 4.8 to Figure 4.13 display examples of the failure types for the 3D printed prototypes. These variations may be related to the moisture content, in the case of the bearing failure, and the size of the cell wall to the thickness of the wall, in the case of the buckling failure. It is also likely that the buckling may represent a localized crushing due to a weakened moist material. The different shear fractures may be explained by how brittle materials fail, which is by the propagation of microcracks, that start with defects (or flaws) until a macroscopic crack failure. The location of these defects varies within the specimen, causing the crack to follow different directions as well.

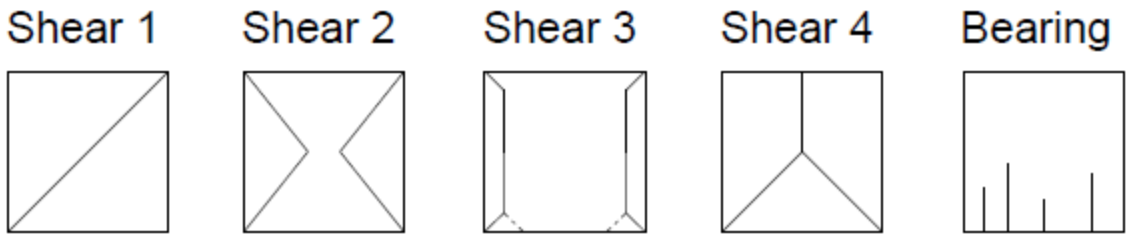

Figure 4.7 Nomenclature for different failure modes.

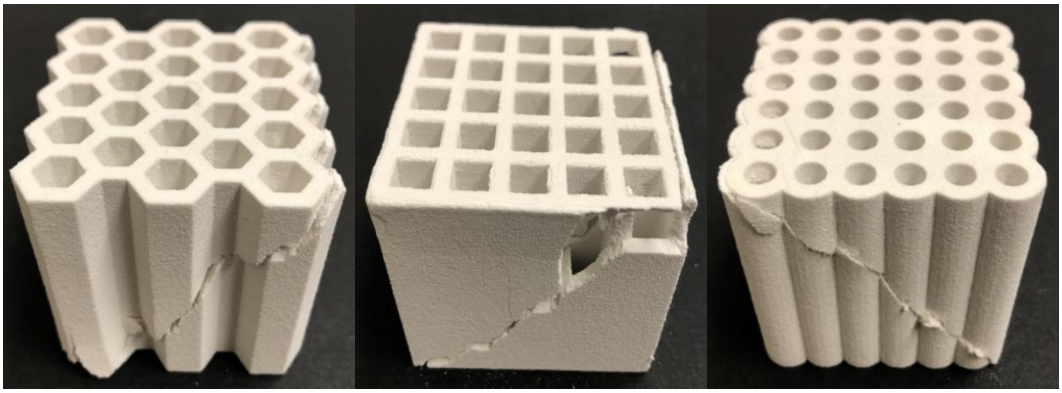

Figure 4.8 Shear 1 failure mode.

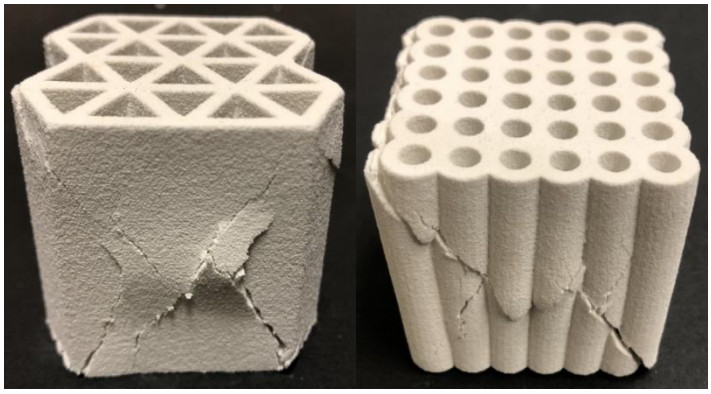

Figure 4.9 Shear 2 failure mode.

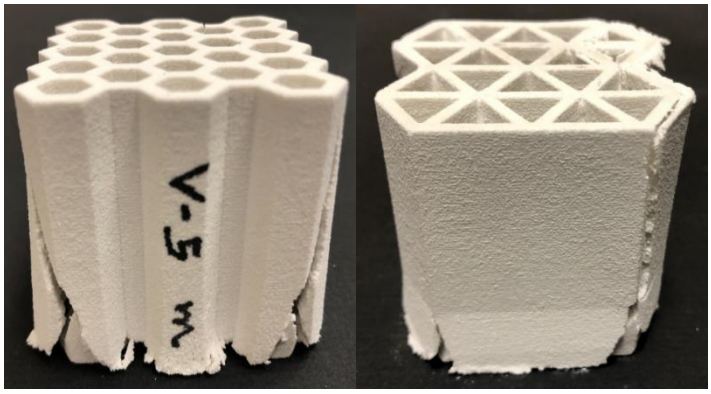

Figure 4.10 Shear 3 failure mode.

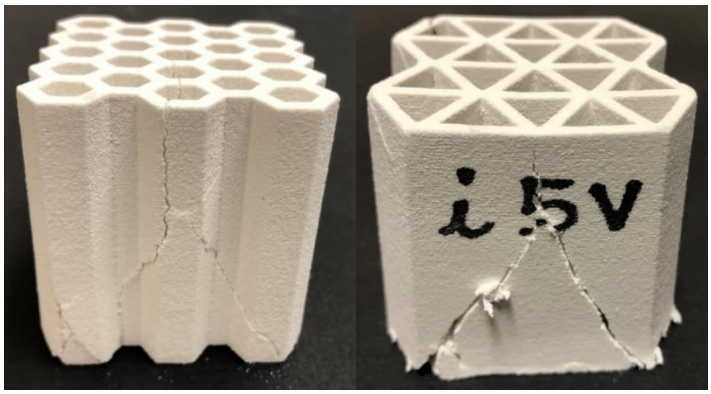

Figure 4.11 Shear 4 failure mode.

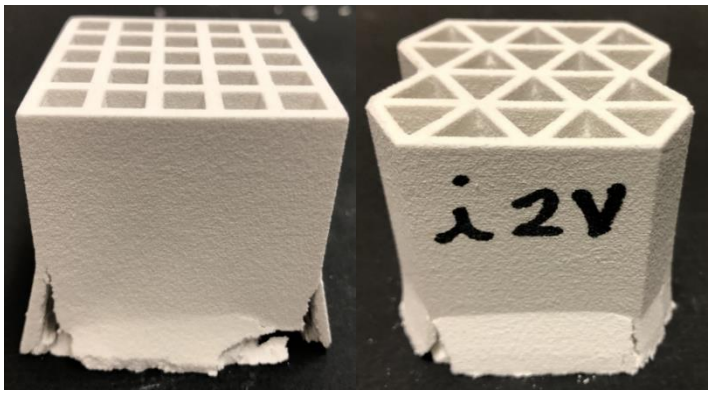

Figure 4.12 Bearing failure mode.

Figure 4.13 Buckling failure mode.

4.3 Batches Results

A total of 15 batches were analyzed for this study. The batches were divided into three segments for analysis:

- Segment 1 is comprised of 2 batches, labeled with alphabetical letters as D and E. Multiple Toucan Beak specimens and cylinders were printed in one single batch for this segment. The bio-inspired specimens included cellular, infilled cellular and solid structures. These specimens were positioned in two layers inside the build chamber (bottom and middle layers), although the exact locations were not tracked. The cylinders were positioned on the left edge wall and bottom layer of the build space. The specimens in these batches were not oven dried before testing.
- Segment 2 is composed of 6 batches (M, N, O, P, S and U), which also included multiple bio-inspired structures (cellular and solid) and cylinders which were printed in one batch. In this segment, the specimens were located just in the bottom layer of the 3D printer's build volume, and their exact locations were recorded. Shapes in this segment include the Honeycomb, Plant Stalk and Horn.

- In segment 3, a total of 7 batches were printed including just one specimen positioned always at the same location in the build volume of the 3D printer. These batches were denominated as TB I, TB II, TB III, TB IV, HC, PS and H, according to the respective prototype design.

4.3.1 Segment 1 – Toucan Beak

4.3.1.1 Cylinders

In this segment, 10 cylinders were tested for each batch. Cylinders from batch D were tested 17 days after being printed and from batch E, 5 days after. The properties determined for cylinders in batches D and E are summarized in Table 4.2. Statistical values including the mean, SD, COV are reported for each, as well as for the entire group.

Table 4.2 Cylinder properties in Segment 1.

		Height (mm)	Density (g/cm^3)	UCS (kPa)	Strain at Peak Stress (%)	Young's Modulus (GPa)
D	**Mean**	24.24	1.27	4556	3.13	1.60
	SD	0.05	0.01	509	0.67	0.76
	COV (%)	0.22	0.97	11.17	21.38	47.66
E	**Mean**	24.25	1.27	3956	3.22	1.48
	SD	0.08	0.01	247	0.71	0.49
	COV (%)	0.34	1.00	6.24	22.02	33.10
Mean		24.25	1.27	4256	3.17	1.54
SD		0.07	0.01	500	0.69	0.64
COV (%)		0.29	0.98	11.74	21.76	41.77

The cylinders in this segment exhibited a height of 24.25 mm, density of 1.27 g/cm^3, UCS in a range of 3956-4556 kPa, SPS between 3.13 and 3.22%, and E from 1.48 to 1.60 GPa. Within the same batch or for both batches, COVs were small for height (0.22 to 0.34%) and density (1%); moderate for UCS (6.2 to 11.7%); and substantial for SPS (21.4 to 22%) and E (33.1 to 47.7%). Figure 4.14 and Figure 4.15 show the stress-strain curves for each batch. Although great variability was observed for the SPS and E, the curves demonstrate similar shapes.

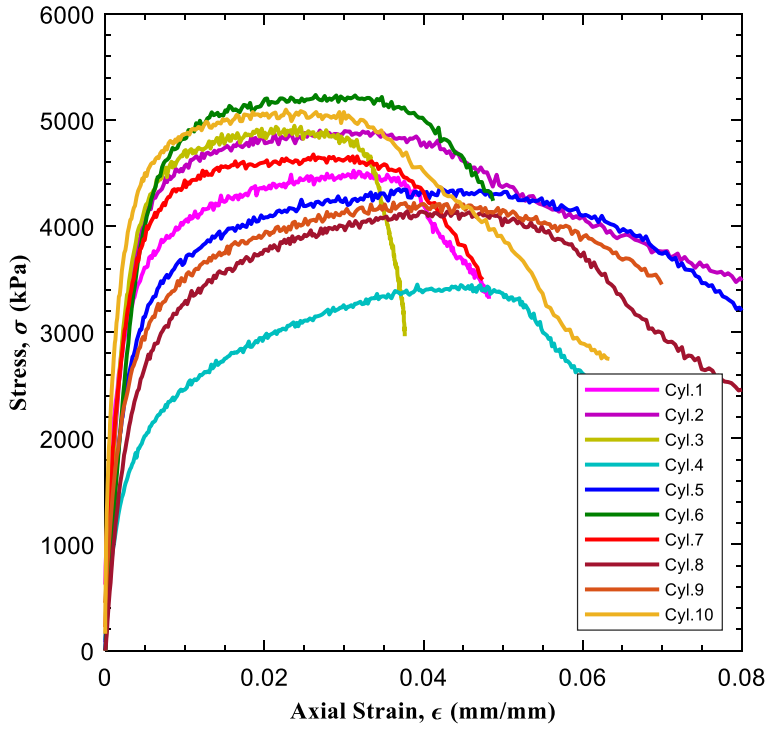

Figure 4.14 Stress-strain curves of cylinders in Batch D.

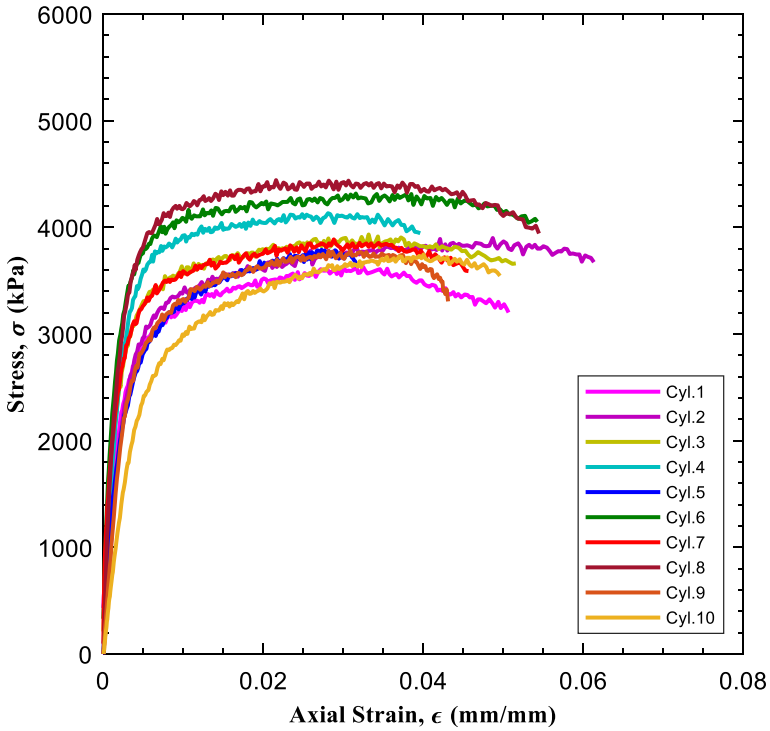

Figure 4.15 Stress-strain curves of cylinders in Batch E.

4.3.1.2 Bio-inspired Structures

4.3.1.2.1 Batch D

Batch D was comprised of the 4 variations of the Toucan Beak in the configuration with voids (i.e., I, II, III and IV). Three replicates of each were printed, obtaining a total of 12 specimens. They were tested 13 days after being printed and were not dried before testing. The properties determined for the bio-inspired specimens are displayed in Table 4.3. The gross density was calculated considering the volume formed by the gross area and the height of the specimen. The material density is related to the volume comprised by the material area of the structure and its height. As mentioned before, relative density is the ratio of the gross density by the material density. The stress-strain curves are presented in Figure 4.16 and Figure 4.17. Cellular I refers to Toucan Beak I, Cellular II to Toucan Beak II, and so forth.

Table 4.3 Toucan Beak properties in Batch D.

	Gross Density (g/cm^3)	**Material Density (g/cm^3)**	**Relative Density**	**Stain at Peak Stress (%)**	**Max. Stress using Gross Area (kPa)**
Toucan Beak I	0.79	1.44	0.55	3.53	2986
Toucan Beak II	0.90	1.42	0.63	3.83	3030
Toucan Beak III	0.87	1.57	0.55	4.00	3198
Toucan Beak IV	0.68	1.46	0.47	2.88	2517

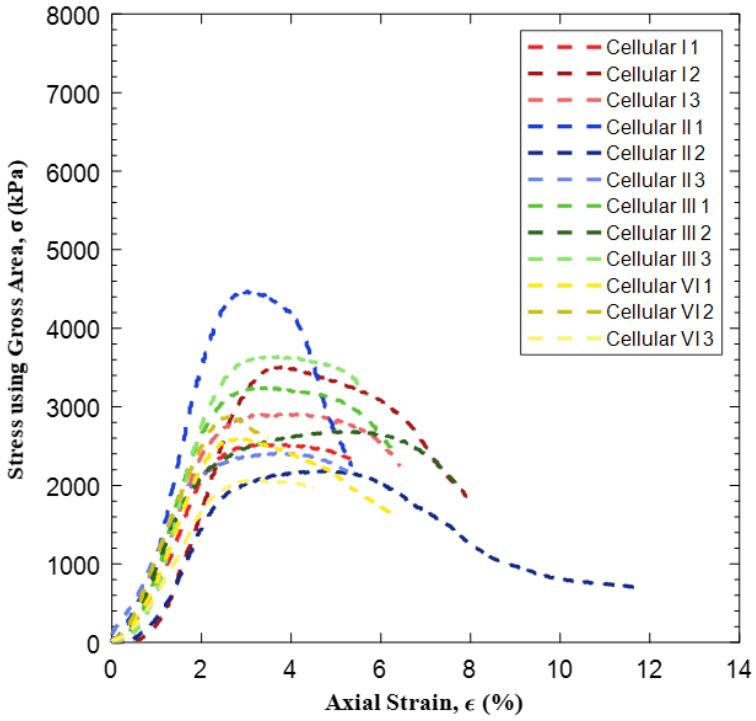

Figure 4.16 Stress-strain curves of cellular structures using gross area in Batch D.

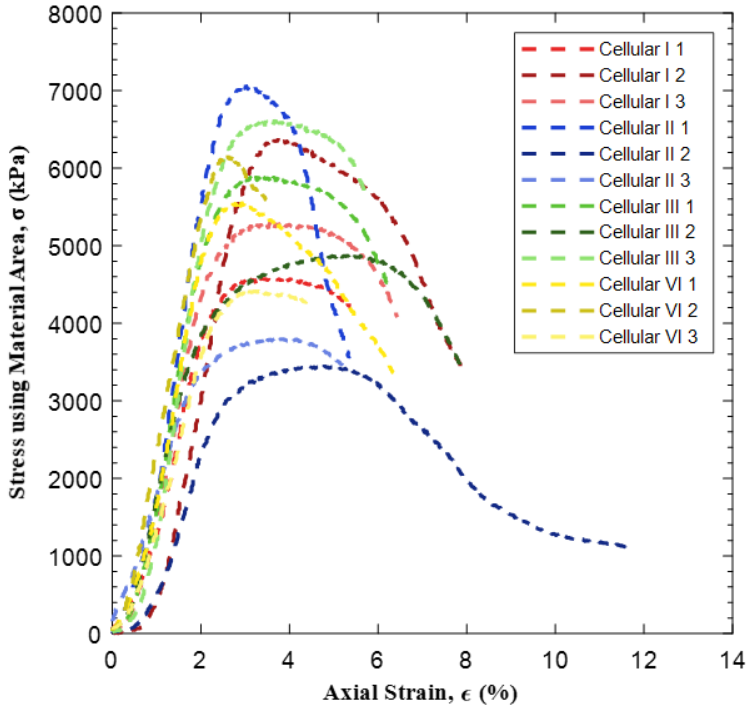

Figure 4.17 Stress-strain curves of cellular structures using material area in Batch D.

4.3.1.2.2 Batch E

Batch E was composed of 4 variations of the Toucan Beak in the 3 different configurations: cellular, infilled cellular and solid structures. Three replicates of each solid structure, two of each cellular structure, and one of each infilled cellular structure were printed, obtaining a total of 24 prototypes. The specimens were not dried before testing. The solid structures were tested after 6 days of being printed, the cellular structures after 7 and 12 days, and the infilled cellular structures after 7 days. Properties for the three different configurations for each type of Toucan Beak are presented in Table 4.4. The stress-strain curves are presented in Figure 4.18, Figure 4.19, and Figure 4.20.

Table 4.4 Toucan Beak properties in Batch E.

		Gross Density (g/cm^3)	Material Density (g/cm^3)	Relative Density	Stain at Peak Stress (%)	Max. Stress using Gross Area (kPa)
Toucan Beak I	**Solid**	1.28	1.28	1	6.16	3212
	Cellular	0.83	1.5	0.55	3.1	3532
	Infilled Cellular	1.22	-	-	3.54	3091
Toucan Beak II	**Solid**	1.3	1.3	1	5.31	2692
	Cellular	0.94	1.49	0.63	2.87	3871
	Infilled Cellular	1.22	-	-	2.95	2854
Toucan Beak III	**Solid**	1.26	1.26	1	6.9	2577
	Cellular	0.89	1.61	0.55	3.37	3070
	Infilled Cellular	1.12	-	-	3.68	2001
Toucan Beak IV	**Solid**	1.27	1.27	1	5.71	3117
	Cellular	0.69	1.47	0.47	3.44	2522
	Infilled Cellular	1.21	-	-	3.54	2763

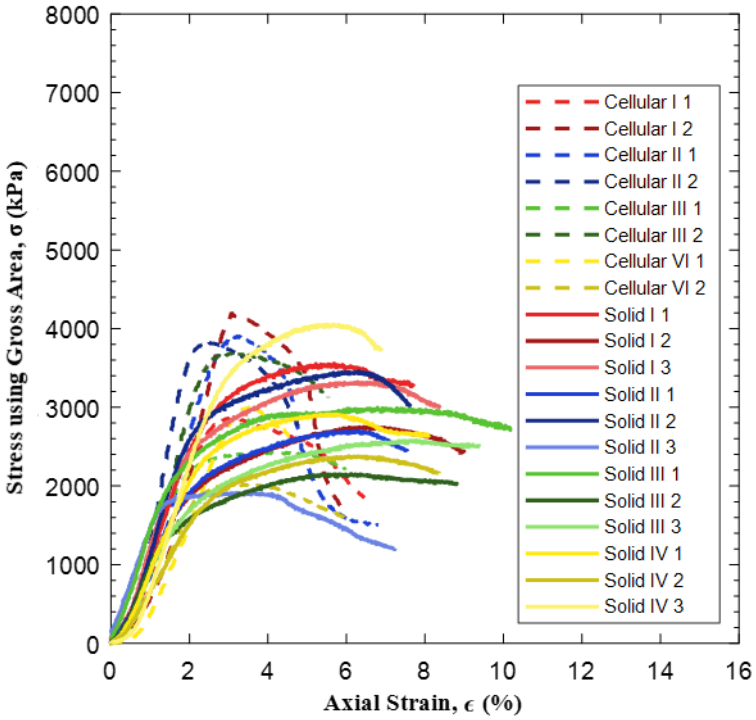

Figure 4.18 Stress-strain curves of solid and cellular structures using gross area in Batch E.

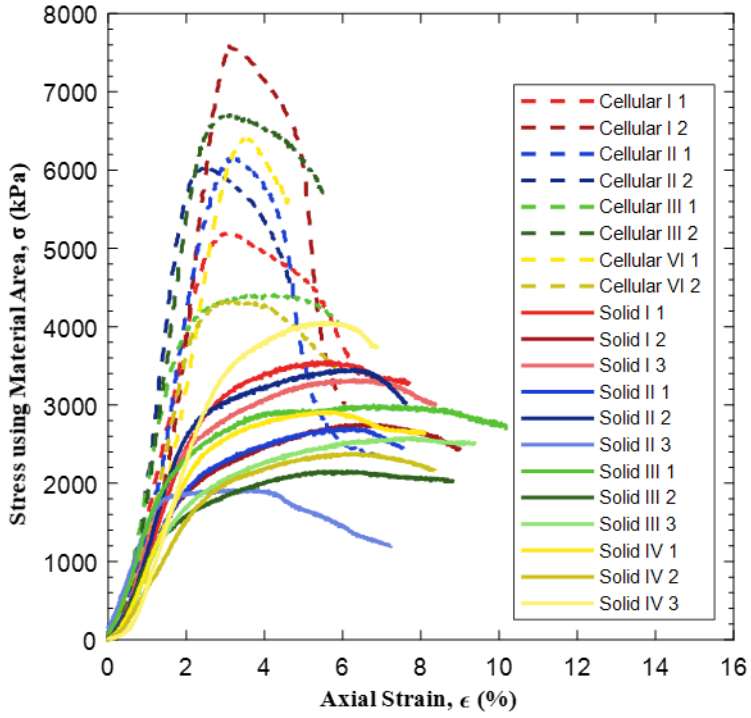

Figure 4.19 Stress-strain curves of solid and cellular structures using material area in Batch E.

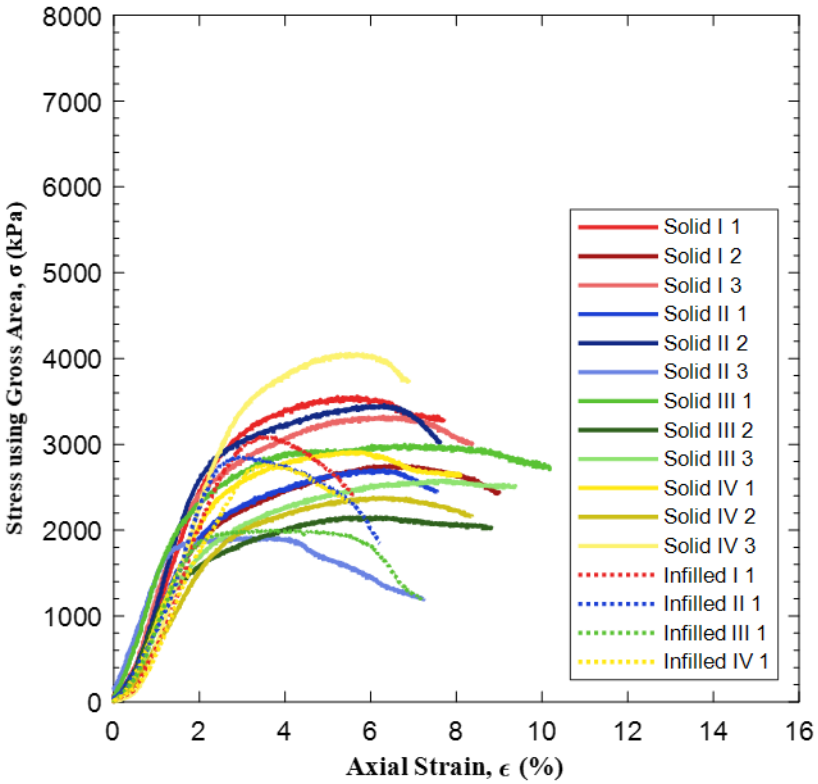

Figure 4.20 Stress-strain curves of solid and infilled cellular structures using gross area in Batch E.

4.3.1.3 Comparison of different Toucan Beak shapes (Batch D and E)

The cellular structures of batches D and E were analyzed together. The means for each shape and statistical values, are reported in Table 4.5 and stress-strain curves for the combined batches are presented in Figure 4.21 and Figure 4.22.

Table 4.5 Toucan Beak properties in Batch D and E.

		Gross Density (g/cm^3)	Material Density (g/cm^3)	Relative Density	Stain at Peak Stress (%)	Max. Stress using Gross Area (kPa)
Toucan Beak I	**Mean**	0.81	1.46	0.55	3.36	3204
	SD	0.03	0.05		0.25	592
	COV (%)	3.18	3.18		7.57	18.48
Toucan Beak II	**Mean**	0.92	1.45	0.63	3.45	3366
	SD	0.03	0.05		0.77	899
	COV (%)	3.26	3.26		22.24	26.72
Toucan Beak III	**Mean**	0.87	1.59	0.55	3.75	3147
	SD	0.02	0.03		0.70	509
	COV (%)	1.89	1.89		18.75	16.16
Toucan Beak IV	**Mean**	0.68	1.46	0.47	3.11	2519
	SD	0.01	0.03		0.32	403
	COV (%)	2.19	2.19		10.32	16.00

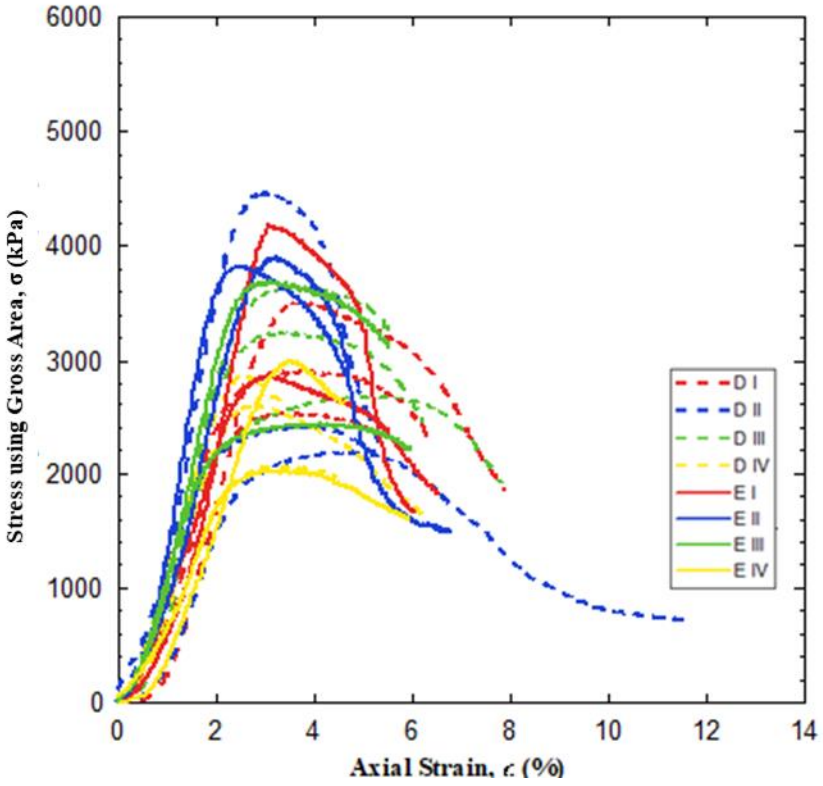

Figure 4.21 Stress-strain curve of cellular structures using gross area in Batch D and E.

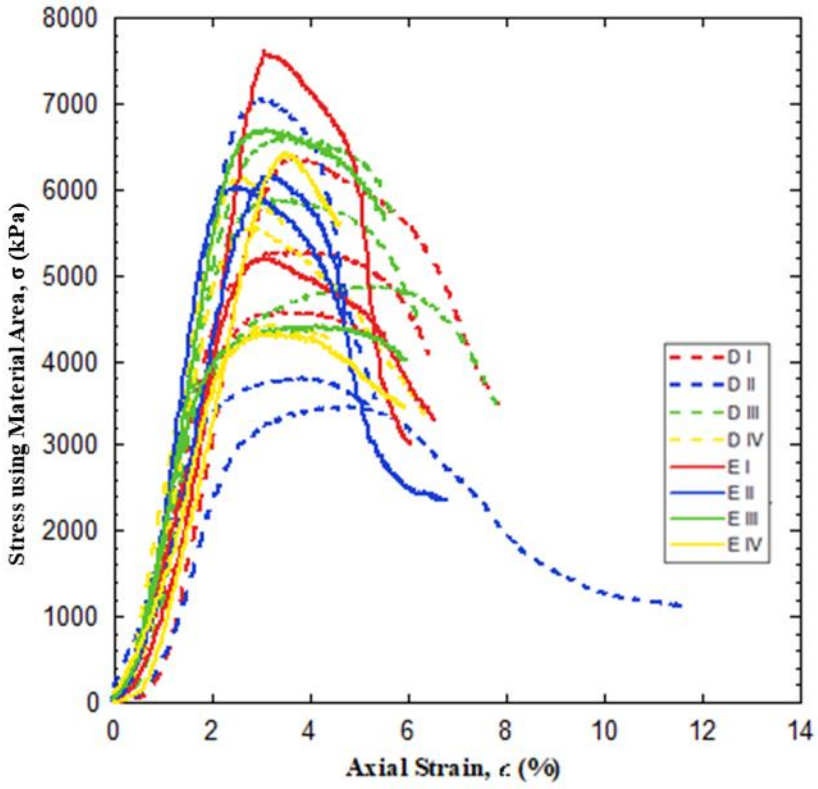

Figure 4.22 Stress-strain curve of cellular structures using material area in Batch D and E.

Considering the gross density of the cellular specimens, Toucan Beak II was the densest (0.92 g/cm^3), followed by Toucan Beak III (0.87 g/cm^3), then Toucan Beak I (0.81 g/cm^3) and Toucan Beak IV (0.68 g/cm^3). It is possible to conclude that the printer uses more binder when the wall is thinner. Toucan Beak I, II and IV have the same wall thickness (≈ 2.41mm) and presented similar material density for the material (1.45 – 1.46 g/cm^3). On the other hand, Toucan beak III has thinner wall thickness (≈1.32 mm), and it had denser walls (1.59 g/cm^3). Analyzing the relative density, Toucan Beak II has the highest (0.63) and Toucan Beak IV the lowest (0.47). Toucan Beak I and III presented the same relative density (0.55).

Toucan Beak II had the highest compressive strength (3366 kPa), followed by the Toucan Beak I (3204 kPa), then Toucan Beak III (3147 kPa), and lastly Toucan Beak IV (2519 kPa). This

order follows the same order as the relative density. The part that reached the peak load with less deformation was the Toucan Beak IV (3.11%), while Toucan Beak III had the highest deformation (3.75%).

It is likely that the Toucan Beak IV specimens had cells that were too large given their wall thickness, because they failed by buckling, with the lowest stresses and could not withstand much deformation before reaching the peak stress. The Toucan Beak III specimens likely had walls that were too thin and could not carry as much load as Toucan Beak I and II before buckling. Toucan Beak III acted more like a solid structure, exhibiting the most deformation before reaching the peak stress.

Table 4.6 Load-to-weight ratio of cellular structures in Batch D and E.

		Weight (g)	Max. Load (N)	Load/Weight ratio (N/g)
Toucan Beak I	**Mean**	78.96	6260	79.27
	SD	2.72	1160	
	COV (%)	3.44	18.54	
Toucan Beak II	**Mean**	78.22	5725	73.19
	SD	2.40	1531	
	COV (%)	3.06	26.73	
Toucan Beak III	**Mean**	85.61	6149	71.83
	SD	1.60	997	
	COV (%)	1.87	16.22	
Toucan Beak IV	**Mean**	67.34	4939	73.34
	SD	1.48	790	
	COV (%)	2.20	15.99	

Analyzing the load-to-weight ratio (Table 4.6), the Toucan Beak I was the most efficient structure (79.27 N/g), and the Toucan Beak III was the worst (71.83 N/g). Based on these analyses, Toucan Beak I and II had the best cellular geometries in terms of load carried, and Toucan Beak I was the most efficient cellular structure, having the highest load-to-weight ratio.

4.3.1.4 Comparison of different configurations: Cellular, Solid, and Infilled Cellular (Batch E)

Properties for the three different configurations for each type of Toucan Beak are presented in Table 4.4. For all shapes based on gross density, the solid structures were the densest (1.26 – 1.30 g/cm^3), and the cellular structures were the least dense (0.69 – 0.94 g/cm^3). The material density was higher for the cellular structures (1.47 – 1.61 g/cm^3) than the solid structures (1.26 – 1.30 g/cm^3), which shows, as explained previously, that the constituent material of these two different configurations were not the same. Also, the solid structures took more deformation before reaching the peak stress (5.31 – 6.90%) and the cellular structures had the least deformation (2.87 – 3.44%). The infilled cellular structures had slightly higher density (1.12 – 1.21 g/cm^3) and SPS compared to the cellular structures (2.95 – 3.68%).

Considering the gross area for Toucan Beak I, the cellular structure had the highest strength (3532 kPa), followed by the solid structure (3212 kPa), and then the infilled cellular structure (3091 kPa). For Toucan Beak II, the cellular structures also exhibited the highest compressive strength (3871 kPa); however, the solid structures were the weakest in this case (2692 kPa), and the infilled cellular structures were intermediary (2854 kPa). For Toucan Beak III, the cellular structures were the strongest (3070 kPa), followed by the solid structures (2577 kPa), and then the infilled cellular structures (2001 kPa). The solid structures exhibited the highest strength for Toucan Beak IV, (3117 kPa), followed by the infilled cellular structures (2763 kPa), and then the cellular structures (2522 kPa). This was the only shape in which the cellular structure was not the strongest and ended up being the weakest structure. This can be explained by the cellular structure of Toucan Beak IV's poor mechanical performance likely due to the large sized cells. The cellular structures appear to have the best mechanical performance, but this was due to the fact that they

were comprised of a stronger material resulting from the higher binder saturation. Therefore, the solid and cellular prototypes were actually 3D printed with different constituent materials and cannot be directly compared. The solid and infilled cellular structures also appear to have similar behaviors, but this is also not a proper comparison because the cellular portion of the infilled structures also had the higher binder saturation. Table 4.7 presents the load-to-weight ratios for each Toucan Beak type. Cellular structures for Toucan Beak I, II and III used 36%, 28% and 30%, respectively, less material than the solid structures. They presented an improvement of load-to-weight ratio over the solid structures of 70%, 99% and 70%, respectively. The cellular structures for Toucan Beak IV did not perform well in terms of load carried; however, they still had a 50% improvement in load-to-weight ratio over the solid structure. For Toucan Beak I, solid and infilled cellular structures had very similar behaviors (49.89 and 49.98 N/g, respectively). For Toucan Beak III and IV, the infilled cellular structures had lower ratios than the solid structures. For Toucan Beak II, the solid structures had the worst performance.

Table 4.7 Load-to-weight ratio of prototypes in Batch E.

		Weight (g)	Max. Load (N)	Load/Weight ratio (N/g)	Improvement (%)
Toucan Beak I	**Solid**	126.3	6302	49.89	70
	Cellular	81.2	6897	84.93	
	Infilled Cellular	121.15	6055	49.98	
Toucan Beak II	**Solid**	111.08	4586	41.28	99
	Cellular	80.16	6588	82.18	
	Infilled Cellular	104.17	4861	46.66	
Toucan Beak III	**Solid**	123.95	5042	40.68	70
	Cellular	86.94	5996	68.96	
	Infilled Cellular	110.04	3916	35.59	
Toucan Beak IV	**Solid**	125.72	6113	48.63	50
	Cellular	67.85	4942	72.84	
	Infilled Cellular	119.49	5404	45.23	

4.3.2 Segment 2 – Honeycomb, Plant Stalk and Horn

4.3.2.1 Cylinders

For the second segment, 10 cylinders were also printed for each batch and tested in the MTS machine to provide a comparison of the material properties across batches. The cylinders were tested at different numbers of days after being printed: 8, 5, 2, 4, 3 and 5, respectively. The properties determined for cylinders in batches M to U are summarized in Table 4.8. Cylinders from batch U were oven dried before testing.

Table 4.8 Cylinders properties in Segment 2.

		Height (mm)	Density (g/cm^3)	UCS (kPa)	Strain at Peak Stress (%)	Young's Modulus (GPa)
M	**Mean**	24.32	1.30	6795	1.77	2.31
	SD	0.11	0.02	761	0.28	1.07
	COV (%)	0.47	1.35	11.2	15.84	46.48
N	**Mean**	24.23	1.30	7639	1.47	1.85
	SD	0.08	0.04	865	0.44	0.48
	COV (%)	0.34	2.85	11.32	29.77	25.78
O	**Mean**	24.42	1.26	7590	1.43	2.34
	SD	0.14	0.03	2239	0.52	1.63
	COV (%)	0.56	2.64	29.5	36.43	69.65
P	**Mean**	24.34	1.29	9205	1.11	3.04
	SD	0.09	0.03	2028	0.24	1.53
	COV (%)	0.38	2.48	22.03	21.65	50.24
S	**Mean**	24.27	1.27	7996	1.67	1.77
	SD	0.08	0.03	1455	0.35	0.43
	COV (%)	0.32	2.02	18.2	20.74	24.16
U	**Mean**	24.33	1.29	6156	2.47	1.55
	SD	0.13	0.03	994	0.96	0.9
	COV (%)	0.53	2.38	16.14	38.64	58.53
Mean		24.32	1.28	7575	1.65	2.13
SD		0.12	0.03	1792	0.45	0.48
COV (%)		0.49	2.69	23.66	40.91	57.47

The material for this segment presented a height of 24.32 mm, a density of 1.28 g/cm^3, UCS in the range of 6156 – 9205 kPa, SPS between 1.11 – 2.47%, and E of 1.55 – 3.04 GPa. For all the specimens in the segment, the COVs were small for height and density (0.5 and 2.7%); however, they were substantial for UCS, SPS and E (23.7, 40.9 and 57.5%).

Considering the cylinders that were not oven dried before testing, the cylinders from batch M, which were tested 8 days after being 3D printed, exhibited lower compressive strength than the cylinders from batches N to S, which were tested 2-5 days after being fabricated. However, the cylinders which were oven dried before the compression tests (batches U) presented lower strength than the mean of the whole group. Within the same batch, height and density were the only properties that did not exhibit large variance. Figure 4.23 to Figure 4.28 show the stress-strain curves for the cylinders in each batch.

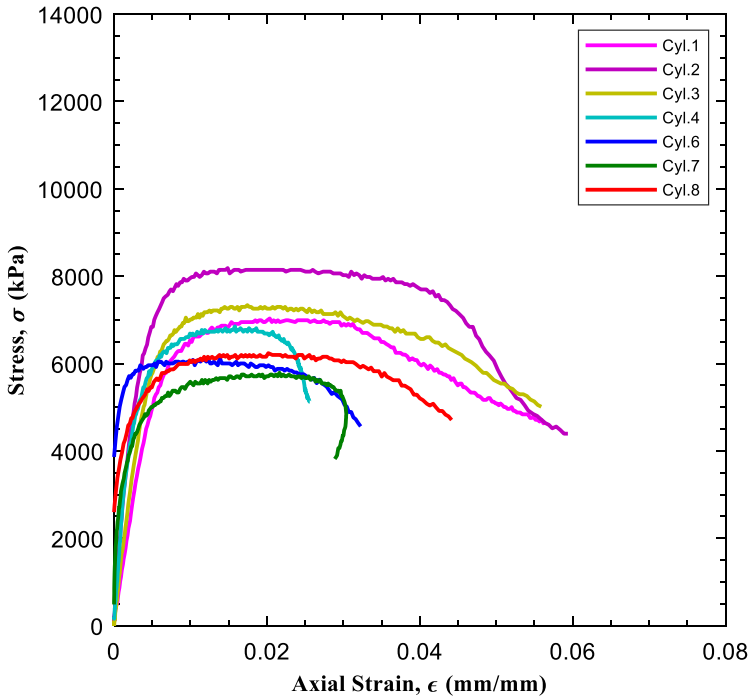

Figure 4.23 Stress-strain curves of cylinders in Batch M.

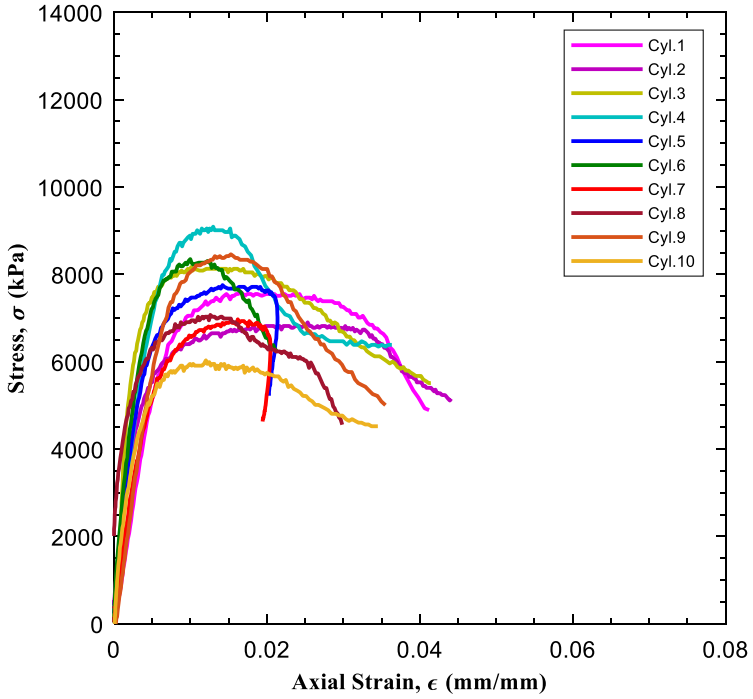

Figure 4.24 Stress-strain curves of cylinders in Batch N.

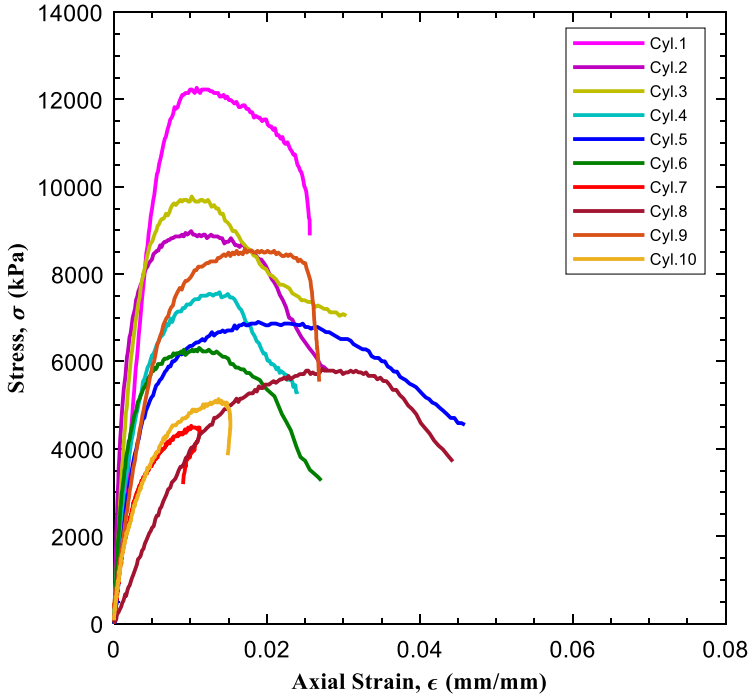

Figure 4.25 Stress-strain curves of cylinders in Batch O.

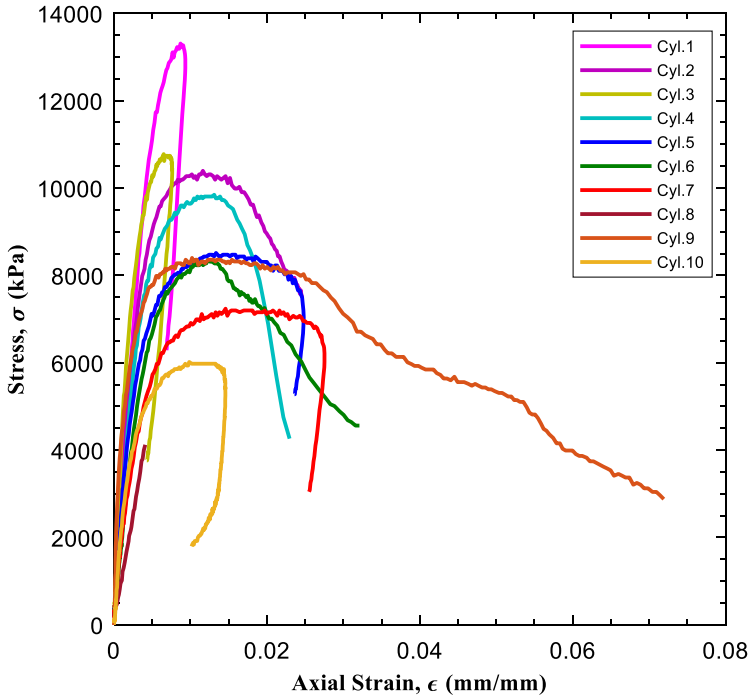

Figure 4.26 Stress-strain curves of cylinders in Batch P.

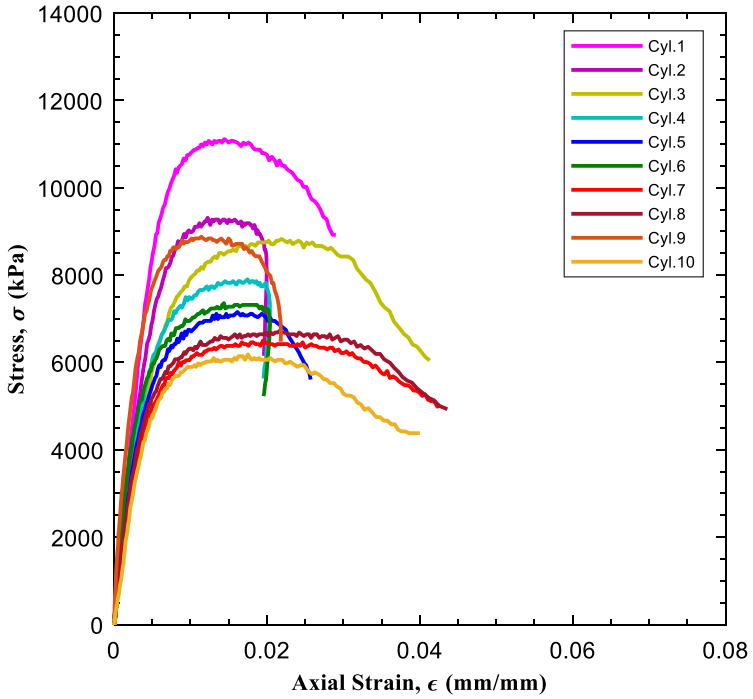

Figure 4.27 Stress-strain curves of cylinders in Batch S.

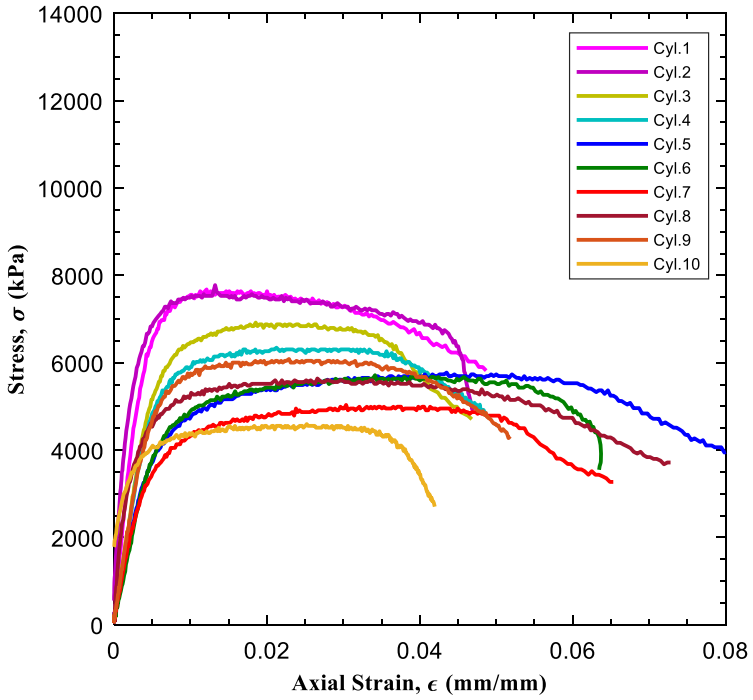

Figure 4.28 Stress-strain curves of cylinders in Batch U.

The stress-strain curves demonstrate a highly variable mechanical behavior during the compression tests for cylinders within the same batch. The groups with more similar performance between cylinders inside the same batch were M, N, S and U. These batches also presented lower COVs for strength.

4.3.2.2 Bio-inspired structures

4.3.2.2.1 Batch M

Batch M was composed of the Honeycomb shape in the cellular and solid configurations. Six replicas of each configuration were printed, obtaining a total of 12 specimens which were organized as shown in Figure 4.29. The specimens in this batch were tested 3 days after being printed and Table 4.9 presents their properties. **Figure *4.30*** Stress-strain curves using gross area of Honeycomb prototypes in Batch M.Figure 4.30 Stress-strain curves using gross area of

Honeycomb prototypes in Batch M. presents the stress-strain curves for all the Honeycomb specimens in Batch M, and Table 4.10 shows the load-to-weight ratios of this batch.

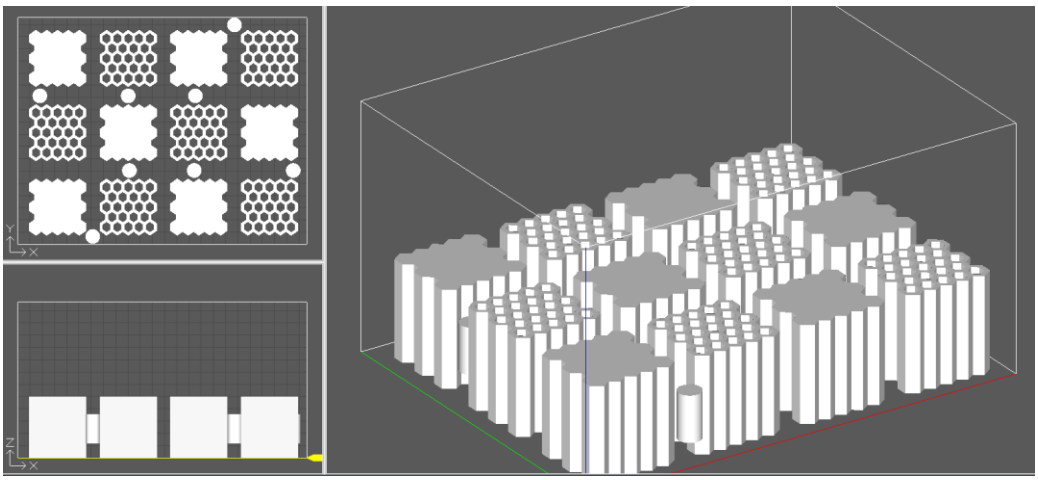

Figure 4.29 Location of prototypes and cylinders in Batch M.

Table 4.9 Honeycomb properties in Batch M.

		Gross Density (g/cm^3)	Material Density (g/cm^3)	Relative Density	Stain at Peak Stress (%)	Max. Stress using Gross Area (kPa)
Solid	**Mean**	1.29	1.29	1.00	3.77	5282
	SD	0.03	0.03		0.21	1022
	COV (%)	1.95	1.95		5.54	19.35
Cellular	**Mean**	0.77	1.45	0.53	4.03	6390
	SD	0.02	0.04		0.31	817
	COV (%)	2.76	2.76		7.72	12.79

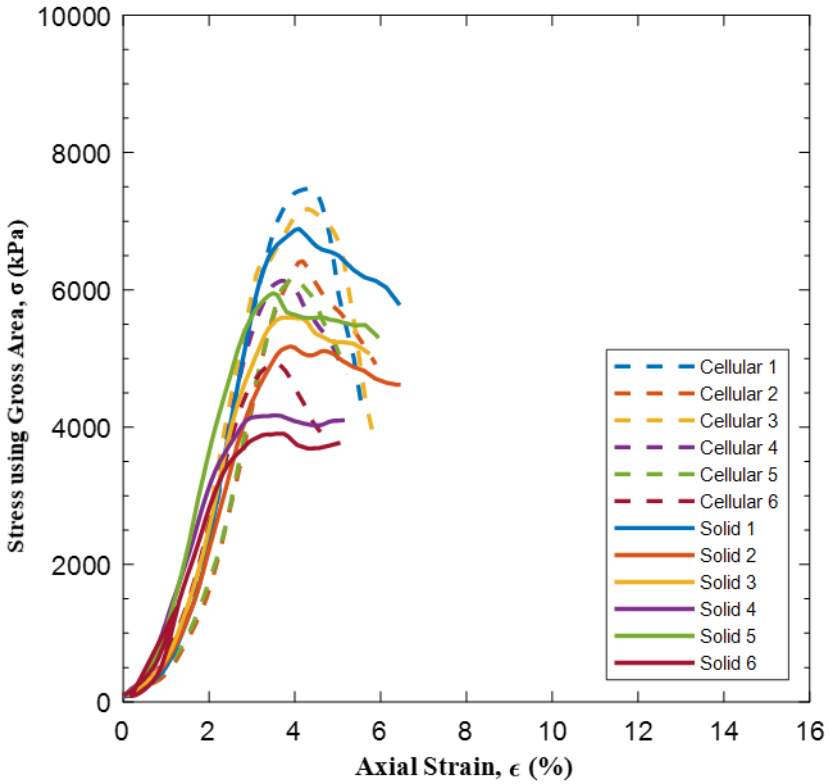

Figure 4.30 Stress-strain curves using gross area of Honeycomb prototypes in Batch M.

The cellular structures withstood higher stresses than the solid structures (around 21% more), considering the same gross area, but again this is due to the fact that the cellular structures had a higher material density than the solid structures. The cellular structures also reached the peak stress at higher strains than solid structures and the cellular structures do not present residual strengths like the solid structures do. The cellular structure results in a much more brittle and catastrophic failure. Note that because gross area is considered here, the stress-strain curve and resulting peak stress values are similar to the relationship observed for force and displacement. The cellular structures exhibited both (Figure 4.31 and Figure 4.32) and the solid structures resulted in more of the Shear 2 and 3 fracture types (Figure 4.33 and Figure 4.34).

Figure 4.31 Shear 3 failure mode of Honeycomb cellular structures (Batch M).

Figure 4.32 Shear 4 failure mode of Honeycomb cellular structures (Batch M).

Figure 4.33 Shear 2 failure mode of Honeycomb solid structures (Batch M).

Figure 4.34 Shear 3 failure mode of Honeycomb solid structures (Batch M).

Considering the load-to-weight ratios, the cellular structures showed an improvement of 104% over the solid structures (Table 4.10). This can also be seen from a plot of stress-strain where the stress is calculated using the material area (Figure 4.35).

Table 4.10 Load-to-weight ratio of Honeycomb prototypes in Batch M.

		Weight (g)	Max. Load (N)	Load/Weight ratio (N/g)	Improvement (%)
Solid	**Mean**	125.60	10198	81.19	104
	SD	2.37	1971		
	COV (%)	1.89	19.33		
Cellular	**Mean**	74.60	12357	165.64	
	SD	1.60	1541		
	COV (%)	2.14	12.47		

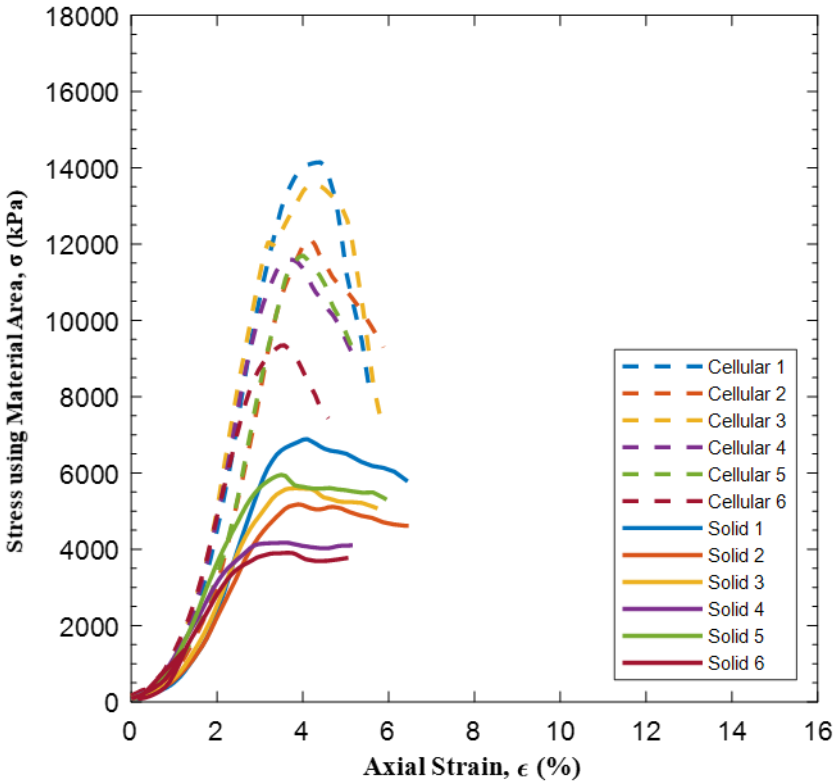

Figure 4.35 Stress-strain curves using material area of Honeycomb prototypes in Batch M.

4.3.2.2.2 Batch N

Batch N had the same composition as Batch M, except for adding two more cylinders as shown in Figure 4.36. Parts were tested 7 days after being printed and Table 4.11 presents the properties obtained. Figure 4.37 displays the stress-strain curves for the prototypes in Batch N. Table 4.12 presents the load-to-weight ratios.

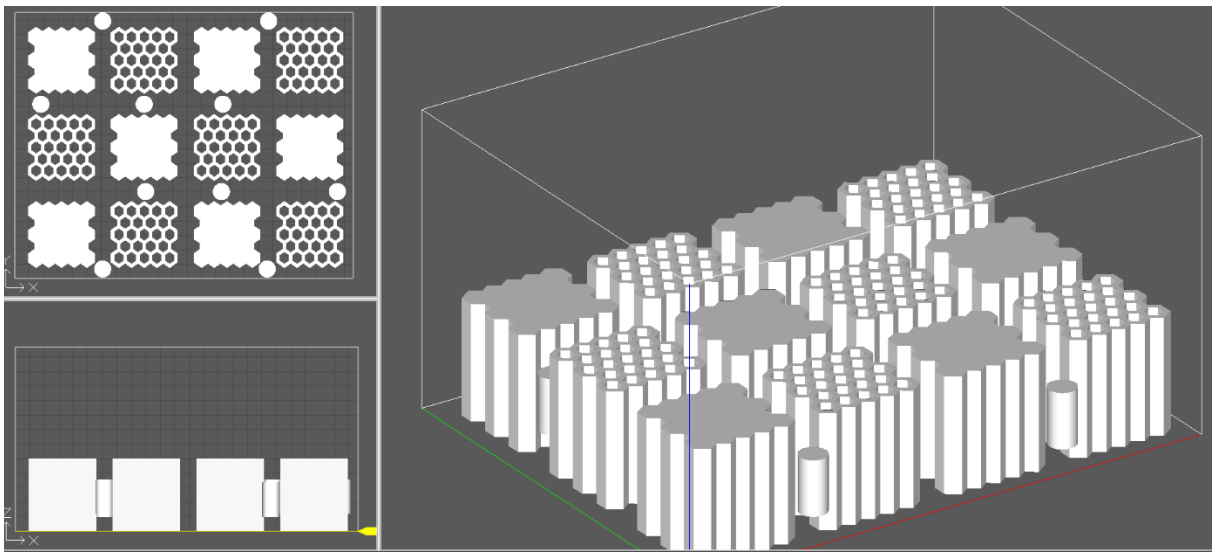

Figure 4.36 Location of prototypes and cylinders in Batch N.

Table 4.11 Honeycomb properties in Batch N.

		Gross Density (g/cm^3)	Material Density (g/cm^3)	Relative Density	Stain at Peak Stress (%)	Max. Stress using Gross Area (kPa)
Solid	**Mean**	1.31	1.31	1.00	4.13	6592
	SD	0.03	0.03		0.54	1292
	COV (%)	2.47	2.47		13.01	19.61
Cellular	**Mean**	0.79	1.49	0.53	3.26	6724
	SD	0.02	0.03		0.32	1010
	COV (%)	2.34	2.34		9.69	15.03

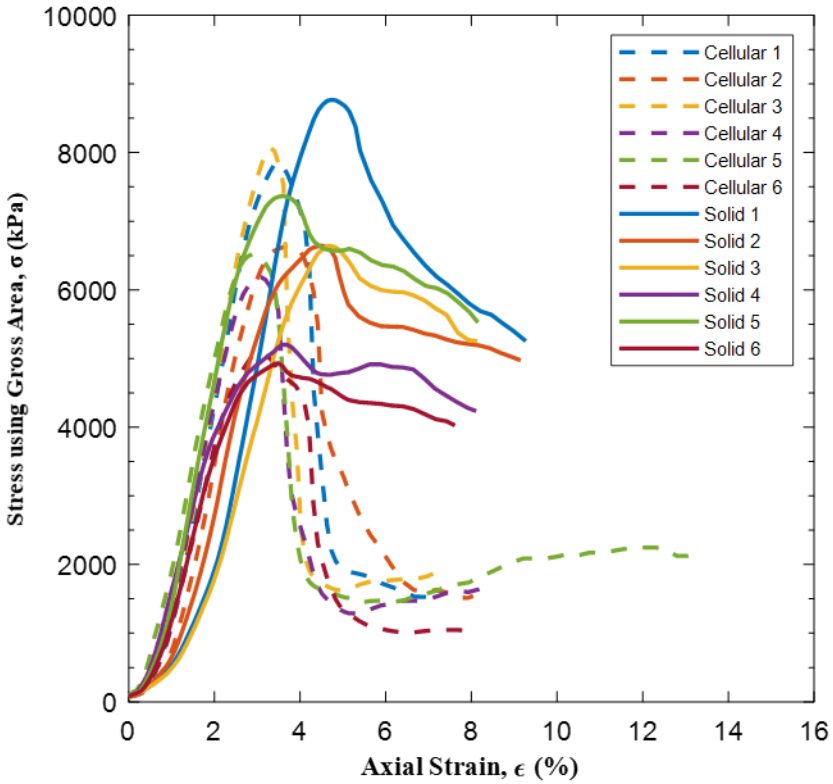

Figure 4.37 Stress-strain curves using gross area of Honeycomb prototypes in Batch N.

Similar to previous batches, the solid structures present a residual strength not shown by the cellular structures. However, it is possible from these curves to see that the cellular structures start carrying more load again around 2000 kPa after the drastic stress drop. This is assumed to be the densification that occurs with cellular solids as proposed by Gibson and Ashby (1997) (Figure 2.37). The cellular and solid structures both showed Shear 1 type failure in this batch, as presented in Figure 4.38 and Figure 4.39. The cellular structures exhibit load-to-weight ratios that are much higher than solid structures, showing an improvement of 70% (Table 4.12 and Figure 4.40).

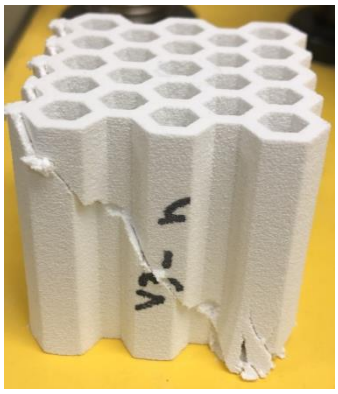

Figure 4.38 Shear 1 failure mode of Honeycomb cellular structures (Batch N).

Figure 4.39 Shear 1 failure mode of Honeycomb solid parts (Batch N).

Table 4.12 Load-to-weight ratio of Honeycomb in Batch N.

		Weight (g)	Max. Load (N)	Load/Weight ratio (N/g)	Improvement (%)
Solid	**Mean**	126.75	12707	100.25	70
	SD	2.91	2489		
	COV (%)	2.30	19.59		
Cellular	**Mean**	76.01	12948	170.35	
	SD	1.65	1950		
	COV (%)	2.17	15.06		

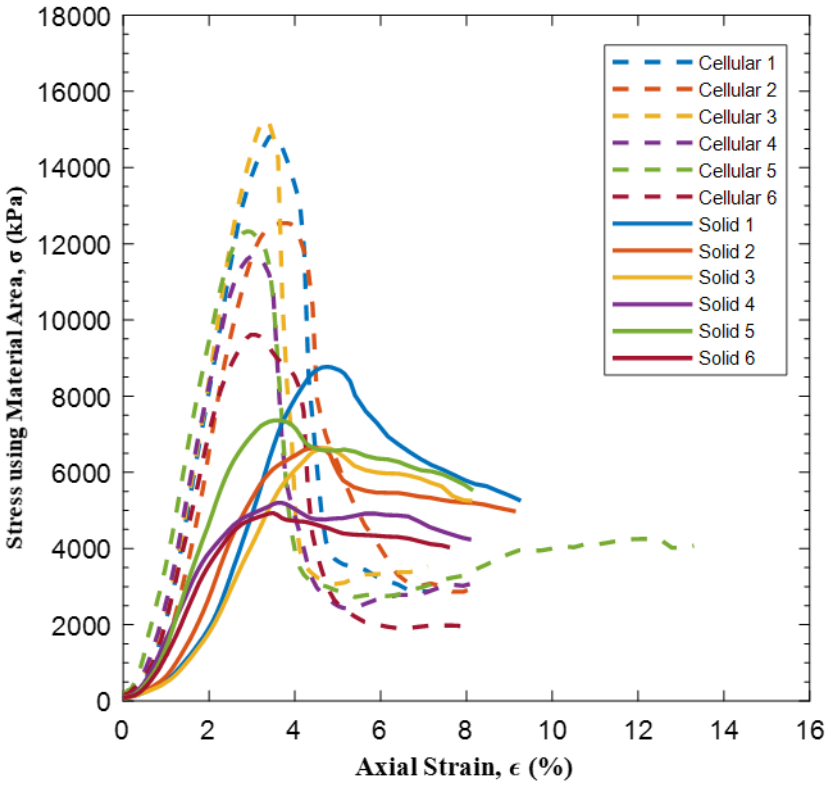

Figure 4.40 Stress-strain curves using material area of Honeycomb prototypes in Batch N.

4.3.2.2.3 Batch O

Batch O was composed of the Plant Stalk shape in the cellular and solid configurations. Six replicates of each configuration were printed, giving a total of 12 specimens which were located in the bottom layer of the build volume (Figure 4.41). The specimens were tested 4 days after being printed. Table 4.13 present their properties, Figure 4.42 presents the stress-strain curves, and Table 4.14 shows the load-to-weight ratios of this batch.

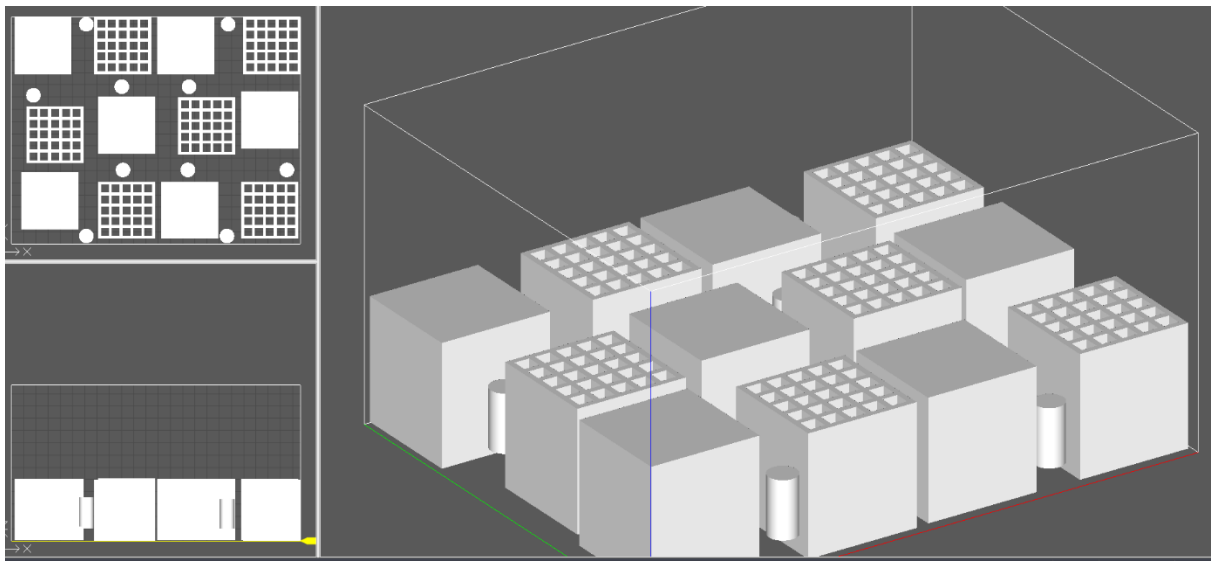

Figure 4.41 Location of prototypes and cylinders in Batch O and P.

Table 4.13 Plant Stalk properties in Batch O.

		Gross Density (g/cm^3)	Material Density (g/cm^3)	Relative Density	Stain at Peak Stress (%)	Max. Stress using Gross Area (kPa)
Solid	**Mean**	1.29	1.29	1.00	4.57	5558
	SD	0.03	0.03		0.79	757
	COV (%)	2.11	2.11		17.30	13.61
Cellular	**Mean**	0.75	1.43	0.52	3.89	7091
	SD	0.02	0.03		0.21	1146
	COV (%)	2.22	2.22		5.46	16.16

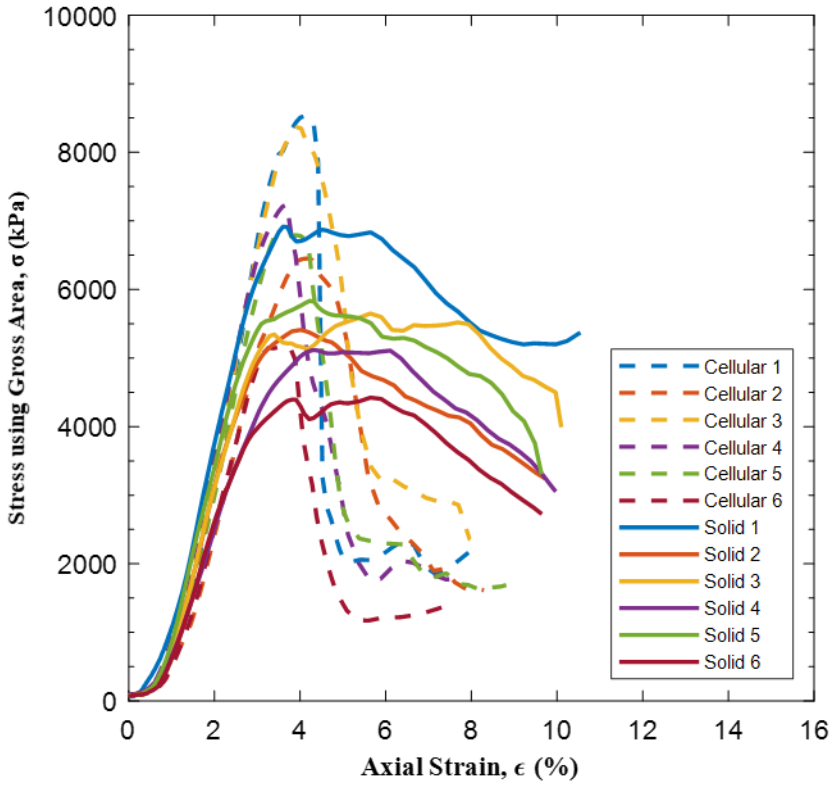

Figure 4.42 Stress-strain curves using gross area of Plant Stalk prototypes in Batch O.

Similar to previous batches, the solid structures showed higher deformation at the peak stress compared to the cellular structures. The cellular structures presented the Shear 1 mode of failure (Figure 4.43) and the solid structures exhibited the Shear 1 and 2 modes (Figure 4.43 and Figure 4.44). The cellular structures with the Plant Stalk shape in this batch exhibited a load-to-weight ratio improvement of 120% (Table 4.14 and Figure 4.46).

Figure 4.43 Shear 1 failure mode of Plant Stalk cellular structure (Batch O).

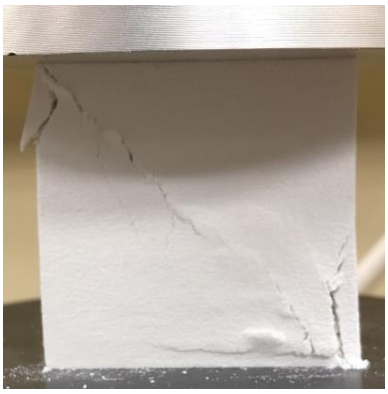

Figure 4.44 Shear 1 failure mode of Plant Stalk solid structure (Batch O).

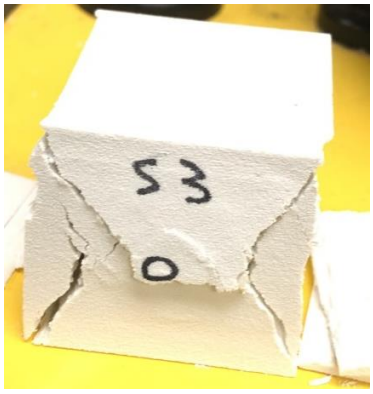

Figure 4.45 Shear 2 failure mode of Plant Stalk solid structure (Batch O).

Table 4.14 Load-to-weight ratio of Plant Stalk in Batch O.

		Weight (g)	Max. Load (N)	Load/Weight ratio (N/g)	Improvement (%)
Solid	**Mean**	143.40	12335	86.02	120
	SD	2.85	1674		
	COV (%)	1.99	13.57		
Cellular	**Mean**	83.38	15745	188.84	
	SD	1.59	2542		
	COV (%)	1.91	16.14		

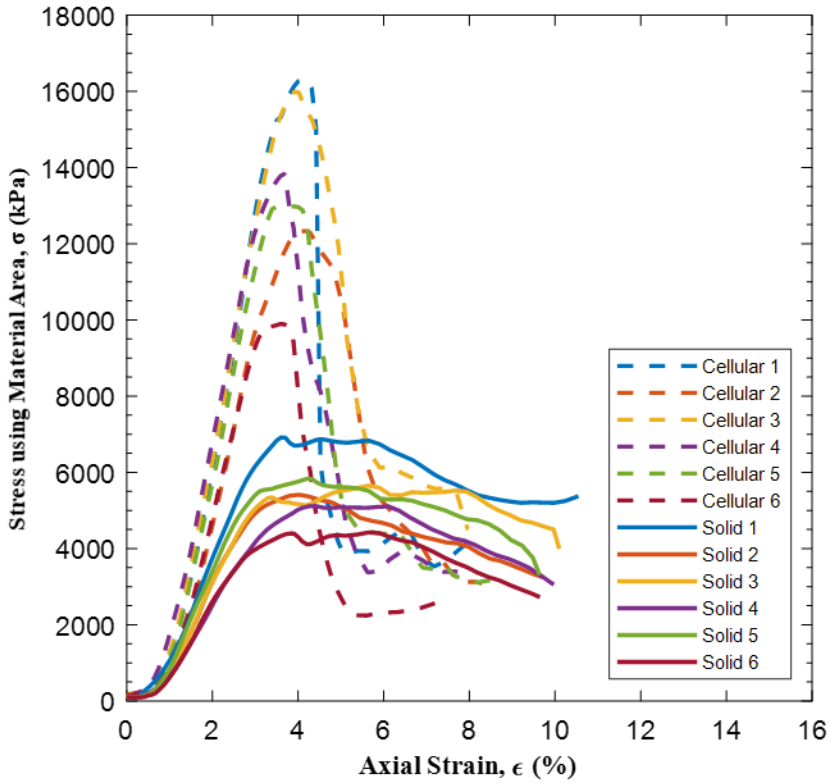

Figure 4.46 Stress-strain curves using gross area of Plant Stalk prototypes in Batch O.

4.3.2.2.4 Batch P

Batch P had the same composition of Batch O. The cellular structures were tested 15 days after being printed and the solid structures within 13 days of being printed. Table 4.15 presents the

properties for them. Figure 4.47 presents the stress-strain curves for all the specimens in Batch P. Table 4.16 shows the load-to-weight ratios of this batch.

Table 4.15 Plant Stalk properties in Batch P.

		Gross Density (g/cm^3)	Material Density (g/cm^3)	Relative Density	Stain at Peak Stress (%)	Max. Stress using Gross Area (kPa)
Solid	**Mean**	1.29	1.29	1.00	6.52	3749
	SD	0.03	0.03		0.60	555
	COV (%)	2.21	2.21		9.20	14.81
Cellular	**Mean**	0.76	1.45	0.52	3.30	5248
	SD	0.02	0.03		0.25	750
	COV (%)	2.00	2.00		7.66	14.28

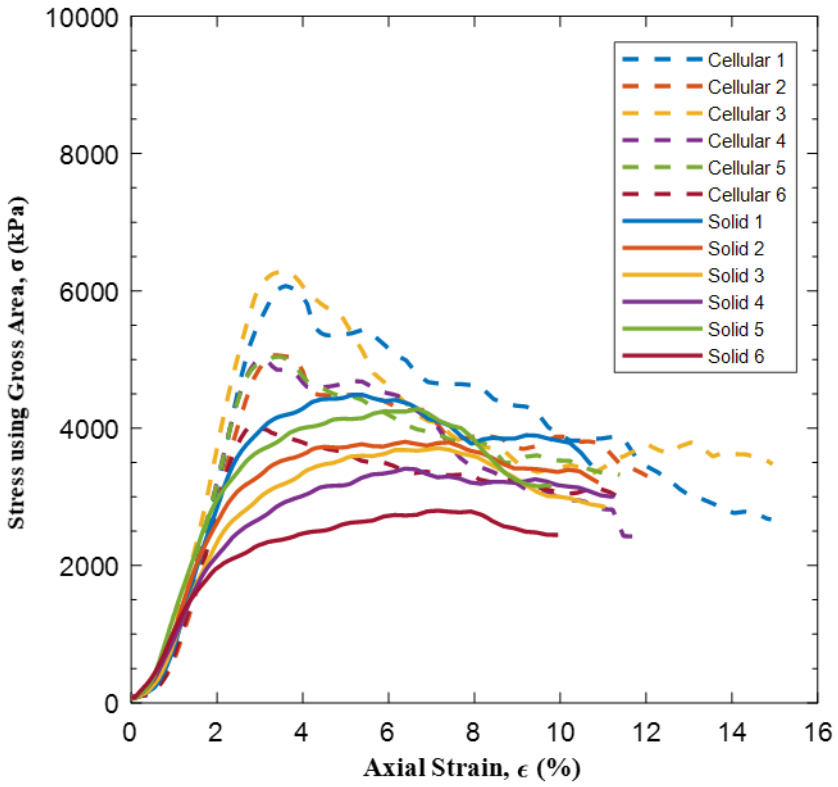

Figure 4.47 Stress-strain curves using gross area of Plant Stalk prototypes in Batch P.

The specimens were weaker in this batch than in Batch O, which could be related to the quantity of days between testing and printing. The cellular structures had a different behavior in

this batch, likely due to the additional moisture absorbed. They presented a residual strength and had bearing failures, as shown in Figure 4.48. The solid structures exhibited the Shear 2 failure mode (Figure 4.49). The solids structures had higher strain at the peak stress compared to the cellular structures. The cellular structures exhibit an improvement of 138% for the load-to-weight ratio over the solid structures in this batch (Table 4.16 and Figure 4.40).

Figure 4.48 Bearing failure mode of Plant Stalk cellular structures (Batch P).

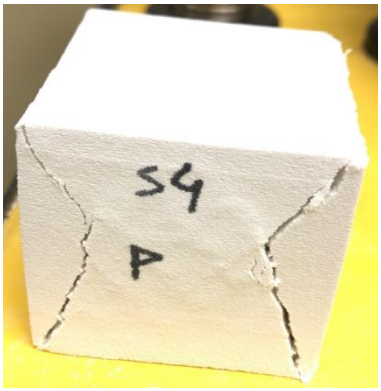

Figure 4.49 Shear 2 failure mode of Plant Stalk solid structures (Batch P).

Table 4.16 Load-to-weight ratio of Plant Stalk in Batch P.

		Weight (g)	Max. Load (N)	Load/Weight ratio (N/g)	Improvement (%)
Solid	**Mean**	142.81	8296	58.09	138
	SD	3.07	1227		
	COV (%)	2.15	14.79		
Cellular	**Mean**	84.03	11621	138.30	
	SD	1.45	1658		
	COV (%)	1.73	14.26		

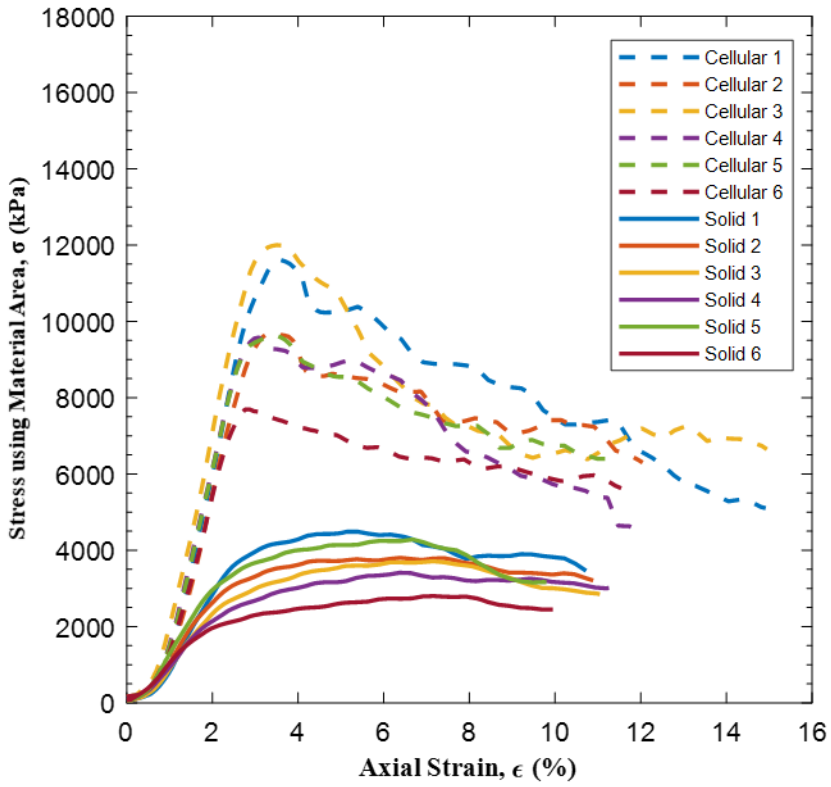

Figure 4.50 Stress-strain curves using material area of Plant Stalk prototypes in Batch P.

4.3.2.2.5 Batch S

Batch S was composed of the Horn shape in the cellular and solid configurations. Six replicates of each configuration were printed, resulting in a total of 12 specimens which were located in the bottom layer of the build volume, as shown in Figure 4.51. Some of the specimens

were dried before testing and some were not to determine whether this would be an effective method to overcome the issue of moisture in the specimens. The specimens were tested 16 and 17 days after being printed and Table 4.17 presents their properties. Figure 4.52 presents the stress-strain curves for all the specimens in Batch S. Load-to-weight ratios are displayed in Table 4.18.

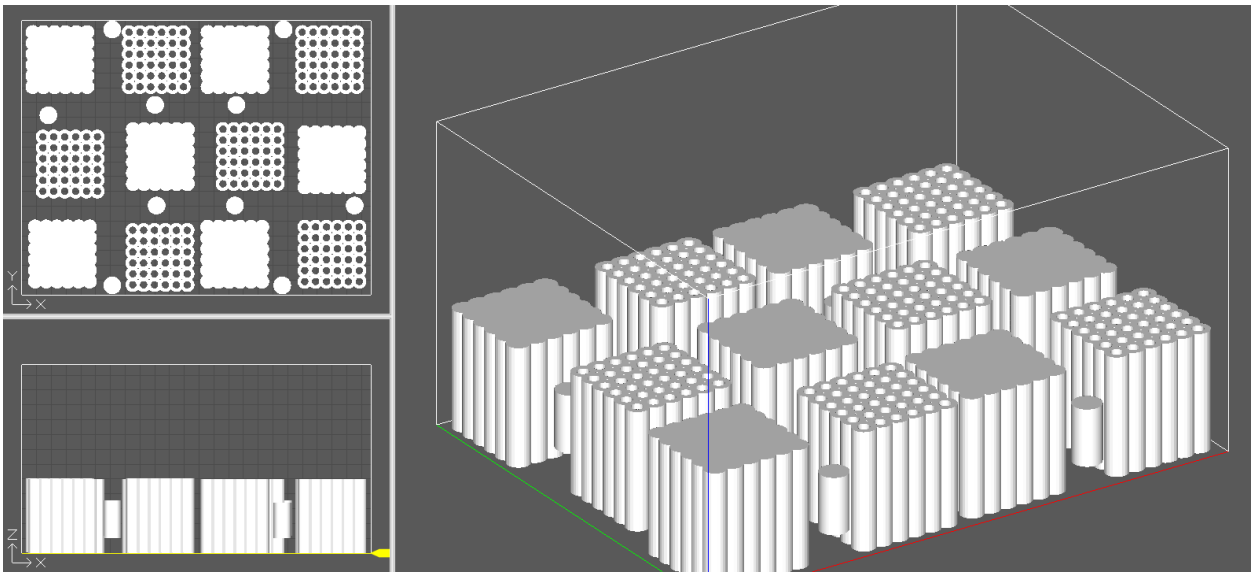

Figure 4.51 Location of prototypes and cylinders in Batch S and U.

Table 4.17 Horn properties in Batch S.

		Gross Density (g/cm^3)	Material Density (g/cm^3)	Relative Density	Stain at Peak Stress (%)	Max. Stress using Gross Area(kPa)
Solid	**Mean**	1.29	1.29	1.00	6.60	4545
	SD	0.03	0.03		1.63	1311
	COV (%)	2.05	2.05		24.77	28.84
Cellular	**Mean**	0.95	1.43	0.66	3.96	6614
	SD	0.02	0.02		0.48	2838
	COV (%)	1.65	1.65		12.02	42.90

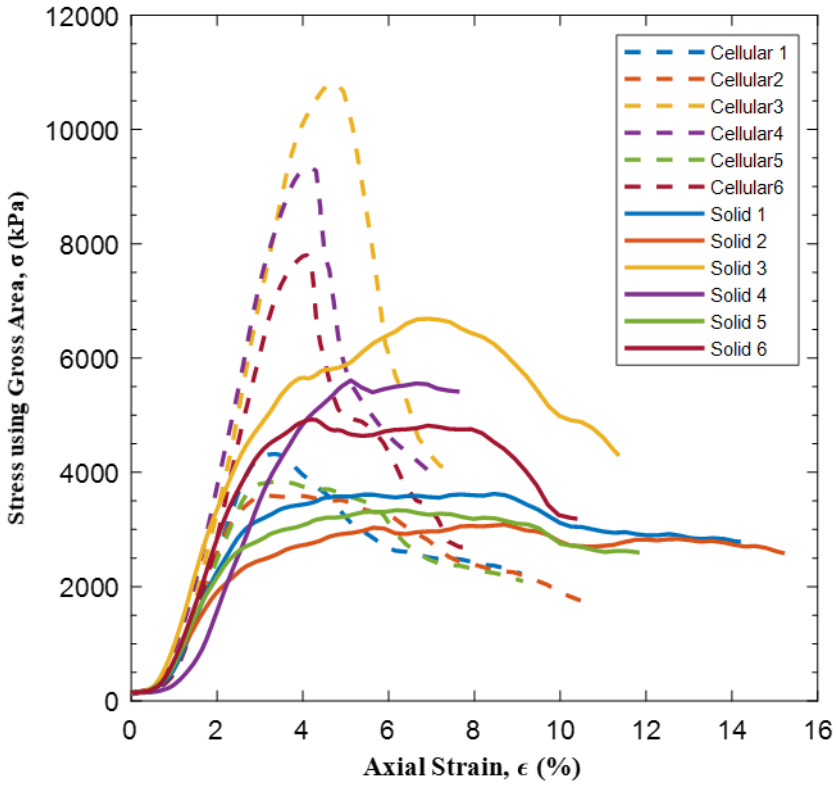

Figure 4.52 Stress-strain curves using gross area of Horn prototypes in Batch S.

From the stress-strain curves, it is clear that specimens exhibited two different behaviors for the cellular and solid configurations. Parts 3, 4, and 6 (for the two configurations) were oven dried before testing and showed higher strength than the specimens that were not dried (1, 2 and 5). The cellular structures in this batch presented Shear 1 and 2 failure mechanism, as shown in Figure 4.53 and Figure 4.54, and the solid structures showed Shear 2 failures (Figure 4.55). The improvement when comparing load-to-weight ratios from the cellular to solid structures was 97% (Table 4.18 and Figure 4.56).

Figure 4.53 Shear 1 failure mode of Horn cellular structures (Batch S).

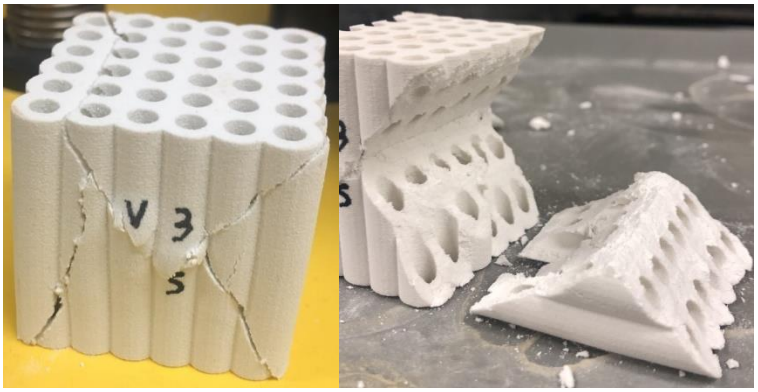

Figure 4.54 Shear 2 failure mode of Horn cellular structures (Batch S).

Figure 4.55 Shear 2 failure mode of Horn solid structures (Batch S).

Table 4.18 Load-to-weight ratio of Horn in Batch S.

		Weight (g)	Max. Load (N)	Load/Weight ratio (N/g)	Improvement (%)
Solid	**Mean**	135.40	9537	70.44	97
	SD	2.61	2753		
	COV (%)	1.92	28.86		
Cellular	**Mean**	100.30	13927	138.85	
	SD	1.38	5975		
	COV (%)	1.37	42.90		

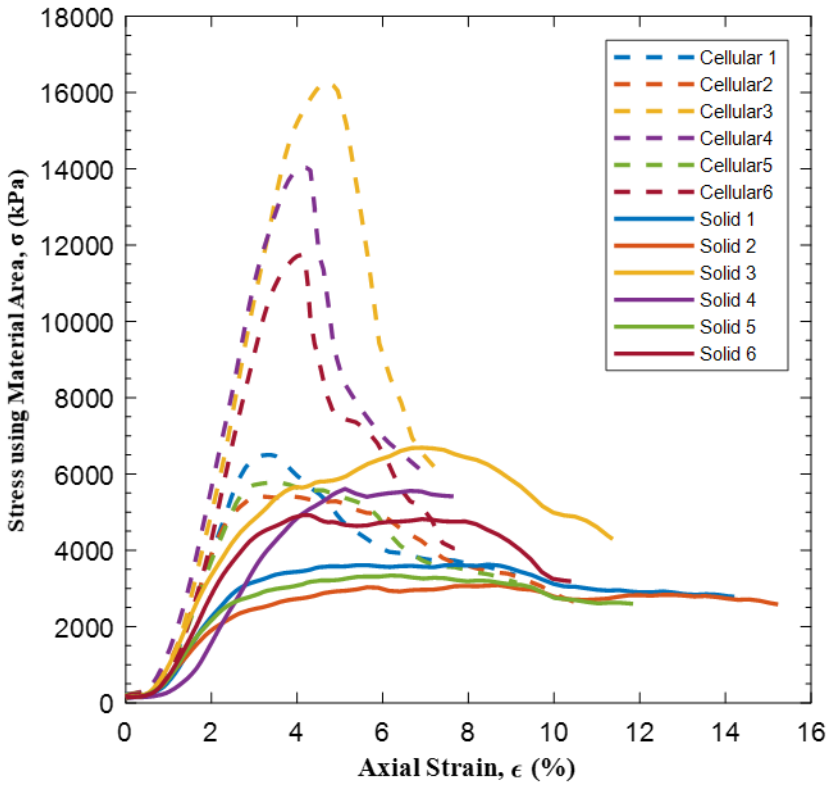

Figure 4.56 Stress-strain curves using material area of Horn prototypes in Batch S.

4.3.2.2.6 Batch U

Batch U had the same composition of Batch S. All specimens were oven dried before testing. The specimens were tested 18 days after being printed and Table 4.19 presents the

properties for them. Figure 4.57 presents the stress-strain curves for all the prototypes in Batch U. Table 4.20 reports the load-to-weight ratios for prototypes in this batch.

Table 4.19 Horn properties in Batch U.

		Gross Density (g/cm^3)	Material Density (g/cm^3)	Relative Density	Stain at Peak Stress (%)	Max. Stress using Gross Area (kPa)
Solid	**Mean**	1.28	1.28	1.00	5.70	6244.89
	SD	0.03	0.03		0.77	1028.84
	COV (%)	2.23	2.23		13.53	16.47
Cellular	**Mean**	0.95	1.43	0.66	4.43	8544
	SD	0.02	0.02		0.19	1161
	COV (%)	1.60	1.60		4.23	13.58

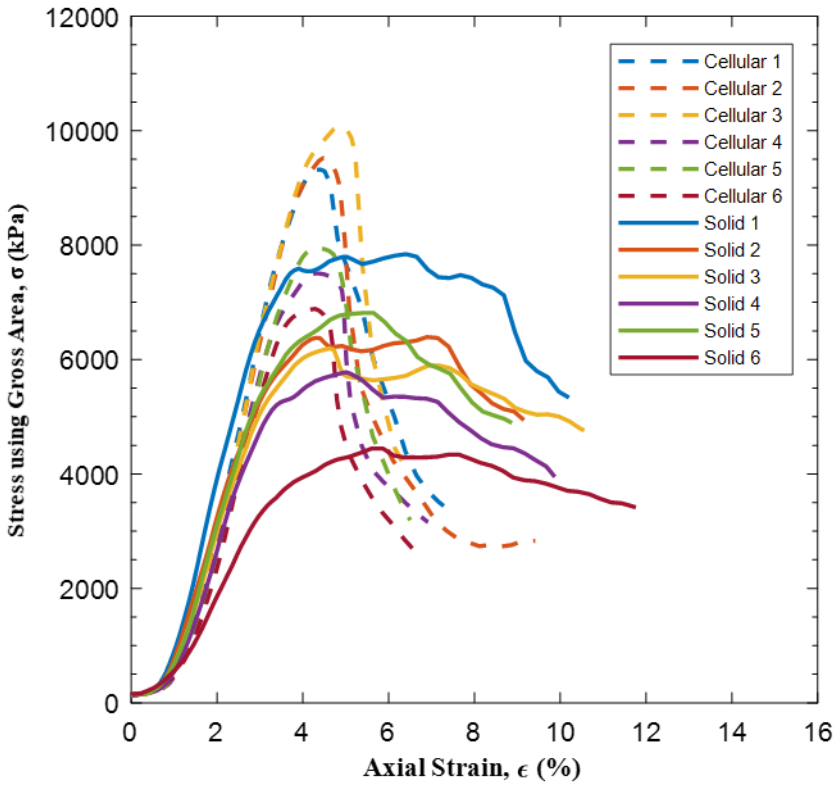

Figure 4.57 Stress-strain curves using gross area of Horn prototypes in Batch U.

For these oven dried specimens, it is possible to notice the drastic drop in stress after the peak stress is reached for the cellular structures, and a residual strength for the solid structures.

The cellular structures had the Shear 1 failure mode, as shown in Figure 4.58, and the solid structures presented Shear 2 failures (Figure 4.59). The increase in the load-to-weight ratio was 84% for this batch, when comparing cellular structures with the solid structures (Table 4.20 and Figure 4.60).

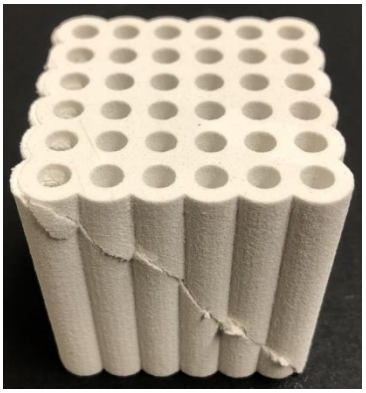

Figure 4.58 Shear 1 failure mode of Horn cellular structures (Batch U).

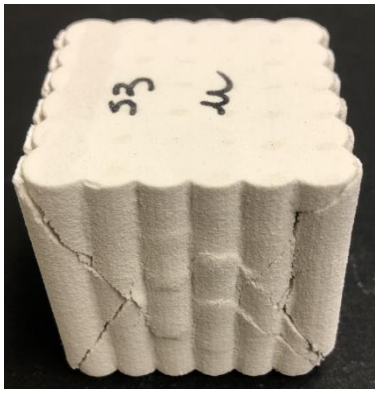

Figure 4.59 Shear 2 failure mode of Horn solid structures (Batch U).

Table 4.20 Load-to-weight ratio of Horn in Batch U.

		Weight (g)	Max. Load (N)	Load/Weight ratio (N/g)	Improvement (%)
Solid	**Mean**	135.14	13106	96.98	84
	SD	2.86	2155		
	COV (%)	2.11	16.44		
Cellular	**Mean**	100.85	17992	178.42	
	SD	1.56	2444		
	COV (%)	1.54	13.58		

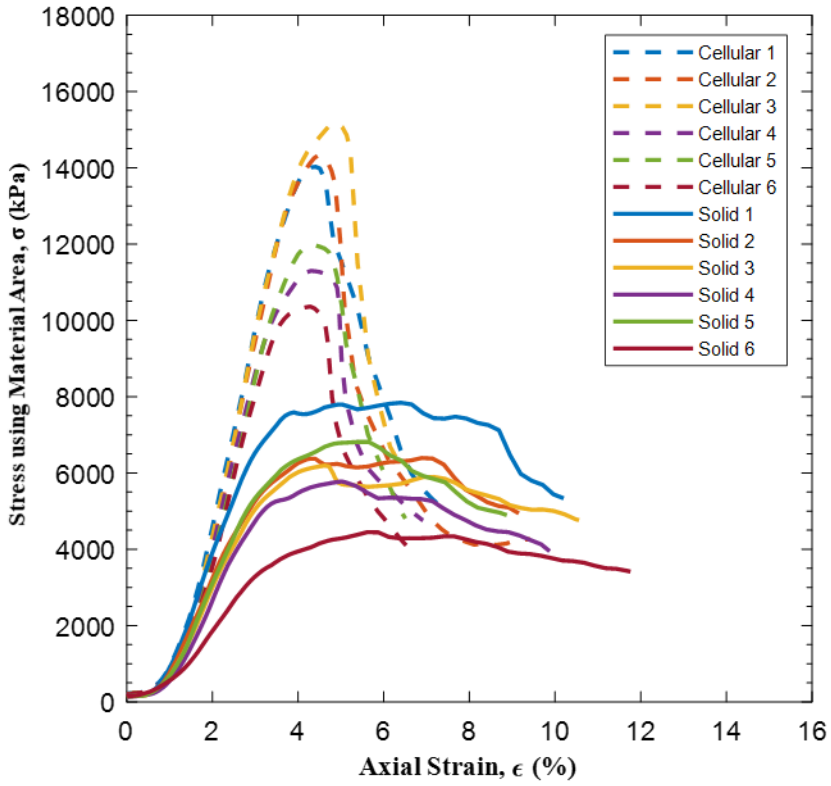

Figure 4.60 Stress-strain curves using gross area of Horn prototypes in Batch U.

4.3.3 Segment 3 – Toucan Beak, Honeycomb, Plant Stalk and Horn

Because the positioning in the build volume of the 3D printer and the quantity of days specimens were tested after printing influenced the properties and strength of the specimens, just one cellular structure was printed in each batch at the same position for this segment, as illustrated

in Figure 4.61. Three cylinders were also printed for each batch at the same locations to track material properties. The shapes printed were the four different designs of the Toucan Beak, the Honeycomb, the Plant Stalk, and the Horn. All cellular structures and cylinders were tested exactly 8 days after being printed, and with a doubled rate of 0.011 mm/s. This doubled rate was due to a default rate being used by accident. While this change makes it difficult to compare these results to those discussed in the segments above, all of the specimens in this segment were tested at this same rate and therefore, can be compared. None of the cellular structures or cylinders were oven dried before testing.

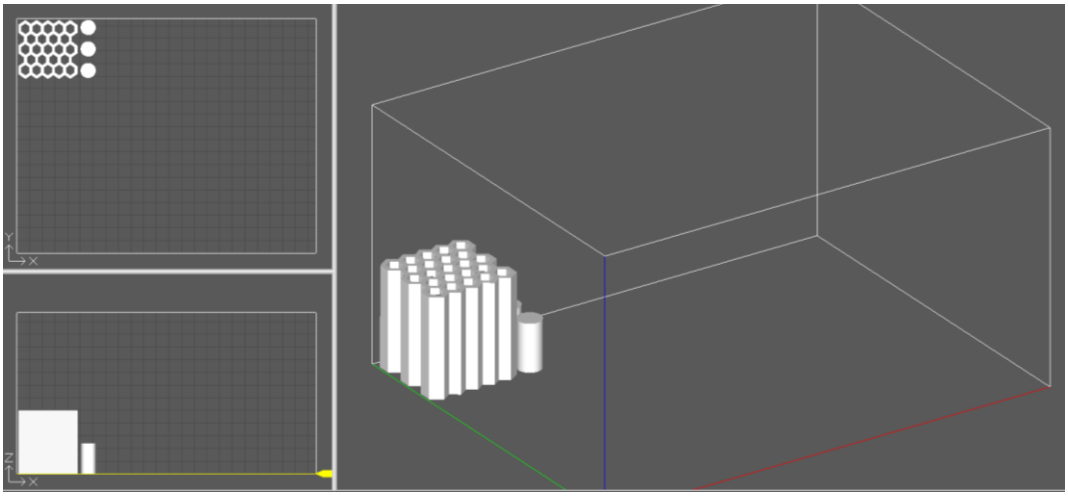

Figure 4.61 Location of prototype and cylinders in Batches TB I to H.

4.3.3.1 Cylinders

The properties determined for the cylinders in batches TB I to H are presented in Table 4.21. The statistical values including mean, SD, and COV for the entire group.

Table 4.21 Cylinders properties in Segment 3.

Batch	Height (mm)	Density (g/cm^3)	UCS (kPa)	Strain at Peak Stress (%)	Young's Modulus (GPa)
TB I	24.24	1.32	5397	1.46	1.76
TB II	24.22	1.31	5072	1.85	1.62
TB III	24.27	1.32	5367	1.69	2.2
TB IV	24.25	1.3	5536	1.95	1.46
HC	24.20	1.3	4389	5.48	0.48
PS	24.19	1.31	4973	4.76	0.34
H	24.19	1.29	4875	6.83	0.54
Mean	24.22	1.31	5098	3.26	1.24
SD	0.04	0.01	467	2.09	0.91
COV (%)	0.16	0.92	9.16	64.04	73.91

For the entire group, the COV for height and density were small (0.16 and 0.92%); moderate for UCS (9.16%); however, SPS and E had substantial different COV's (64.04 and 73.91% respectively). From the means of each batch, it is possible to divide the results into two groups with similar properties: TB I to TB IV and HC to H. Table 4.22 shows how the COVs decrease if the batches are separated into these two groups.

Table 4.22 Cylinders properties for the two groups in Segment 3.

Batch	Height (mm)	Density (g/cm^3)	UCS (kPa)	Strain at Peak Stress (%)	Young's Modulus (GPa)
TB I	24.24	1.32	5397	1.46	1.76
TB II	24.22	1.31	5072	1.85	1.62
TB III	24.27	1.32	5367	1.69	2.2
TB IV	24.25	1.3	5536	1.95	1.46
Mean	24.24	1.31	5343	1.74	1.76
SD	0.04	0.01	379	0.55	0.83
COV (%)	0.15	0.85	7.09	31.92	47.25
HC	24.20	1.3	4389	5.48	0.48
PS	24.19	1.31	4973	4.76	0.34
H	24.19	1.29	4875	6.83	0.54
Mean	24.19	1.30	4730	5.55	0.45
SD	0.02	0.01	317	1.41	0.15
COV (%)	0.07	0.72	6.70	25.46	32.93

The material for the first group of this segment had a mean height of 24.24 mm, density of 1.31 g/cm^3, UCS of 5343 kPa, SPS of 1.74%, and E of 1.76 GPa. The second group had a mean height of 24.19 mm, density of 1.30 g/cm^3, UCS of 4746 kPa, SPS of 5.69%, and E of 0.45 GPa. It is possible to conclude that objects from batches TB I to TB IV were stiffer and resulted in less deformation before reaching the peak stress than specimens in batches HC to H. Figure 4.62 and Figure 4.63 show the stress-strain curves for the two groups. Despite the significant variability in SPS and E within each batch, the stress-strain curves demonstrate similar shapes.

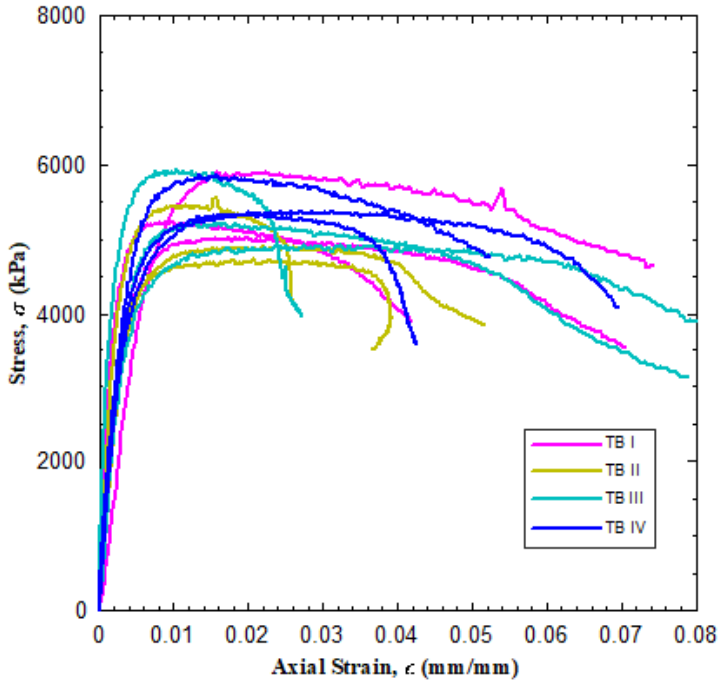

Figure 4.62 Stress-strain curves of cylinders in Batches TB I to TB IV.

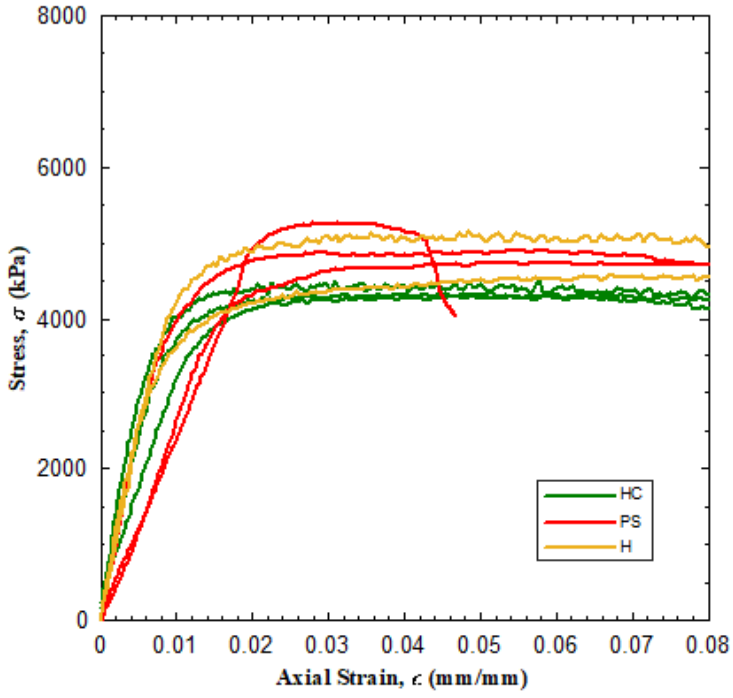

Figure 4.63 Stress-strain curves of cylinders in Batches HC to H.

4.3.3.2 Bio-inspired structures

According to the results of the cylinders, TB I to TB IV prototypes could be compared together as one group, and HC to H as another group. Table 4.23 presents the properties obtained for the cellular structures in each batch.

Table 4.23 Prototypes properties in batches TB I to H.

Batch	Shape	Gross Density (g/cm^3)	Material Density (g/cm^3)	Relative Density	Stain at Peak Stress (%)	Max. Stress using Gross Area (kPa)
TB I	Toucan Beak I	0.82	1.5	0.55	2.91	5723
TB II	Toucan Beak II	0.95	1.5	0.63	3.31	6590
TB III	Toucan Beak III	0.89	1.61	0.55	3.31	5794
TB IV	Toucan Beak IV	0.68	1.45	0.47	2.90	4568
HC	Honeycomb	0.79	1.49	0.53	2.89	5752
PS	Plant Stalk	0.76	1.45	0.52	3.33	5611
H	Horn	0.96	1.44	0.66	3.73	7754

Comparing the different shapes of the Toucan Beak (batches TB I, TB II, TB III and TB IV), Toucan Beak II had the highest compressive strength (6590 kPa), and Toucan Beak IV had the lowest (4568 kPa). Toucan Beak I and III had very similar performances in terms of UCS (5723 and 5794 kPa, respectively). Toucan Beak II and III exhibited higher SPS (3.31%) compared to Toucan Beak I and IV (2.91%). Toucan Beak II was the strongest design and Toucan Beak IV was the weakest, as reported from Batches D and E in the first segment. This order based on strength also follows the same pattern as the relative density. The stress-strain curves of the Toucan Beak specimens are presented in Figure 4.64.

Comparing batches HC, PS and H, corresponding to the Honeycomb, Plant Stalk and Horn shapes, the Horn exhibited the highest UCS (7754 kPa), and the Honeycomb and Plant Stalk had very similar strengths (5752 and 5611 kPa, respectively). The Horn shape exhibited higher SPS

(3.73%), followed by the Plant Stalk (3.33%), and then the Honeycomb (2.89%). It is possible to conclude that the order of UCS (i.e., Horn, Honeycomb, and Plant Stalk) corresponds to the order of relative density. The stress-strain curves for the specimens in this group are presented in Figure 4.65.

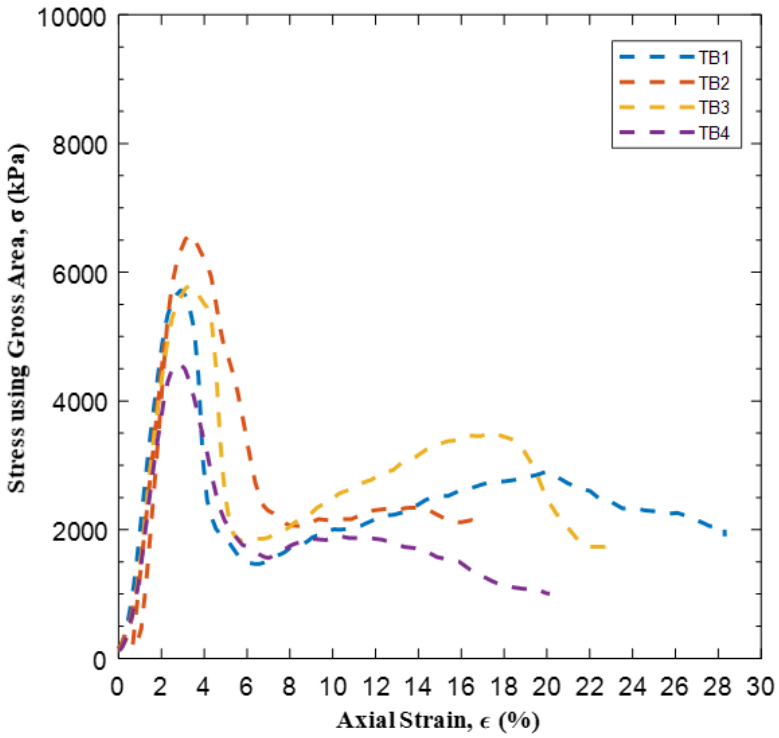

Figure 4.64 Stress-strain curves of cellular structures in batches TB I to TB IV.

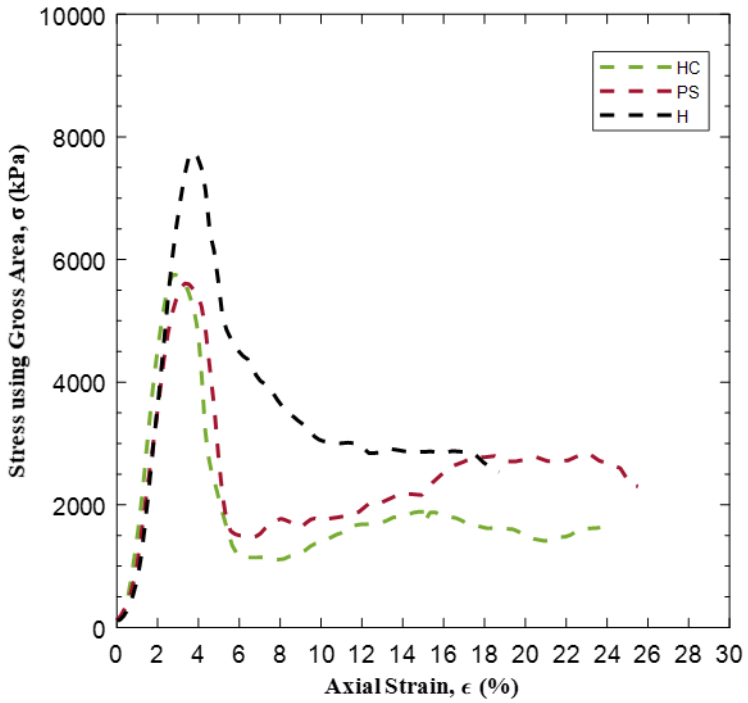

Figure 4.65 Stress-strain curves of cellular structures in batches HC to H.

Table 4.24 presents the load-to-weight ratios for the prototypes in these batches. Toucan Beak I and II showed similar load-to-weight performance in this segment. Toucan Beak III once again presented the worst efficiency in terms of material utilization. For the second group in this segment, the Horn exhibited the most efficient material usage, followed by the Plant Stalk, and then the Honeycomb.

Table 4.24 Load-to-weight ratio of prototypes in Batches TB I to H.

Batch	Shape	Weight (g)	Max. Load (N)	Load/Weight ratio (N/g)
TB I	Toucan Beak I	80.29	11153	138.91
TB II	Toucan Beak II	80.52	11197	139.06
TB III	Toucan Beak III	86.63	11328	130.76
TB IV	Toucan Beak IV	66.15	8939	135.14
HC	Honeycomb	76.01	11075	145.70
PS	Plant Stalk	83.38	12382	148.50
H	Horn	100.85	16369	162.31

5 CONCLUSIONS

Based on the findings in this study, it is possible to conclude that periodic cellular structures may be a worthwhile design and construction practice in Civil Engineering. A significant amount of material can likely be saved in the construction industry with the utilization of periodic cellular cross-sections similar to those investigated herein. Although this is impossible using traditional fabrication and construction practices, complex shapes for building products will likely be possible in the future from further development of additive manufacturing in this sector. The results of this study also indicate that biomimicry is a strong approach for achieving these efficiently designed products.

The variability of the ProJet 260C 3D printer and the material's susceptibility to experimental differences were found to be important factors in this study. The positioning of the parts inside the build volume of the printer has shown to influence their quality. The compaction of the powder and the boundary conditions vary for different positions inside the batch, causing variations in the properties of the objects. Additionally, the cellular structures presented higher material density than the solid structures, meaning that the 3D printer, within the same area, utilizes more binder to fabricate the cellular structures. This makes comparisons between mechanical properties and material usage more complicated and it prohibited a proper direct comparison of the cellular and solid structures. The number of days specimens were tested after being printed was also shown to influence the strength, as specimens absorbed humidity from the air. Additional testing is needed to better understand these factors and reexamine the findings under more controlled conditions.

From the different Toucan Beak shapes, it was possible to conclude that Toucan Beak I and II were the strongest and most efficient shapes, presenting higher ultimate compressive

strengths and load-to-weight ratios. Toucan Beak IV was the weakest part, showing that the sizes of the cells were excessively large relative to the cross-sectional area, causing the walls to buckle. Toucan Beak III had very thin walls, which caused it to fail at lower stresses than Toucan Beak I and II, and it presented the worst load-to-weight ratio. Furthermore, it is possible to conclude that for the same cellular configuration, the ultimate compressive strength follows the same trend as the relative density, however, the load-to-weight ratio may not. This means that, if the quantity of material in the same gross cross-sectional area increases, the peak load is also going to increase, however, the efficiency of material use does not follow the same rule.

For most shapes, except for Toucan Beak IV, when the gross area was used to calculate stress, the cellular structures had higher compressive strength than the solid structures. This may be explained by the constituent material of the cellular structures being stronger than the one for the solid structures. For axial loading, the solid structures should have exhibited the highest strength. In more complex loading like bending; however, geometry can change the moment of inertia and this is an area that should be studied more in the future for bio-inspired shapes such as those used herein.

When comparing the load withstood and material weight, all of the cellular structures showed an improvement in the load-to-weight ratio compared to the solid configuration. The improvements ranged from 70% with the Honeycomb to 140% with the Plant Stalk. Note that these are still for two different materials and more investigation under better controlled printing processes is recommended.

For most of the batches, the solid structures did exhibit higher strains at the peak stress and the cellular structures resulted in a much more brittle and catastrophic failure after achieving peak stress. Catastrophic failure such as this can have particularly important implications for some

engineering applications and further exploration of these shapes in applications in civil engineering practices is recommended.

REFERENCES

Akpinar, M. V., Pancar, E. B., Şengül, E., and Aslan, H. (2018). Pavement subgrade stabilization with lime and cellular confinement system. *Baltic Journal of Road and Bridge Engineering, 13*(2), 87–93.

Aminanda, Y., Castanié, B., Barrau, J.-J., and Thevenet, P. (2005). Experimental Analysis and Modeling of the Crushing of Honeycomb Cores. *Applied Composite Materials, 12*, 213–227.

Apis Cor (2019). The World's Biggest 3D Printed Building. Retrieved July 2020, from https://www.apis-cor.com/dubai-project.

Arvin, M. R., Zakeri, A., and Shoorijeh, M. B. (2018). Using Finite Element Strength Reduction Method for Stability Analysis of Geocell-Reinforced Slopes. *Geotechnical and Geological Engineering, 37*(3), 1453-1467.

AskNature (2016). STICKS lightweight structural system. TECTONICA Architecture. Retrieved September 2020, from https://asknature.org/idea/stick-s-lightweight-structural-system/.

ASTM International (2020). *C39/C39M-20 Standard Test Methods for Compressive Strength of Cylindrical Concrete Specimens.* West Conshohocken, PA.

Bechtle, S., Ang, S. F., and Schneider, G. A. (2010). On the Mechanical Properties of Hierarchically Structured Biological Materials. *Biomaterials, 31*(25), 6378–6385.

Benyus, J. M. (1997). Biomimicry: Innovation inspired by nature (First ed.). New York: Morrow.

Bertram, J. E., and Gosline, J. M. (1986). Fracture toughness design in horse hoof keratin. *The Journal of Experimental Biology, 125*, 29–47.

Bhushan, B. (2009). Introduction : Biomimetics : Lessons from Nature - An Overview. *Philosophical Transactions of the Royal Society B: Biological Sciences, 367*(1893), 1445–1486.

Bikas, H., Stavropoulos, P. and Chryssolouris, G. (2016), Additive manufacturing methods and modelling approaches: a critical review. *International Journal of Advanced Manufacturing and Technology, 83*, 389–405.

Blue Planet (2015). Economically Sustainable Carbon Capture. Retrieved September 2020, from http://www.blueplanet-ltd.com.

Brezny, R., and Green, D.J. (1993). Uniaxial Strength Behavior of Brittle Cellular Materials. *Journal of the American Ceramic Society, 76*, 2185-2192.

Camacho, D.D., Clayton P., O'Brien W.J., Seepersad C., Juenger M., Ferron R., and Salamone S. (2018). Applications of additive manufacturing in the construction industry – A forward-looking review. *Automation in Construction, 89*,110–119.

Cesaretti, G., Dini, E., De Kestelier, X., Colla, V., and Pambaguian, L. (2014). Building components for an outpost on the lunar soil by means of a novel 3D printing technology. *Acta Astronautica, 93*, 430-450.

Chen, H., and Zhao Y.F. (2016). Process parameters optimization for improving surface quality and manufacturing accuracy of binder jetting additive manufacturing process. *Rapid Prototyping Journal, 22*(3), 527–538.

Chiras, S., Mumm, D.R., Evans, A.G., N. Wicks, J.W. Hutchinson, K. Dharmasena, H.N.G. Wadley, S. Fichter, (2002). The structural performance of near-optimized truss core panels. *International Journal of Solids and Structures, 39*(15), 4093–4115.

Chiusoli, A. (2018) The first 3D printed House with earth| Gaia. Retrieved June 2020, from https://www.3dwasp.com/en/3d-printed-house-gaia/.

Choi, J., and Lee, J. (2014). Preliminary Research of Truss-wall Corrugated Cellular Solids. *Applied Mechanics and Materials, 510*, 139–149.

Compton, B.G., and Lewis, J.A. (2014). 3D-Printing of Lightweight Cellular Composites. *Advanced Materials, 26*, 5930–5935.

CONCR3DE (2020). Stone 3D-printing for Construction, Design and Research. Retrieved June 2020, from https://concr3de.com/.

Côté, F., Deshpande, V.S., Fleck, N.A., and Evans, A.G. (2004). The out-of-plane compressive behavior of metallic honeycombs. *Materials Science and Engineering: A, 380*(1–2), 272–280.

Deshpande, V.S., Fleck, N.A., and Ashby, M.F. (2001). Effective properties of the octet-truss lattice material. *Journal of the Mechanics and Physics of Solids, 49*(8), 1747–1769.

Dimas, L.S., Bratzel, G.H., Eylon, I. and Buehler, M.J. (2013). Tough Composites Inspired by Mineralized Natural Materials: Computation, 3D printing, and Testing. A*dvanced Functional Materials, 23*, 4629–4638.

D-Shape (2020). Retrieved June 2020, from https://d-shape.com/our-technology/.

D-Shape (2010). UnaCasaTuttaDiUnPezzo. Retrieved June 2020, from https://d-shape.com/portfolio-item/casa-ferreri/.

Elliott, A. and Waters, C. (2019). *Additive Manufacturing for Designers - A Primer*, SAE International.

Emerging Objects (2020). Big ideas about 3D printing & printing big. Retrieved June 2020, from https://www.emergingobjects.com/.

Evans, A.G., Hutchinson, J.W., Fleck, N.A., Ashby, M.F., and Wadley, H.N.G. (2001). The topological design of multifunctional cellular metals. *Progress in Materials Science, 46*(3–4), 309–327.

Fereshtenejad, S., and Song, J. (2016). Fundamental Study on Applicability of Powder-Based 3D Printer for Physical Modeling in Rock Mechanics. *Rock Mechanics and Rock Engineering, 49*(6), 2065–2074.

Fleck, N. A., and Deshpande, V. S. (2004). The Resistance of Clamped Sandwich Beams to Shock Loading. ASME. *Journal of Applied Mechanics, 71*(3), 386–401.

Freiman, S. W., and Mecholsky, J. J. (2012). *The Fracture of Brittle Materials: Testing and Analysis*. The American Ceramic Society. John Wiley & Sons, Inc., New Jersey.

Frølich, S., Weaver, J.C., Dean, M.N. and Birkedal, H. (2017). Uncovering Nature's Design Strategies through Parametric Modeling, Multi-Material 3D Printing, and Mechanical Testing. *Advanced Engineering Materials, 19*, e201600848.

Fu, Q., Saiz, E. and Tomsia, A.P. (2011). Bioinspired Strong and Highly Porous Glass Scaffolds. *Advanced Functional Materials, 21*, 1058–1063.

Gan, Z., Turner, M. D., and Gu, M. (2016). Biomimetic gyroid nanostructures exceeding their natural origins. *Science Advances*, *2*(5), e1600084.

Gao, W., Zhang, Y., Ramanujan, D., Ramani, K., Chen, Y., Williams, C. B., Wang, C.C.L, Shin, Y.C., Zhang, S., and Zavattieri, P.D. (2015). The status, challenges, and future of additive manufacturing in engineering. *Computer-Aided Design*, *69*, 65–89.

Gibson, L., and Ashby, M. (1997). *Cellular Solids: Structure and Properties.* Cambridge Solid State Science Series. Cambridge: Cambridge University Press.

Gibson, I., Rosen, D., and Stucker, B. (2015). *Additive Manufacturing Technologies: 3D Printing, Rapid Prototyping, and Direct Digital Manufacturing*. Springer, New York, NY.

Gu, G.X., Libonati, F., Wettermark, S. D., and Buehler, M.J. (2017). Printing nature: Unraveling the role of nacre's mineral bridges. *Journal of the Mechanical Behavior of Biomedical Materials*, *76*, 135–144.

Gu, G. X., Su, I., Sharma, S., Voros, J. L., Qin, Z., and Buehler, M. J. (2016). Three-Dimensional-Printing of Bio-Inspired Composites. ASME. Journal of Biomechanical Eng*ineering, 138*(2), 021006.

Gümrük, R., Mines, R.A.W. & Karadeniz, S. (2013). Static mechanical behaviors of stainless-steel micro-lattice structures under different loading conditions. *Materials Science and Engineering: A. 586*, 392-406.

Hosford, W. (2010). *Mechanical Behavior of Materials*. 2nd Edition. Cambridge University Press, New York.

Huang, S. H., Liu, P., Mokasdar, A., and Hou, L. (2013). Additive manufacturing and its societal impact: A literature review. *The International Journal of Advanced Manufacturing Technology, 67*(5-8), 1191–1203.

IFAI (1970). Geocells. *Geosynthetics Magazine*. Retrieved December 2020, from https://geosyntheticsmagazine.com/1970/01/01/geocells.

Ivanić, K.-Z., Tadić, Z., and Omazić, M. A. (2015). *BIOMIMICRY – AN OVERVIEW*. *5*, 19–36.

Jeong, J., Lee Y., and Cho, M. (2013). Sequential multiscale analysis on size-dependent mehcanical behavior of micro/nano-sized honeycomb structures. *Mechanics of Materials,*

57, 109-133.

Kasapi, M. A., and Gosline, J. M. (1997). Design complexity and fracture control in the equine hoof wall. *The Journal of Experimental Biology*, *200*(11), 1639–1659.

Kasapi, M. A., and Gosline, J. M. (1999). Micromechanics of the equine hoof wall: optimizing crack control and material stiffness through modulation of the properties of keratin. *The Journal of Experimental Biology*, *202*(4), 377–391.

Kennedy, E. B. (2017). Biomimicry in Industry: The Philosophical and Empirical Rationale for Reimagining R&D (Doctoral Dissertation). The University of Akron, Ohio, USA. Available from ProQuest Dissertations & Theses Global Database (UMI No. 13834496).

Khan, M. K. (2006). Compressive and lamination strength of honeycomb sandwich panels with strain energy calculation from ASTM standards. *Proceedings of The Institution of Mechanical Engineers Part G-journal of Aerospace Engineering, 200*.

Khoshnevis, B. (2004). Automated construction by contour crafting—related robotics and information technologies. *Automation in Construction, 13*(1), 5–19.

Khoshnevis, B. (1999). Contour crafting-state of development. Solid Freeform Fabrication Symposium Proceedings, Austin, USA, 743–750.

Khoshnevis, B., and Dutton, R. (1998). Innovative rapid prototyping process makes large sized, smooth surfaced complex shapes in a wide variety of materials. *Materials Technology, 13*(2), 53–56.

Labonnote, N., Rønnquist, A., Manum, B., and Rüther, P. (2016). Additive construction: state-of-the-art, challenges and opportunities. *Automation in Construction*, *72*, 347–366.

Leshchinsky, B. A. (2012). Enhancing Ballast Performance using Geocell Confinement (Doctoral Dissertation). Columbia University.

Leshchinsky, D., Ling, H. I., Wang, J.-P., Rosen, A., and Mohri, Y. (2009). Equivalent seismic coefficient in geocell retention systems. *Geotextiles and Geomembranes, 27*(1), 9-18.

Libonati, F., Gu, G.X., Qin, Z., Vergani, L. and Buehler, M.J. (2016). Bone-Inspired Materials by Design: Toughness Amplification Observed Using 3D Printing and Testing. *Advanced Engineering Materials, 18*, 1354–1363.

Liu, L., Meng, P., Wang, H., and Guan, Z. (2015). The flatwise compressive properties of Nomex honeycomb core with debonding imperfections in the double cell wall. *Composites Part B: Engineering, 76*, 122–132.

Lu, T.J. (1999). Heat transfer efficiency of metal honeycombs. *International Journal of Heat and Mass Transfer, 42*(11), 2031-2040.

Mann, S. (2001). *Biomineralization: Principles and Concepts in Bioinorganic Materials Chemistry.* New York: Oxford University Press.

Martin, S. M., Senf, D. F., and Crowe, R. E. (1998). Using cellular confinement systems for slope stabilization. *Public Works*, *129*(1), 36.

Mayer, G., and Sarikaya, M. (2002). Rigid biological composite materials: Structural examples for biomimetic design. *Experimental Mechanics*, *42*(4), 395–403.

Mehdipour, I., Ghazavi, M., and Moayed, R. Z. (2013). Numerical study on stability analysis of geocell reinforced slopes by considering the bending effect. *Geotextiles and Geomembranes*, *37*, 23–34.

Mehdipour, I., Ghazavi, M., and Moayed, R. Z. (2017). Stability Analysis of Geocell-Reinforced Slopes Using the Limit Equilibrium Horizontal Slice Method. *International Journal of Geomechanics*, *17*(9), 06017007.

Menig, R., Meyers, M. H., Meyers, M. A., and Vecchio, K. S. (2000). Quasi-static and dynamic mechanical response of Haliotis rufescens (abalone) shells. *Acta Materialia*, *48*(9), 2383–2398.

Mera, H. and Takata, T. (2000). High-Performance Fibers. In Ullmann's Encyclopedia of Industrial Chemistry.

Meyers, M. A., and Chen, P.-Y. (2014). *Biological Materials Science: Biological Materials, Bioinspired Materials, and Biomaterials.* Cambridge: Cambridge University Press.

Meyers, M. A., Chen, P. -Y., Lin, A. Y. M., and Seki, Y. (2008). Biological materials: Structure and mechanical properties. *Progress in Materials Science*, *53*(1), 1–206.

Meyers, M. A., McKittrick, J., and Chen, P.-Y. (2013). Structural biological materials: critical mechanics-materials connections. *Science (New York, N.Y.)*, *339*(6121), 773–779.

Mirzaeifar, R., Dimas, L. S. Qin, Z., and Buehler, M. J. (2016). Defect-Tolerant Bioinspired Hierarchical Composites: Simulation and Experiment. *ACS Biomaterials Science and Engineering*, *1*(5), 295–304.

Mueller, R., Howe, S., Kochmann, D., Ali, H., Andersen, C., Burgoyne, H., Chambers, W., Clinton, R., De Kestellier, X., Ebelt, K., and Gerner, S. (2016). Automated additive construction (AAC) for Earth and space using in-situ resources. *Proceedings of the Fifteenth Biennial ASCE Aerospace Division International Conference on Engineering, Science, Construction, and Operations in Challenging Environments* (Earth & Space 2016).

Nakahara, H., Kakei, M., and Bevelander, G. (1982). Electron microscopic and amino acid studies on the outer and inner shell layers of Haliotis rufescens. *Venus Japanese Journal of Malacology*, *41*(1), 33–46.

Nature Process Design (2005). Designing with Natural Processes (building as if you are part of nature). Retrieved September 2020, from http://www.naturalprocessdesign.com/.

Ngo, T., Kashani, A., Imbalzano, G., Nguyen, K. and Hui, D. (2018). Additive manufacturing (3D printing): A review of materials, methods, applications and challenges. *Composites Part B: Engineering*, *143*, 172–196.

Nguyen-Van, V., Tran, P., Peng, C., Pham, L., Zhang, G., and Nguyen-Xuan, H. (2020). Bioinspired cellular cementitious structures for prefabricated construction: Hybrid design & performance evaluations. *Automation in Construction, 119*, 103324.

Novitskaya, E., Chen, P.Y., Lee, S., et al. (2011). Anisotropy in the compressive mechanical properties of bovine cortical bone and the mineral and protein constituents. *Acta Biomaterials, 7*, 3170–3177.

Oberti, I., and Plantamura, F. (2015). Is 3D printed house sustainable? Proceedings of International Conference CISBAT 2015: Future Buildings and Districts Sustainability from Nano to Urban Scale, 173–178.

Pegna, J. (1997). Exploratory investigation of solid free form construction. *Automation in Construction, 5*, 427–437.

Perrot, A., Rangeard, D., and Courteille. E. (2018). 3D printing of earth-based materials: processing aspects. *Construction and Building Materials, 172*, 670–676.

Pokharel, S. K., Han, J., Leshchinsky, D., and Parsons, R. L. (2018). Experimental evaluation of geocell-reinforced bases under repeated loading. *International Journal of Pavement Research and Technology, 11*(2), 114–127.

Presto GeoSystems (2020). GEOWEB Geocells. How Geocells Work for Soil Stabilization. Retrieved December 2020 from https://www.prestogeo.com/products/soil-stabilization/geoweb-geocells.

Pronk, Ir. A.D.C., Blacha M., and Bots, A. (2008). Nature's Experiences for Building Technology. Building Technology Department, Eindhoven University of Technology, Eindhoven, Netherlands.

Qin, Z., Jung, G. S., Kang, M. J., & Buehler, M. J. (2017). The mechanics and design of a lightweight three-dimensional graphene assembly. *Science advances, 3*(1), e1601536.

Sammis, C. G., and Ashby, M. F. (1986). The Failure of Brittle Porous Solids under Compressive Stress States. *Acta Metallurgica, 34*, 511–26.

Sarikaya, M. (1994). An introduction to biomimetics: a structural viewpoint. *Microscopy Research and Technique, 27*, 360–375.

Satyal, S.R., Leshchinsky, B., Han, J., and Neupane, M. (2018). Use of cellular confinement for improved railway performance on soft subgrades. *Geotextiles and Geomembranes, 46*, 190–205.

Schaedler, T.A., Jacobsen, A.J., Torrents, A., Sorensen, A. E., Lian, J., Greer, J. R., Valdevit, L., and Carter, W. B. (2011). Ultralight Metallic Microlattices. *Science, 334*(6058), 962-965.

Seki, Y., Schneider, M. S., and Meyers, M. A. (2005). Structure and mechanical behavior of a toucan beak. *Acta Materialia, 53*(20), 5281–5296.

Shahverdi, H., Keshavanarayana, S., Kothare, A., Yang, C., and Horner, A. L. (2017). Experimental and numerical study on the mechanical response of fiberglass/phenolic honeycomb core under uniaxial in-plane loading. *Paper presented at the International SAMPE Technical Conference*, 2149–2165.

Shakor, P., Sanjayan, J., Nazari, A., and Nejadi, S. (2017). Modified 3D printed powder to cement-based material and mechanical properties of cement scaffold used in 3D printing. *Construction and Building Materials, 138*, 398–409.

The Biomimicry Institute (2020). What is biomimicry. Retrieved September 2020, from https://biomimicry.org/what-is-biomimicry/.

Tiwary, C. S., Kishore, S., Sarkar, S., Mahapatra, D. R., Ajayan, P. M., and Chattopadhyay, K. (2015). Morphogenesis and mechanostabilization of complex natural and 3D printed shapes. *Science advances*, *1*(4), e1400052.

Tombolato, L., Novitskaya, E. E., Chen, P. -Y., Sheppard, F. A., and McKittrick, J. (2010). Microstructure, elastic properties and deformation mechanisms of horn keratin. *Acta Biomaterialia*, *6*(2), 319–330.

Tran, P., Ngo, T.D., Ghazlan, A., and Hui, D. (2017). Bimaterial 3D printing and numerical analysis of bio-inspired composite structures under in-plane and transverse loadings. *Composites Part B: Engineering, 108*, 210–223.

UGSI Solutions (2020). Pax Water Technologies. Retrieved September 2020, from https://www.paxwater.com/.

Ujjawal, K. N., Venkateswarlu, H., and Hegde, A. (2019). Vibration isolation using 3D cellular confinement system: A numerical investigation. *Soil Dynamics and Earthquake Engineering*, *119*, 220–234.

Vaezi, M., and Chua, C.K. (2011). Effects of layer thickness and binder saturation level parameters on 3D printing process. *International Journal of Advanced Manufacturing and Technology, 53*(1), 275–284.

Wadley, H.N.G, Fleck N., and Evans A.G. (2003). Fabrication and structural performance of periodic cellular metal sandwich structures. *Composites Science and Technology, 63*(16), 2331–2343.

Wadley, H.N.G. (2006). Multifunctional periodic cellular metals. *Philosophical Transactions of the Royal Society A: Mathematical, Physical and Engineering Sciences*, *364*(1838), 31–68.

Wahl, L., Maas, S., Waldmann, D, Zürbes, A., and Frères, P. (2012). Shear stresses in honeycomb sandwich plates: Analytical solution, finite element method and experimental verification. *The journal of sandwich structures & materials, 14*(4), 449–468.

WASP (2018). Retrieved from https://www.3dwasp.com/en/3d-printed-house-gaia/.

Watters, M.P., and Bernhardt, M.L. (2017). Modified curing protocol for improved strength of binder-jetted 3D parts. *Rapid Prototyping Journal*, *23*(6), 1195–1201.

Weibull, W. (1951) A statistical distribution function of wide applicability. *Journal of Applied Mechanics, 18*, 293–297.

Wicks, N. & Hutchinson, J.W. (2001). Optimal Truss Plates. *International Journal of Solids and Structures, 38*, 5165–5183.

Wierzbicki, T. (1983). Crushing analysis of metal honeycombs. *International Journal of Impact Engineering, 1*(2), 157–174.

Woolley-Barker, T. (2014). The Biomimicry Manual: what can designers learn from honeybee? Inhabitat. Retrieved July 2020, from https://inhabitat.com/the-biomimicry-manual-what-can-the-honeybee-teach-designers-about-insulation-elasticity-and-flight/.

Wu, E., and Jiang, W-S. (1997). Axial crush of metallic honeycombs. *International Journal of Impact Engineering*,*19*(5–6), 439–456.

Xia, M., and Sanjayan, J. (2016). Method of formulating geopolymer for 3D printing for construction applications. *Materials and Design*, *110*, 382–390.

Xinye H., Tomoharu M., Toshihiko K., Takashi K. (2017). Seismic Response of a Newly Developed Geocell-Reinforced Soil Retaining Wall Backfilled with Gravel by Shaking Table Model Test. *Geotechnical Hazards from Large Earthquakes and Heavy Rainfalls*. Springer, Tokyo.

Xue, Z., and Hutchinson, J.W. (2004). A comparative study of impulse-resistant metal sandwich plates. *International Journal of Impact Engineering, 30*(10).

Yang, X., Han, J., Leshchinsky, D., and Parsons, R. L. (2013). A three-dimensional mechanistic-empirical model for geocell-reinforced unpaved roads. *Acta Geotechnica*, *8*(2), 201–213.

Yang, X., Han, J., Pokharel, S. K., Manandhar, C., Parsons, R. L., Leshchinsky, D., and Halahmi, I. (2012). Accelerated pavement testing of unpaved roads with geocell-reinforced sand bases. *Geotextiles and Geomembranes*, *32*, 95–103.

Yang, Y., Song, X., Li, X., Chen, Z., Zhou, C., Zhou, Q., Chen, Y. (2018). Recent Progress in Biomimetic Additive Manufacturing Technology: From Materials to Functional Structures. *Advanced Materials, 30*, 1706539.

Zhang, J., and Ashby, M. (1992). The out-of-plane properties of honeycombs. *International Journal of Mechanical Sciences, 34*(6), 475–475.

Zhang, Q., Yang, X., Li, P., Huang, G., Feng, S., Shen, C., Han, B., Zhang, X., Jin, F., Xu, F., Lu, T.J. (2015). Bioinspired engineering of honeycomb structure – Using nature to inspire human innovation. *Progress in Materials Science, 74*, 332–400.